Integrating a Photovoltaic Panel and a Battery Pack in One Module

From concept to prototype

Vega Garita, Victor

DOI
10.4233/uuid:c5af67c1-a665-49df-8b23-0f16d7185fa3

Publication date
2019

Document Version
Final published version

Citation (APA)
Vega Garita, V. (2019). *Integrating a Photovoltaic Panel and a Battery Pack in One Module: From concept to prototype*. [Dissertation (TU Delft), Delft University of Technology]. https://doi.org/10.4233/uuid:c5af67c1-a665-49df-8b23-0f16d7185fa3

Integrating a Photovoltaic Panel and a Battery Pack in One Module

from concept to prototype

Integrating a Photovoltaic Panel and a Battery Pack in One Module

from concept to prototype

Dissertation

for the purpose of obtaining the degree of doctor
at Delft University of Technology
by the authority of the Rector Magnificus, Prof. dr. ir. T. H. J. J. van der Hagen,
chair of the Board for Doctorates
to be defended publicly on Thursday, 13 June 2019 at 10:00 o'clock

by

Víctor Ernesto Vega Garita

Materials Engineer,
Costa Rica Institute of Technology, Cartago, Costa Rica,
born in Heredia, Costa Rica.

This dissertation has been approved by the promotors.
Composition of the doctoral committee:

Rector Magnificus	chairperson
Prof. dr.ir. P. Bauer	Delft University of Technology, promotor
Prof. dr. M. Zeman	Delft University of Technology, promotor

Independent members:

Prof. dr. A.H.M. Smets,	Delft University of Technology
Prof. ir. P.T.M. Vaessen	Delft University of Technology
Prof. dr. M. Gibescu	Utrecht University
Dr. T. Merdzhanova	Jülich Research Centre
Prof. ir. M.A.M.M. van der Meijden	Delft University of Technology, reserve member

Dr.ir. L. Ramirez-Elizondo, Delft University of Technology, contributed to this thesis as a daily supervisor.

Keywords: Photovoltaic energy, batteries, integration, thermal management, battery testing

Printed by: *ProefschriftMaken (https://www.proefschriftmaken.nl)*

Cover & picture: Cover designed by Loeloe Vermeulen and picture from Liselotte Stolk.

ISBN 978-94-6366-170-6

An electronic version of this dissertation is available at
http://repository.tudelft.nl/.

If you don't live according to what you think,
you will end up thinking according to how you live.

José Figuerres Ferrer

Contents

Summary

Photovoltaic (PV) solar energy is variable and not completely predictable; therefore, different energy storage devices have been researched. Among the variety of options, electrochemical cells (commonly called batteries) are technically feasible because of their maturity and stability. However, PV-battery systems face multiple challenges such as high cost and complexity of installation. Cost is the main concern when trying to enable new solutions for the solar market, especially when competing with other renewable technologies, but most importantly, with fossil fuels to reduce the effects of climate change. As a consequence, a new concept that integrates all the components of a PV-battery system in a single device is introduced. By integrating a power electronics unit and a battery pack at the back of a PV panel, referred as *PV-battery Integrated Module* (*PBIM*), the cost of the total system can decrease and become a viable alternative for the solar market. Because the concept is relatively new and not all the challenges have been previously addressed, this dissertation strives to prove the feasibility of the concept and to fill the gaps that have been identified in the literature review. Firstly, an off-grid PV-battery system was selected, and a sizing methodology was proposed to investigate the limitations and boundaries of the integrated device. Having sized the system, the thesis explored the implementation of an energy management system in order to control smartly the direction and magnitude of the power delivery. Then, a thermal model was developed to characterize the thermal response of the *PBIM* and to recommend a thermal management system to decrease the temperature of operation of the battery pack and power electronics. Finally, by testing a *PBIM* prototype and developing an integrated model that reproduces the temperature and power flows expected, a battery testing methodology was developed for finding a suitable battery technology that can comply with the requirements set by the expected operating conditions of the device. Therefore, the research carried out in this dissertation proves that the integration of PV-battery system in one device is technically feasible.

Samenvatting

Omdat fotovoltaïsche zonne-energie (PV) niet constant en niet volledig voorspelbaar is, zijn er verschillende vormen van opslag onderzocht. Onder de verscheidenheid aan opties zijn elektrochemische cellen (ook wel batterijen genoemd) technisch haalbaar vanwege hun ver gevorderde ontwikkeling en stabiliteit. PV-batterijsystemen hebben echter te kampen met meerdere uitdagingen, zoals hoge kosten en grote complexiteit. Het financiële aspect is de grootste zorg bij het vinden van nieuwe oplossingen voor de zonne-energiemarkt. Vooral wanneer ze moeten concurreren met andere hernieuwbare technologieën, maar in het bijzonder met fossiele brandstoffen. Laatstgenoemde is noodzakelijk om het effect van klimaatverandering te verminderen. Als gevolg hiervan introduceren we een nieuw concept dat alle onderdelen van een PV-batterijsysteem in één apparaat integreert. Door de vermogenselektronica en batterij aan de achterkant van een PV-paneel te integreren, hier aangeduid als *PV-Battery Integrated Module* (*PBIM*), dalen de kosten van het totale systeem en kan het een levensvatbaar alternatief worden voor de zonne-energiemarkt. Omdat het concept relatief nieuw is en niet alle uitdagingen eerder zijn geadresseerd, probeert dit proefschrift de haalbaarheid van het concept aan te tonen en de hiaten, die geïdentificeerd zijn in de literatuurstudie aan te vullen. Ten eerste werd een lokaal niet net-gekoppeld PV-batterijsysteem op het platteland geselecteerd en werd er een dimensioneringsmethode voorgesteld om de beperkingen en grenzen van het geïntegreerde systeem te onderzoeken. Na de grootte van het systeem onderzocht te hebben, is ten tweede de implementatie van het energiebeheersysteem onderzocht. Het energiebeheersysteem moet de vermogensrichting en —grootte regelen. Ten derde werd er een thermisch model ontwikkeld om de thermische respons van de *PBIM* te karakteriseren en een thermisch beheersysteem aan te bevelen om de bedrijfstemperatuur van het batterijpakket en de vermogenselektronica te verlagen. Tot slot, door een *PBIM*-prototype te testen en een geïntegreerd model te ontwikkelen dat de verwachte temperatuur- en vermogensstromen reproduceert, is een batterijtestmethodologie ontwikkeld voor het vinden van een geschikte batterijtechnologie. Deze technologie voldoet aan de vereisten die worden gesteld aan het systeem welke gebaseerd zijn op de verwachte operationele omstandigheden. Concluderend, het onderzoek in dit proefschrift toont aan dat de integratie van PV-batterijsystemen in één apparaat technisch haalbaar is.

1

Introduction

The average global temperature of the world is rising as a consequence of the continuously growing greenhouse emissions [1]. According to estimations [2], the average surface temperature of the world is likely to exceed 2°C by the end of the 21st century with respect to the levels before the industrial revolution. More recently, the International Panel on Climate Change has reported that an increase of 1.5°C (above pre-industrial levels) is likely to occur between 2030 and 2052; this is expected to cause extreme temperatures, heavy precipitations, and high probability of droughts in particular regions [3].

Among the various options to mitigate the impact of global warming, renewable energy has been identified as an alternative for the electricity energy sector in order to diminish the dependency on fossil-fuel-based thermal plants [4]. By fostering energy generation from clean sources such as wind and solar energy, the dependence on fossil fuel may reduce as well as the rate at which temperature has been rising [5].

In particular, solar photovoltaic (PV) energy generation has seen a drastic increase in installed capacity during the last years, with a cumulative average PV capacity growth of 49% per year between 2003 to 2013 [6]. In 2017, PV generation represented 1.9% of the global electricity production [7], but it is estimated that by 2050 this will increase to 16% [6].

To make this possible, the challenges related to the variability of solar irradiation must be solved, as they lead to unreliability and instability in the electricity supply [7]. This is due to the mismatch that occurs when the output power from the PV modules and the power demanded from the loads are not equal. A way to cope with this is by incorporating energy storage systems to supply power when there is no irradiation or when it changes rapidly [8]. Benefits of integrating PV and storage systems could be reaped by system owners, and in specific cases are more affordable than PV systems alone [9], specially when feed-in tariffs are in place [10]. However, the system price must continue to drop in order to become a widely adopted technology to face climate change.

1

1.1. Motivation

Current systems that combine PV panels and battery banks present multiple opportunities for improvement, but the most important is the system cost. Even though PV panel and battery prices are dropping fast [11, 12], PV-battery systems are still expensive. Costs can be reduced without necessarily increasing the efficiency and reducing the prices of PV modules, for instance by decreasing the installation expense. Actual PV-battery systems are complex to design and install, requiring extensive technical advice and labor to build the system, which impacts the total cost.

The installation cost of solar systems accounts for around 24% of the total when other soft expenses, not related to hardware, are considered for residential PV systems [13]. This is because, in a typical residential PV-battery system, PV panels on the roof are usually connected to the power electronics and batteries separately inside the households, making the installation process complicated and time-consuming. Moreover, typical systems are bulky, because battery banks and power electronics occupy space dedicated to other activities in the households.

The manner in which a PV-battery system is conceived and designed currently is rigid, as the systems cannot be updated easily in case of an increase in energy demand. Therefore, if more solar panels are required, the total system must be redesigned accordingly. A redesign means new power electronics elements and perhaps a change or an update of the battery bank (the most expensive part), and as a consequence, new components must be bought. At the same time, these kinds of centralized systems are less efficient than modular approaches, because the general performance of the system is determined by the weakest solar panel of the array.

Another cost that should be decreased is the cost of the balance-of-system (BoS) components, which are energy storage devices and power electronics elements needed to implement the system. While the prices of solar panel continue to reduce, BoS cost has not declined at the same rate [14]. For instance, the 54% of the total cost (PV rooftop system, Germany) in 2017 was related to BoS components, while in 2006 this cost was only a 29% [15], as depicted in Figure 1.1. At the moment, the BoS are manufactured independently, and possible synergies between them have not been extensively exploited. By unifying or combining various BoS in new compact devices, the cost of the balance of systems components could be reduced. This is possible due to the savings expected from the manufacturing process as materials reduce and the process speeds up.

1.2. Possible solution

To tackle the issues raised in Section 1.1, this thesis proposes a novel device that combines a battery pack, charge controller, microinverter, and PV module in one unit (refer to Figure 1.2). In particular, the PV-battery system installation effort and cost could lower if a complete system were directly installed at the chosen location. As the installation becomes simpler compared to conventional systems, the labor required could be reduced, which translates into a fewer upfront cost. Another associated cost is related to the system design; this has to do with the professional advice necessary to size the components, i.e., finding appropriate PV array rated power, power electronics

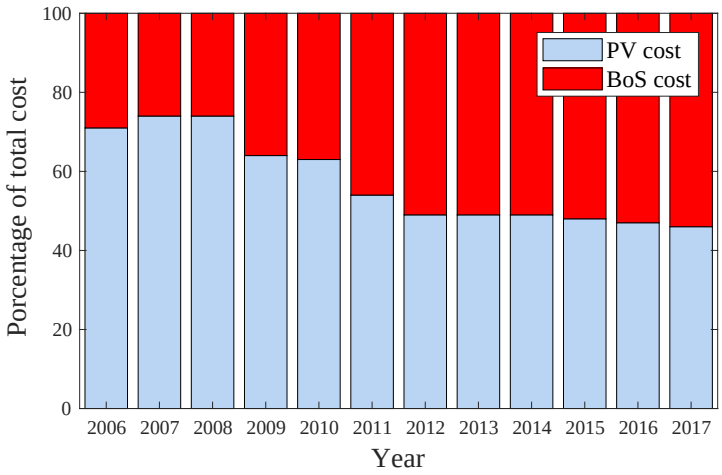

Figure 1.1: Total component-related cost development for PV systems between 10–100 kW_p in Germany. Sourced from [15]

selection based on peak powers, and optimum battery capacity. In this regard, the *PV-battery Integrated Module* (*PBIM*) gives the PV system owner the option to acquire a device that provides a direct connection to the loads without spending time designing the system.

This device provides a modular plug-and-play solution for PV-systems owners. Because it is optimally designed and presents a simple connection to the load, the *PBIM* is easy to use. This device also makes it possible to increment the size of the system by increasing the number of the integrated modules, acting as a building block for scaling up the PV-battery systems in a modular manner. For instance, just one *PV-battery Integrated Module* will not be able to supply a significant portion of the energy demanded

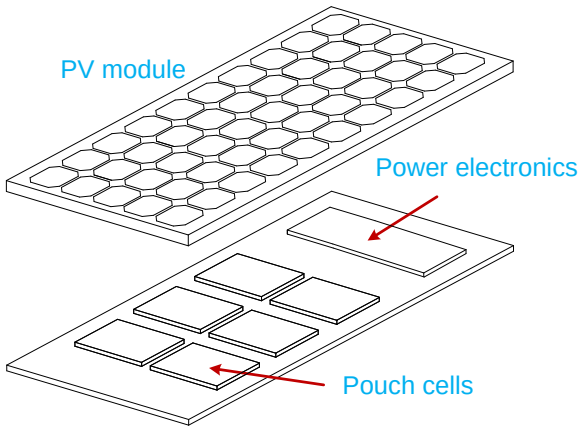

Figure 1.2: *PV-battery Integrated Module* concept. It consist of a PV panel, a battery pack composed of multiple pouch cells (battery pack), and power electronics.

in a household. However, more integrated modules can be connected in parallel to increase the PV generation and energy storage size of the PV-battery system. The benefits of the modular approach are also observed in the case of partial shading. In comparison with PV installations with series connections and central inverters, using multiple *PBIMs* ameliorates the diminution of output power. With this approach, panels with poor illumination conditions do not define the output power of the total system.

1.3. Research objective

Design a device that combines all the components of a typical PV-battery system in one single unit, by optimally sizing the system, enabling intelligent energy management system, proposing an efficient thermal management method, and selecting a suitable battery technology.

1.4. Research questions

In order to achieve the research objective, the following research questions must be answered:

1. What are the most critical challenges and limitations when integrating a PV panel and a battery pack in one device? (chapter 2)

2. What are the boundaries in terms of PV rating and battery capacity for a single *PV-battery Integrated Module* in a standalone system considering system availability? (chapter 3)

3. How to implement an energy management system for the *PV-battery Integrated Module* to enable an intelligent power and energy delivery? (chapter 4)

4. How can high temperatures reached by the battery pack be managed in order to ensure that the *PV-battery Integrated Module* performs within a safe region of operation? (chapter 5)

5. Which is the most suitable electrochemical cell technology or technologies to integrate a PV module and storage physically in one package based on aging? (chapter 6)

1.5. Main contributions

This thesis contributes towards

1. identifying the trends and challenges to overcome for the development of PV-battery integrated devices for outdoor high power applications (PV panels more than 10 W_p),

2. indicating the boundaries in terms of PV rating and battery capacity for a single *PBIM* considering the trade-offs between system availability, battery aging, and components temperature.

3. analyzing via a validated thermal model the concept of physical integration of a PV-battery system while having a look at the thermal behavior and proposing optimum thermal management, and

4. selecting a suitable battery technology and testing it in conditions that emulated the operation of an integrated device, while performing an accelerated aging test in comparison to a battery operating in standard conditions.

1.6. Thesis outline

In this thesis, each chapter addresses an individual research question (Section 1.4). The thesis consists of seven chapters, and they are linked as shown in Figure 1.3. Moreover, the content of the thesis is based on journal and conference papers, as indicated at the beginning of every chapter.

Chapter 2. Integrating a Photovoltaic Storage System in One Device

As a starting point, chapter 2 presents an overview of the current state of the devices that integrate photovoltaic energy and energy storage components (batteries or supercapacitors). The chapter establishes the main challenges to design robust low and high power devices, while defining key aspects that must be solved to turn fundamental research into products for the solar energy market. This chapter helps to determine the route of this thesis, as it identifies as a priority to dive into aspects such as system sizing (chapter 3), thermal management (chapter 5), and the study of battery aging (chapter 6).

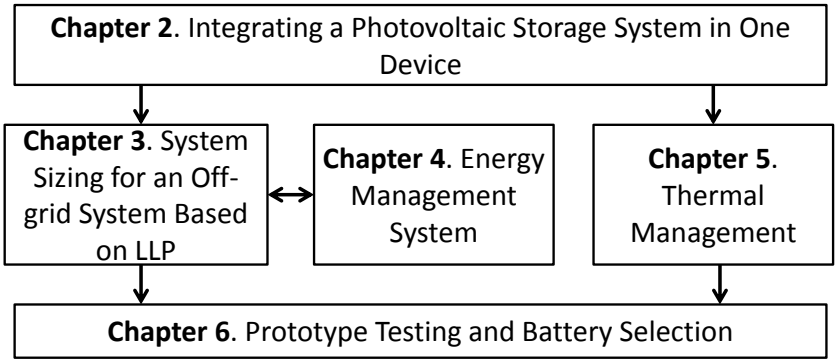

Figure 1.3: Graphical description of the dissertation indicating the connections between chapters.

Chapter 3. System Sizing for an Off-grid System Based on LLP

Chapter 3 introduces a methodology to size the PV module and battery pack considering system availability (in the form of loss of load probability) for a standalone solar home system (SHS), while also exploring the boundaries of a single *PBIM* using two load profiles as a reference. The method consists of an iterative process that varies the PV rating and battery capacity while evaluating its impact on loss of load probability (LLP). LLP is defined as the primary criterion, which must be minimized to ensure the continuity of the energy supply to the load. Also, a basic energy management (EMS) strategy that prioritizes load fulfillment either by solar power or battery discharging is proposed. The implementation of this EMS is further explored in chapter 4.

Chapter 4. Energy Management System

In this chapter, the DC coupled architecture is chosen as it can ensure appropriate functioning of the battery, while the complexity of the system is moderate. The converters are managed to define the power flows according to seven modes of operation, which are needed to perform energy management in a standalone and grid-tied PV system case studies. Moreover, the proposed energy management system is able to harvest the energy from the PV panel at the maximum power point, curtail the excess of PV power in cases of overproduction, and take care of the battery charging and discharging processes following the power required by the load.

Chapter 5. Thermal Management

This chapter presents a detailed thermal model of the physical integration of a PV-battery system on the back side of a PV panel. Based on the model, it was found that the temperature of the components is reduced drastically by adding an air gap between the PV panel and the BoS components. This chapter proves that batteries operate in a safe range, even under severe conditions and the temperature can be reduced even further through the use of phase change materials. The Finite Element Method (FEM) model was validated using a lab testing set-up. The results of this chapter are fundamental to determine a suitable battery technology, which is studied in chapter 6.

Chapter 6. Prototype Testing and Battery Selection

This chapter examines the *PBIM* concept by introducing a framework with the final aim of selecting a suitable battery technology for the *PBIM*. For doing this, a prototype was tested to characterize its electrical and thermal response via indoor testing designed to reproduce an extreme scenario of high irradiance and low heat dissipation. Here, the battery and PV module temperature are closely monitored until stabilized, setting the highest temperature expected into an integrated module. Based on the information obtained from the indoor testing of the prototype, a battery testing methodology that emulated the conditions expected in an integrated device was formulated. By using the designed battery testing, the state of health (SoH) of two battery technologies (Lithium iron phosphate and lithium cobalt oxide) was measured throughout a cycling test considering two temperature levels: 45°C and ambient temperature (22–26°C).

Chapter 7. Conclusions

The final chapter sums up the general findings of the research project while correlating them with the research questions set in chapter 1. Future research lines and recommendations are also mentioned in this chapter.

1

References

[1] N. Oreskes, *The scientific consensus on climate change,* Science **306**, 1686 (2004), http://science.sciencemag.org/content/306/5702/1686.full.pdf .

[2] Intergovernmental Panel on Climate Change (IPCC), *Climate Change 2014: Synthesis Report. Contribution of Working Groups I, II and III to the Fifth Assessment Report of the Intergovernmental Panel on Climate Change* (2014) arXiv:arXiv:1011.1669v3 .

[3] O. P. Myles Allen, Heleen de Coninck, K. J. Dube, Ove Hoegh-Guldberg, Daniela Jacob, D. S. Aromar Revi, Joeri Rogelj , Joyashree Roy, and W. William Solecki, Michael Taylor , Petra Tschakert, Henri, *Global Warming of 1.5 °C*, Tech. Rep. June (Intergovernmental Panel on Climate Change, 2018).

[4] O. Edenhofer, R. P. Madruga, Y. Sokona, K. Seyboth, P. Matschoss, S. Kadner, T. Zwickel, P. Eickemeier, G. Hansen, S. Schlömer, and C. von Stechow, *Renewable Energy Sources and Climate Change Mitigation: Special Report of the Intergovernmental Panel on Climate Change* (2011) IEA, 2016 .

[5] I. P. on Climate Change (IPCC), *Renewable Energy Sources and Climate Change Mitigation: Special Report of the Intergovernmental Panel on Climate Change* (2014).

[6] International Energy Agency, *Technology Roadmap Solar Photovoltaic Energy,* (2014).

[7] REN21, *Renewables 2018: Global status report*, Tech. Rep. (2018).

[8] IRENA, *Electricity-storage-and-renewables-costs-and-markets*, October (2017) p. 132.

[9] E. Tervo, K. Agbim, F. DeAngelis, J. Hernandez, H. K. Kim, and A. Odukomaiya, *An economic analysis of residential photovoltaic systems with lithium ion battery storage in the united states,* Renewable and Sustainable Energy Reviews **94**, 1057 (2018).

[10] A. S. Hassan, L. Cipcigan, and N. Jenkins, *Optimal battery storage operation for pv systems with tariff incentives,* Applied Energy **203**, 422 (2017).

[11] A. Jäger-waldau, *PV Status Report 2016*, October (2016).

[12] B. Nykvist and M. Nilsson, *Rapidly falling costs of battery packs for electric vehicles,* Nature Climate Change **5**, 329 (2015).

[13] R. Fu, D. Feldman, R. Margolis, M. Woodhouse, and K. Ardani, *Us solar photovoltaic system cost benchmark: Q1 2017,* Golden: National Renewable Energy Laboratory (2017).

[14] K. Jäger, O. Isabella, A. H. Smets, R. Van Swaaij, and M. Zeman, *Solar Energy: The physics and engineering of photovoltaic conversion, technologies and systems* (UIT Cambridge, 2016).

[15] F. ISE, *Photovoltaics report,* PSE conferences Consulting (2018).

2

Integrating a Photovoltaic Storage System in One Device

Having set the ground in the previous section, this chapter provides an overview of the current trends based on the integration of solar energy and energy storage. Despite the vast literature, there are still several open questions about how to transfer the integration concepts from the lab to real-life applications. Hence, this chapter critically analyzes the challenges that previous studies faced while pointing out the remaining gaps in the field and suggesting future research lines. The chapter is divided into two main sections based on the PV device rating: low (<10 W_p) and high power (>10 W_p). In both sections, the published papers are summarized for PV-supercapacitors and PV-battery devices to identify general trends and challenges. On the one hand, it is concluded that the research efforts focused on lower power solutions are normally not stable enough to perform for long times as required by real-life applications, and they are not easily scalable to supply appliances such as low power cell phone charging. On the other hand, high power devices can already been used in practical applications; consequently, this thesis will be based on high power integrated devices. However, as introduced in this chapter, there is a lack of knowledge about the impact due to the high temperatures on storage devices and its relation to aging, adequate heat management systems, and system sizing. Consequently, chapter 3, chapter 5, and chapter 6 are fundamental to prove the technical feasibility of integrated devices.

This chapter is based on V. Vega-Garita, L. Ramirez-Elizondo, N. Narayan, P. Bauer. *Integrating a photovoltaic storage system in one device: A critical review.* Progress in Photovoltaics Research and Applications (2019) [1].

2.1. Introduction

Solar photovoltaic (PV) energy generation is highly dependent on weather conditions, making solar power intermittent and many times unreliable. Moreover, energy demand is widespread during the day, and solar energy is available for few hours, provoking a mismatch between demand and supply. These two issues are the driving force behind the use of energy storage (ES) devices, which help decrease the fluctuations from the generation side, but also provide the possibility of performing ancillary services. Consequently, it is fundamental to find the most appropriate energy storage device for particular applications and operational conditions.

According to the characteristics of ES devices, the criterion that defines when the energy is stored and utilized may vary, even for the same component. Some ES devices can supply power during extended periods (hours, days), while others are more suitable for shorter periods of operation (seconds, minutes). For instance, rapid changes in PV power due to rapidly changing illumination conditions can be smoothed using supercapacitors (SC); they deliver power when solar supply is scarce, so the load is still satisfied. For devices with lower self-discharging values like electrochemical cells (batteries), the electrical energy produced by a PV generator could be stored immediately for later use, or the battery could supply the energy accumulated in previous times to complement the generation.

Having accepted the fact that solar energy and storage are complementary, there are two forms in which both of them can be combined: via an external circuitry or by physically integrating the components. External connection of components is associated with elevated resistances [2], complicated manufacturing processes [3], rigid and heavy devices [4], and space consuming solutions [5]. By physically integrating a PV-storage system, the current benefits of the synergy solar/storage could be expanded as well as the range of applications for different power levels. The manufacturing process of a complete integrated device is foreseen as one of the main motivations of the physical integration, because it might mean a reduction of the amount of materials and energy in comparison to separately fabricating all components.

Also, integrated devices typically result in higher volumetric and gravimetric energy density devices when compared to solar systems with separated components, due to a reduction on wiring, the sharing of common encapsulation or electrodes, and more compact devices. Another benefit of physically integrated devices is the possibility of having self-sustaining devices and partially-self-sustaining devices, opening the door for portable solutions, where no external power sources are required. Furthermore, user-friendly devices that are easy to install and use are also considered advantages in these sort of applications.

2.1.1. Related literature

Over the past years, several review papers have explored the combination of solar cells and energy storage in one single component like [6], indicating the features of the proposed approaches for particular applications. For instance in [7], the state of the art of self-powered systems is introduced, while fibre-shape power devices have been studied in [8]. Similarly, many papers have summarized and discussed the trends and perspectives of the integration concepts [9, 10]. Among them, particular attention

has been paid to understand the challenges and advances of printed flexible PV power systems, revising the progress on flexible solar cells, batteries and power electronics individually [3]. The developments on nano-structured flexible electrodes and structural designs towards shape-conformable devices have been introduced and summarized in detail [4]. Specific interest has been given to the variety of materials that can be combined to build devices that unite dye-sensitized solar cells and supercapacitors, where particular attention has been drawn to carefully selecting the materials to achieve components with appropriate performances [11]. Moreover, the current issues and future research directions for various devices that integrate different types of solar cells and supercapacitors technologies have been analyzed [5, 12]. Also, in [13, 14], the system configuration and working principles of the combination of solar, mechanical, or thermoelectric generator have been reviewed when combined with electrochemical cells or supercapacitors.

However, despite the reviews mentioned above, just a few articles have highlighted the limitations and features that make one of the combinations, solar-battery or solar-supercapacitor, better than the other depending on the applications as this review chapter intends. As a consequence, this chapter gives the opportunity to evaluate both combinations in a common frame. Moreover, to the best of our knowledge, this chapter combines all the relevant efforts related to the physical integration of solar cells and energy storage, from low to high power devices — PV rated power more than 10 W_p.

Additionally, especially novel in this chapter is the focus on high power devices similar to the *PV-battery Integrated Module*. These kind of concepts have been neither covered nor the gaps and challenges elucidated.

2.1.2. Contributions

This chapter contributes to

- analyze the trends and most relevant research on PV-supercapacitors and PV-batteries for low power approaches (section 2.3.2 and 2.3.3),
- identify general and particular challenges for physically integrating solar and energy storage in low power applications (section 2.3.4 and 2.3.5),
- gather the efforts to combine solar and storage devices for high power solutions (section 2.4), and
- identify and analyze the most relevant challenges and gaps for high power applications contributing to the formulation of chapter 3, 5, and 6 (section 2.4.5).

2.2. Methodology of the review

2.2.1. Criteria for selecting papers

All the papers collected in this chapter were found using the general searching terms that Table 2.1 introduces. The literature survey focuses on the integration of PV devices and energy storage technologies, i.e., electrochemical cells and supercapacitors. Approaches that include water-splitting devices, or bio-inspired concepts are not considered within the scope of this study. The bibliographic references were selected based

on quality (highly cited, from renown journals, clear, etc.), and novelty (new concepts, high efficiencies, new materials, etc.) of the introduced concepts.

2.2.2. Criteria for classifying papers

For classification purposes, the papers were divided into two categories: high power and low power devices. Devices with a PV generation rated power less than 10 W_p were considered low power solutions, whereas devices able to deliver more than 10 W_p were classified as high power, as stated by [15]. In order put this value in perspective, charging a cell phone requires from 1 up to 10 W. Accordingly, a low power integrated device would barely be capable of charging a mid-power cell phone (10 W).

Table 2.1: Searching terms for literature study

	Combined with AND		
Combined with OR	Physical Integration	Solar cell	Batteries
	One device	Solar module	Lithium ion
	Combined	Solar panel	Accumulator
	Monolithic	PV module	Electrochemical cell
	Integrated Module	Photovoltaic panel	Supercapacitor
	All in one	Photovoltaic module	Energy storage
		Photo battery	
		Solar battery	
		Photo capacitor	
		Solar capacitor	

2.3. Low power PV-storage devices

This section introduces various efforts for physically integrating solar cells, supercapacitor, and electrochemical cells that result in low power devices. Here, the general structures followed to combine storage and solar energy are presented along with the main trends and challenges that both types of devices face. Also, the most promising applications are introduced to describe their level of readiness to become widespread solutions.

2.3.1. Overall efficiency

To estimate the overall efficiency (η_{ss}) of an integrated device, a formula that considers the individual efficiencies of the energy sources is written as follows:

$$\eta_{ss} = \eta_{sc}\eta_s, \tag{2.1}$$

where η_{sc} is solar cell efficiency and η_s energy storage efficiency. By using Equation 2.1 as a reference, all solutions could be compared using the same expression. This is important because many papers have considered other ways of estimating η_{ss}, making difficult fair comparisons across articles. The η_{ss} values provided by Tables 2.2, 2.4,

and 2.6 utilizes Equation 2.1 as long as the information about individual efficiencies is provided. In these tables, the procedure followed to measure or calculate η_{sc} and η_s are also mentioned if details are provided by the authors of the reviewed papers. Moreover, power conversion devices such as DC/DC converters are generally not added in low power concepts; consequently, the efficiency term related to power conversion is not considered in equation 2.1.

2.3.2. Solar cells and supercapacitor

Supercapacitors (SC) are capacitors with high values of capacitance but low voltage. In general terms, they are located between electrolytic capacitors and rechargeable batteries in terms of energy density. Among the most important characteristics of supercapacitors are low maintenance, high performance, and long cycle life [16]. As mentioned before, supercapacitors are more suitable for power (short-term storage) than for energy applications (long-term). Consequently, the devices in this section are mainly designed to make the solar cell output power more stable.

When a solar cell is exposed to light, the voltage increases and as soon as the cell is not illuminated, the voltage returns immediately to zero (Figure 2.1). However, if the solar cells are connected to a supercapacitor, the voltage of the device does not decrease immediately to zero. Therefore, the power delivered is not interrupted when light is not available. Because the power is not interrupted, integrated devices provide more reliable power output, which facilitates its use in a broader range of applications.

How are supercapacitors and solar cells integrated?

Devices that combine solar cells and supercapacitor are referred as a solar-capacitors or photo-supercapacitors (PSC). In these devices, multiple solar cells technologies (e.g., dye-sensitized, organic, perovskite, and silicon) and supercapacitor types (double layer, pseudo-capacitors, and hybrid) have been combined following different approaches. Although previous research has explored the combination of solar cells and supercapacitors when they are connected by external cables, these are not considered entirely integrated solutions. In fully integrated devices, the solar cell and the supercapacitor must either share a common electrode [12] or at least the same substrate. This electrode facilitates the charge transfer while reducing resistance losses due to wiring in comparison to not integrated approaches. The majority of these integrated devices exhibit a planar (monolithic) structure or a fibre-shaped configuration as introduced in Figure 2.2.

Planar structure

In planar or monolithic structures, the solar cell is at the top receiving the incident light, while the supercapacitor is placed at the bottom of the device, and as Figure 2.2a shows they are typically connected in series. According to the materials and working principle of the solar cell and supercapacitor, different ideas of integration can be realized; however, there are three main configurations: two-electrode, three-electrode, and four-electrode modes [13].

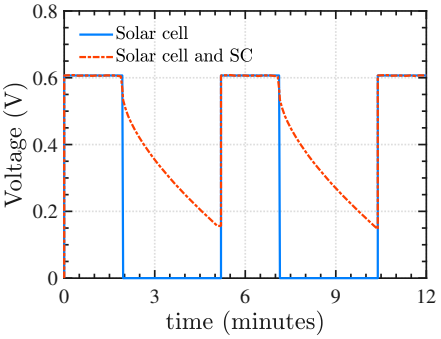

Figure 2.1: Response of a single solar cell and a solar cell coupled with a supercapacitor during intermittent illumination. If light is on, the voltage of a single solar cell is around 0.6, but when light is off the voltage decreases to 0. In cases where an appropriate SC is used, the system voltage does not decrease to zero intermediately in the absence of light. This figure is based on [17], where the illumination period was 2 min followed by a 3 min discharging process at a constant discharging current density of 40 μA cm^{-2}.

Two-electrode mode

The two-electrode mode is the most integrated of the approaches because the rear electrode of the solar cell is shared with the SC while reducing materials and increasing the energy density of the device. However, when combining a dye-sensitized solar cell (DSSC) and an SC in a two-electrode configuration [18], the device presented particular issues. One problem occurred during the discharging process because the electrons from the counter electrode were not able to easily cross the TiO_2 layer towards the shared electrode. The diffusion of iodine ions caused the second problem, as the SC electrolyte short-circuited or self-discharged the device. These difficulties resulted into a device with lower efficiency in comparison to a three-electrode mode device presented by the same authors [19], as the two-electrode mode exhibited a higher resistance.

Three-electrode mode

Due to the problems mentioned above, an intermediate electrode is added to separate the DSSC and the SC, forming a three-electrode structure. By adding this barrier, solar cells and supercapacitors can operate individually or together when supplying the load, which is not possible in the two-electrode case. In a three-electrode configuration, the counter electrode fulfills a double purpose; it functions as a redox electron transfer surface and as charge storage.

Fibre structure

When compared to a planar structure, fibre-shaped or wire-type devices follow the same physical principles; the difference lies in the arrangement of the components. They are classified as core-shell (or coaxial), twisted, and parallel-like structures [5]. Besides the structure itself, all of these devices share a common substrate in the form of a fibre. Plastic, elastic rubber, and metal wires have been used as mechanical support and to assemble the solar cell part and the supercapacitor in cores-shell structures. In the case

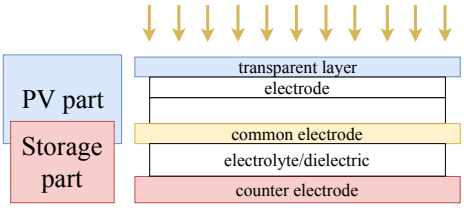

(a) Monolithic structure.

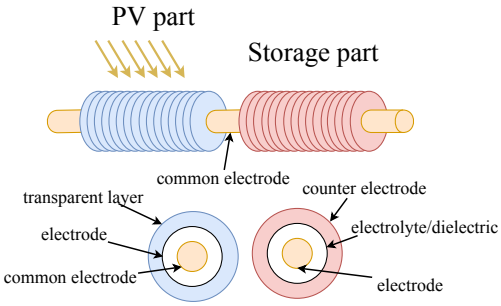

(b) Fibre structure.

Figure 2.2: Two possible structures for integrated devices: (a) planar or monolithic three-electrode structure and (b) coaxial fibre parallel structure.

of twisted devices, the substrate fibres with the solar cell and supercapacitor are rolled to achieved the required spiral-shape, while for parallel-like structure the mechanical stability normally improved by having the two fibres placed in parallel (Figure 2.2). While fibre-shaped solutions are less energy efficient when compared to a planar structure, their mechanical properties enable them to be used in wearable and portable low power applications [8].

How does a photo-supercapacitor work?

The PV part converts the incident light into electrical energy generating hole-electron pairs while promoting electrons to high energy levels and holes remain at low energy level. The exited electrons accumulate at one side of the capacitor and holes in the other electrode until the capacitor saturates.

Figure 2.3 depicts the working principle of a solar supercapacitor implemented using a dye-sensitized solar cell (DSSC) for a three-electrode configuration. In these devices, photo-excited electrons from the dye reach the conduction band of a semiconductor, generally TiO_2. Later, the electrons flow to the transparent conducting electrode, which is externally connected to the supercapacitor where they are stored. This process is possible because negative electrolyte ions, frequently I^-, are combined with positive charged dye molecules allowing its regeneration and keeping the photo-generation process. The charging process continues as the redox reaction (I^-/I_3^-) in the electrolyte is sustained by the electrons provided from the shared electrode. The supercapacitor

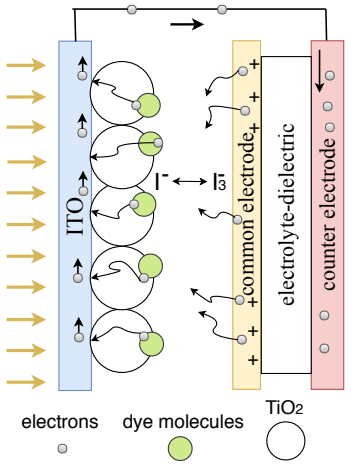

Figure 2.3: Working principle of a dye-sensitized solar cell coupled with a supercapacitor.

can be charged until saturation; however, if light intensity weakens or disappears the opposite process occurs and the device discharges.

Relevant papers and trends

Tables 2.2 and 2.4 summarize the variety of research carried out when integrating solar cells and supercapacitors; the papers are classified based on the year of publication, solar cells technologies, the structure of the device, type of supercapacitor, power, efficiencies, and capacitance. From this table, it is evident that since 2004, when the first paper was published, the articles have focused mainly on the integration of DSSC and different types of supercapacitors. The preference for DSSC over other solar cell technologies lies in its easy manufacturing process, but also because supercapacitors and DSSCs share a similar structure which facilitates its physical integration [5].

Later on, organic solar cells (OSC) have also been combined with SCs. OSCs have expanded the range of applications for integrated devices, e.g., in portable and wearable solutions. Among the many merits of OSCs, its flexibility, lightweight, and transparency are the most remarkable [20, 21]. Furthermore, OSCs low costs and ease of manufacturing (roll-to-roll) underline its potential and interest in physically integrated devices [22]. Although the efficiencies of OSCs need further improvements, the utilization of OSCs eliminates the need for liquid electrolytes when compared to DSSC concepts, making more stable and robust integrated devices. An OSC and graphene-based supercapacitor were combined following an in-plane or parallel structure in [23]; the method presented is considered suitable for roll-to-roll manufacture, and convenient for future self-sustained applications. Nonetheless, after connecting 5 OSCs in series the voltage of the device was about 5V with a low conversion efficiency of almost 1.6%.

In an effort to achieve more efficient and powerful integrated devices, perovskite solar cells (PVSC) and supercapacitor have undergone extensive investigation. The result of this combination has produced devices that excel when compare to other devices. As Figure 2.4 indicates, the device with the highest PV output (13.6 mW cm^{-2})

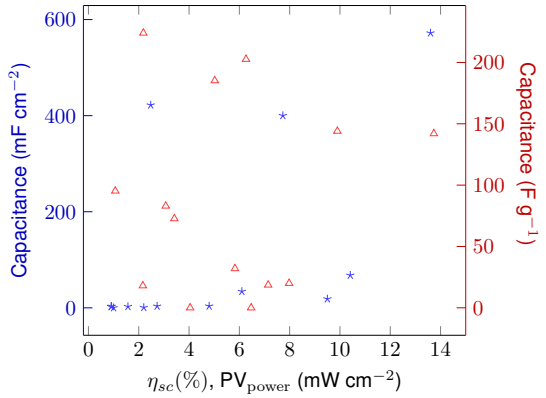

Figure 2.4: Trends in photo-supercapacitors. The data for this graph were taken from Tables 2.2 and 2.4 for devices tested at 1 sun condition. At the top right, two devices are characterized by high capacitances and solar efficiencies. Triangular markers correspond to capacitance in Fg^{-1} and star markers to capacitance in $mFcm^{-2}$.

and capacitance per unit area (572 mF cm^{-2}) is based on union of PVSC and SC. In [24], OSC and PVSC-based devices were integrated following the same structure and using supercapacitor technology, concluding that as expected PVSC integrated device outperforms OSCs, by a factor of two in this case. As can be seen from Tables 2.2 and 2.4, devices with efficiencies above 10% are possible when high efficient PVSCs have been combined with conventional SC [24, 25]. Although not so frequently, a-Si and c-Si solar cells have also been researched with acceptable overall efficiencies [17, 26, 27].

Regarding the materials used as electrodes in the SC part, activated carbon is usually chosen in double-layer capacitors due to its low cost, extensive surface area, and chemical stability. To face the challenges of having a liquid electrolyte, multi-walled carbon nanotubes are used in all-solid integrated devices to achieve a more energetically compact device [28].

Moreover, pseudocapacitors made of metal oxides and conductive polymers have been employed as electrodes in various SC coupled to solar cells. Conductive polymers (such as PEDOT and PANI) are selected because they are easy to manufacture and able to reach relatively high capacitance values. In the case of metal oxides (like TiO_2), the devices perform deficiently due to their high electrical resistance when selected as intermediate electrodes [29].

Although not very often, hybrid SCs have also been investigated as a consequence of its tunable voltage levels and elevated capacitance values. This combination, however, has resulted in devices with low-efficiency [30].

2.3.3. PV and battery

Unlike supercapacitors, batteries are able to store energy for more extended periods with low self-discharging rates. This feature makes batteries an appropriate technology to manage the mismatch between solar generation and energy demand because the

sun shines for a limited time and it is not able to supply power during the night. Batteries can also smooth the output of the solar cell, similarly to the supercapacitor, although its response capacity is limited because high power requirement from the load could damage the batteries. Currently, batteries are part of PV-storage systems because of their stability, reasonable price, low maintenance cost, and maturity [16].

An electrochemical cell is a device that is able to store energy in a chemical form as a result of electric stimuli. In an electrochemical cell, a material (electrode) reduces while the other electrode oxidizes, in which the overall system remains in equilibrium because the electrons flow from one electrode to the other. As the electrodes cannot touch each other, an electrolyte is needed to provide electrical insulation while acting as a medium for the ions to diffuse.

How are solar cells and batteries integrated?

Photovoltaic charging devices as well as photocatalytic charging systems have been explored when integrating batteries and solar cells. In photovoltaic charging devices, the battery and solar cells obey independent physicochemical processes, while in photocatalytic devices, photo-induced interdependent redox reactions occur during the charging process. Integrated devices that contain silicon, organic, or perovskite solar cells are classified as photovoltaic charging devices. Conversely, dye-sensitized and quantum dye-sensitized solar cells belong to the category of photo-catalytic devices [13]. Solar cells and batteries have been integrated following mainly planar structures with differences in the electrode configuration: two-electrode (2E) and three-electrode (3E). In three-electrode devices (Figure 2.2a), there is a clear distinction between the storage and generation part, although they share a common counter electrode [2]. Alternatively, other articles have introduced devices composed of two electrodes, where one of them works as a photo-electrode and the other functions as an energy storage electrode. Hence, the device is considered as a single entity as there is no physical division in the middle of the generation and storage parts.

How does a photo-battery work?

In 3E devices, when photons strike the photo-active material, some electrons increase their energy and can reach the conduction band while producing holes. If the voltage provided by the solar cell is enough to activate the electrochemical charging process inside the battery, the electrons from the solar cell move to the batterys anode, where they recombine with the cations released by the cathode. Alternatively, the holes from the solar cell recombine with the electrons generated by the oxidation in the cathode. As soon as the light source is not present, the opposite phenomenon occurs, and the batteries discharge if a load is added to extract the energy accumulated [31].

However, 2E structured components follow a different working principle. In the photo-electrode material, one chemical element oxidizes while in the counter electrode another substance reduces. An example of this kind of devices was explored in [60], where a conventional DSSC was modified substituting the I^-/I_3^- electrolyte with a lead-organohalide. The device resulted in a dual-function rechargeable solar-battery with an overall efficiency close to 7%.

Table 2.2: General characteristics of published research on photo-supercapacitors from 2004–2015. [a] Testing at one sun (1000 W/m^2), [b] parameters estimated from I-V curve, [c] testing at specific conditions, [d] parameters obtained from a complete charging-discharging process, [e] overall photo-storage efficiency, [f] parameter calculated using cyclic voltammetry, [g] parameter calculated based only on a charging or discharging process, [h] parameter calculated according to a equation proposed by the authors, [i] parameters estimate for one device isolated of the other, [j] parameter given by the manufacturer, [k] parameter obtained for the device with the highest performance, [l] efficiency calculated by the authors of this paper using Equation 2.1, [m] parameter calculated by the authors of this paper based on provided information.

Year	Ref	Structure	PV	SC	PV (mW cm^{-2})	η_{sc} (%)	η_s (%)	η_{ss} (%)	Capacitance (mF cm^{-2})* (F g^{-1})**
2004	[18]	Planar (2E)	DSSC	Activated carbon (LiI-doped)	–	–	80[d]	–	690*
2005	[19]	Planar (2E,3E)	DSSC	Activated carbon (LiI-doped)	–	–	42[d](3E)	–	650*[g] (3E)
2011	[32]	Planar (2E)	DSSC	PEDOT(MWCN)/$LiCF_3SO_3$ (PC)	–	–	–	–	95**[g]
2012	[33]	Coaxial/fibre (2E)	DSSC	CNT/PVA/H_3PO_4/Ti	–	2.2[a]	–	1.5[e]	0.6*
2013	[34]	Planar (3E)	DSSC	Ti/TiO_2/ZrO_2/TiO_2/Ti	0.2178[b]	–	–	–	0.14*
2013	[35]	Planar (2E,3E)	DSSC	Ag/$RuO_x(OH)_y$/nafion/FTO (3E)	0.92[a]	0.92	87.8[d] (3E)	0.8[h]	3.26*[g]
2013	[36]	Planar (comb)	DSSC	PET/Ni/Carbon	–	0.27[a]	–	–	2.89**[f]
2013	[37]	Planar (3E)	DSSC	Ag/RuO_x(-OH)$_y$/nafion/FTO	2–3[a]	2–3	87.8[d]	0.8[h]	3260*[a]
2013	[28]	Planar (3E)	DSSC	MWCNT/PVA-H_3PO_4/FTO	2.31[a]	2.31[a]	34	0.79	83**[f]
2013	[38]	Planar/fibre (2E)	DSSC	PVDF/ZnO/FTO	2.23-4.36[a]	7.32[a,k]	–	3.7[e]	20**
2014	[26]	Planar(2E)	Si-poly	Porous Si	–	14.8[j]	84[a,d]	12.43[k]	0.014*[h]
2014	[39]	Coaxial	OSC	Ti/PVA/H_3PO_4/MWCNT	1[a,k]	1.01[a,k]	65.6[f]	0.82[a,k]	0.077*[h]
2014	[40]	Coaxial	DSSC	Ti/TiO_2/PVA/H_3PO_4/Ti	2.7[a]	2.73[a]	75.7[h]	2.07[a]	3.32*[f]
2014	[41]	Planar (3E)	DSSC	Pt/Au/PVDF/FTO	3.3	–	–	1.33–3.38[a]	0.017**[g]
2014	[42]	Coaxial	DSSC	MWCNT/PVA/H_3PO_4	6.47	6.47[a]	–	1.83[h]	18.6**[f]
2014	[30]	Planar	DSSC	Co-doped NiO/AC	5,12	4.9[a]	54[d]	0.6	32**[f]
2015	[43]	In plane	PVSC	polypyrrole-based	13.6	13.6[a]	–	10[h]	572*[f]
2015	[44]	Planar	QDSSC	MWCNT/FTO/Ag/$LiCF_3SO_3$	–	–	–	3.45[c]	150**[f]
2015	[45]	Planar meshed (3E)	QDSSC	carbon/Cu_2S/Na_2S/S/KCl	–	2.66[a]	–	–	72.7**[f]
2015	[46]	Planar(2E)	DSSC	Liquid(l) or quasi-solid electrolyte	–	5.78[a] (l)	–	–	0.0046**
2015	[47]	Planar(3E)	DSSC	Ionic polymer	4.8[a]	4.8[a]	80[d]	2.1[f]	3.5*
2015	[23]	In plane	OSC	Al/graphene/ITO	–	1.57[a]	–	–	2.5*[f]
2015	[48]	Separated	DSSC	b-cyclodextrin/PVP/$MnCO_3$	–	5.57[a]	–	–	202.6**[f]
2015	[49]	Planar	DSSC	PEDOP/V_2O_5	–	1.4[a]	–	–	224**[f]
2015	[50]	In plane	PSC	CNT/PVA-H_3PO_4/PANI	4.3[a,k]	4.3[a,k]	72.1[g,k]	3.1[k]	185.2**[h]

Table 2.4: General characteristics of published research on photo-supercapacitors from 2016–2017. [a] Testing at one sun (1000 W/m^2), [b] parameters estimated from I-V curve, [c] testing at specific conditions, [d] parameters obtained from a complete charging-discharging process, [e] overall photo-storage efficiency, [f] parameter calculated using cyclic voltammetry, [g] parameter calculated based only on a charging or discharging process, [h] parameter calculated according to a equation proposed by the authors, [i] parameters estimate for one device isolated of the other, [j] parameter given by the manufacturer, [k] parameter obtained for the device with the highest performance, [l] efficiency calculated by the authors of this paper using Equation 2.1, [m] parameter calculated by the authors of this paper based on provided information.

Year	Ref	Structure	PV	SC	PV (mW cm^{-2})	η_{sc} (%)	η_s (%)	η_{ss} (%)	Capacitance (mF cm^{-2})* (F g^{-1})**
2016	[27]	Planar(2E,3E)	a-Si SC	Co-Al LDH/ACT/ACT/graphene	–	22[j]	3.87[d]	–	145**[g]
2016	[51]	Planar(3E)	PVSC	CuOHNT/KOH/PVA	$\sim$ 10.41[a]	10.41[a]	–	–	46–67.78*[f]
2016	[52]	In plane	DSSC	SWCNT/Buckypaper-based/PVA/KOH	–	0.26[a]	–	–	62.5–95.25**[f]
2016	[21]	Planar	OSC	steel/carbon/gel-polymer electrolyte	–	5.2[i]	–	2.9[c]	50–130*[i]
2016	[53]	Planar (3E)	PVSC	PEDOT-carbon/FTO	–	6.37[i]	73.77[h,k]	4.7[a,k]	10.8–12.8*[f]
2016	[25]	Planar (3E)	PVSC	WO_3/PVA/H_3PO_4	–	–	–	3.73–11.89[b]	28.7–43.1*[g]
2016	[54]	Planar (2E)	DSSC	$WO_3 \cdot H_2O$/CNT/PVDF	–	–		2.2[a,k]	195[f,k] F cm^{-3}
2016	[17]	Planar (3E)	c-Si	Al/MoO_x/$NaSO_4$	–	6.1[a]	–	–	34*[f]
2016	[55]	Coaxial/Fibre	DSSC	PDMS/Cu/PVA/H_3PO_4	–	5.64[a]	–	–	1.9[f] mF cm^{-1}
2016	[56]	Coaxial/Fibre	DSSC	Ti/TiN/KOH/PVA	–	0.9[a]	85[d]	–	2.28*[f]
2017	[57]	Planar (4E)	DSSC	steel/graphene/PVDF	–	1.38[a]	73.91	1.02[h]	10–18**[f,h]
			PVSC			13.2[a]	80.31	10.97[h]	142**[g]
2017	[24]	Planar (3E)	OSC	graphene oxide/PVA/H_3PO_4	–	9.28 [a]	64.59	5.07[h]	144**[g]
2017	[58]	Planar (3E)	DSSC	PANI/TiO_2/PVA/H_3PO_4/carbon	–	7.73[a]	–	6.5[h]	250–400*[f]
2017	[59]	Planar/fibre (3E)	PSC	PANI/CNT	–	2.476[a]	70.6[d]	1.74[h]	422*[f]
2017	[29]	Coaxial/fibre	DSSC	CF/TiO_2/MoS_2	–	9.5[a]	–	1.8*[h]	18.51*[f]

Relevant papers and trends

2E configurations have been extensively explored, where various combinations of materials for anodes and cathodes were tested in redox cells to evaluate their effectiveness to produce and store solar energy. One of the first attempts at integrating a dye-sensitized solar cell and an electrochemical device in one component consisted of using WO_3 as a charge storage layer [61]. For more details, a comprehensive list was developed by Yu et al. in [62], in which the published papers were classified based on catholyte redox couples, photoelectrode, active anodes, transport ion, solvent, membranes, voltages, and discharged currents. As a consequence of the variety of types of materials, the compatibility of the electrodes and the selection of appropriate electrolytes is fundamental for long-term stability, but also to achieve adequate performance. Although few devices have been able to exhibit overall efficiencies above 10% like [63], the short-term and mid-term stability of the devices along with the low voltage output have been considered one of the main problems behind these approaches. One way to increase the voltage is by using Li ions as the active anode because it results in devices with comparable voltages as individual Li-ion batteries. An example of this was introduced by [64], where the delithiation of lithium iron phosphate nanocrystals is produced by its interaction with light, opening the door to photo-rechargeable lithium-ion batteries, which presents a considerable advance in the field of solar and energy storage. However, the overall efficiency was low 0.06–0.08%. Along the same line, a Li-O_2 light-assisted battery was suggested [65], with similar voltage values (2.72–2.83 V) and deficient stability.

Because of these limitations, currently, three-electrode configurations have been examined more extensively than two-electrode structures as can be seen in Table 2.6. In this table, various research papers are classified based on the PV generation technologies, device structure, type of battery, power, storage and generation efficiency, overall efficiency, and battery capacity. Also, based on Tables 2.6 and 2.7, Figure 2.5 compares different approaches and battery technologies.

As Si have been intensively used for making solar cells, different types of Si solar cells have been combined with batteries. One remarkable concept was introduced in [66], where a nanowire-based multijunction Si photovoltaic device shared a Si substrate with a $LiCoO_2$ battery which had a Si nanowire anode. Another triple-junction solar cells made of amorphous and microcrystalline silicon was used to charge a lithium-ion battery and demonstrate the potential of an integrated solar cell-to-battery cell monolithic device, with a battery capacity of 0.15 mAh and overall efficiency of 8.8% [67]. Moreover, a silicon-on-insulator manufacturing process was introduced to fabricate multiple solar cells and scale up the overall cell voltage [68]; here, an array of 25 cells has been integrated with a micro-battery to act as a mini generator, producing a maximum power of 1.7 mW. The open circuit voltage of the solar cells could be scaled from 3.6 V (9 cells) until 101.5 V if 169 cells are connected in series. Thin film solar cells have also been explored. For instance, in [69], the fabrication and characterization of a harvesting device that integrates a thin-film solid-state rechargeable battery was introduced, showing a 0.1%/cycle reduction on battery capacity and a generation-storage efficiency and maximum power point of 7.03% and 150 mW, respectively.

Dye-sensitized solar cells have also been combined with batteries following a three-

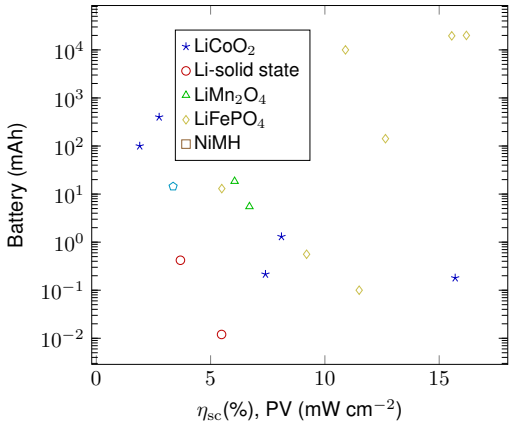

Figure 2.5: Trends in solar battery systems. The data for this graph were taken from Table 2.6 and 2.7 for devices tested at 1 sun conditions. High power solution are located at the top right of the graph.

electrode configuration. As presented in Figure 2.6a, the device has a Ti common electrode in which TiO_2 nanotubes were grown to be part of the DSSC (orange) and Li-ion battery (green). At the top, the TiO_2 nanotubes covered by dye molecules work as electron collectors that when hit by the light transfer exited electrons first to the Ti electrode, and later to the TiO_2 battery anode where they are stored. Also while charging the Li^+ move to the anode maintaining the electrochemical equilibrium. For this device, the overall efficiency was 0.82% and the battery capacity 38.39 μAh [70].

Moreover, a few organic solar cells have been physically integrated. A bendable module (1 mm) made utilizing an organic PV cell, charging electronics, and a rechargeable battery (NiMH) was introduced in [71]. There, two devices with different voltages (6 and 24 V) were tested and charged after 4 h under 1-sun condition. On the same line, a previous study integrates a thin film solar cell and Li-ion polymer (100 mAh, 3.3 g, ans a thickness less than 1mm) [72].

Although not so common, as Table 2.6 suggests, batteries and PVSC have been studied. Four $CH_3NH_3PbI_3$ perovskite solar cells placed in series have been employed for charging a Li-ion battery made of a $LiFePO_4$ cathode and a $Li_4Ti_5O_{12}$ anode. The device reached an overall efficiency of 7.80% and a good cycling stability [74]; however, the fabrication process must be revised carefully before the device can be implemented in practical applications, as indicated by the authors.

Table 2.6: General characteristics of published research on solar-batteries. [a] Testing at one sun (1000 W/m^2), [b] parameters estimated from I-V curve, [c] testing at specific conditions, [d] parameters obtained from a complete charging-discharging process, [e] overall photo-storage efficiency, [g] parameter calculated based only on a charging or discharging process, [h] parameter calculated according to a equation proposed by the authors, [i] parameters estimate for one device isolated of the other, [j] parameter given by the manufacturer, [k] parameter obtained for the device with the highest performance, [l] efficiency calculated by the authors of this paper using Equation 2.1, [m] parameter calculated by the authors of this paper based on provided information.

Year	Ref	Structure	PV	Battery	PV (mW cm^{-2})	η_{sc} (%)	η_s (%)	η_{ss} (%)	Capacity (mAh)
				$LiMn_2O_4$					0.8
2002	[75]	Planar	GaAs	$LiNiCoO_2$	–	12.8[c]	–	–	45
2002	[61]	One device (2E)	DSSC	WO_3/$LiWO_3$ /LiI/LiI_3	–	–	–	–	0.167[a,h]
2007	[72]	Planar	OSC	$LiCoO_2$/graphite	1.9[a]	1.85[a]	–	–	100[j,k]
2009	[76]	Planar	a-Si	$LiCoO_2$ Li-ion solid state	3.68[j]				0.42[j]
2010	[77][78]								
2011	[79]	Planar	OSC	$LiCoO_2$/graphite	–	1.02-2.75[a]	–	–	105–400[a]
2011	[68]	Parallel	c-Si	SiO_2/$LiMn_2O_4$	2.07–6.7[a]	1.5-6.5[a]	–	–	5.5[i]
2012	[80]	Planar (3E)	Si	Si/$LiCoO_2$	–	–	–	–	–
2012	[70]	Planar	DSSC	$LiCoO_2$	–	–	41	0.82[h]	0.039[g]
2012	[81]	Planar (3E)	DSSC	carbon/$LiClO_4$/ PPy/FTO	–	0.1[a]	–	–	8.3 g^{-1} [g]
2013	[82]	Planar	OSC	$LiFePO_4$/ $Li_4Ti_5O_{12}$	–	5.49[a]	–	–	13
2013	[69]	Planar	α-Si	Nb_2O_5/LiPON/ $LiCoO_2$	–	7.4[a]	95[d]	4[h]	0.215[g]
2013	[83]	Planar	c-Si	Li-solid state	–	5.48[a]	–	–	0.012[i]
2014	[84]	Planar	a-Si	Li/LiPON/ $LiCoO_2$	–	–	–	–	0.3[j]
2015	[74]	Planar/ series	PSC	$LiFePO_4$/ $Li_4Ti_5O_{12}$	–	12.65 [a,i]	–	7.8[g,h]	142.1[g] g^{-1}
2015	[71]	Planar	OSC	NiMH	3.36[a]	–	–	–	5.5–14.4[j]
2015	[60]	Planar	DSSC	Lead organohalide	–	–	81.5[d]	8.6[a]	–
2016	[67]	Planar	a-Si:H	$LiFePO_4$/ $Li_4Ti_5O_{12}$	–	9.2–11.5[a]	–	8.8[h,k]	0.1[g]
2016	[85]	Planar	a-Si	graphite/ $LiCoO_2$	–	4[j]	99.9[d]	–	47.5 [d]
2016	[86]	Planar	a-Si:H	$LiFePO_4$/ $Li_4Ti_5O_{12}$	–	9.2[a]	–	8[g,h]	0.56[d]
2016	[87]	Fibre	DSSC	$LiMn_2O_4$/ $Li_4Ti_5O_{12}$	–	6.05[a]	95[g]	5.74[l]	18.48[m]
2017	[88]	Planar(3E)	a-Si:H/ μc-Si:H	Li/LiPON/ $LiCoO_2$	–	8.1[a]	99.9[d]	8[l]	1.3[m]
2017	[73]	Planar	c-Si	$Li_4Ti_5O_{12}$/ $LiCoO_2$/Al	–	15.7[a]	–	7.61[h]	0.18 [g,m]

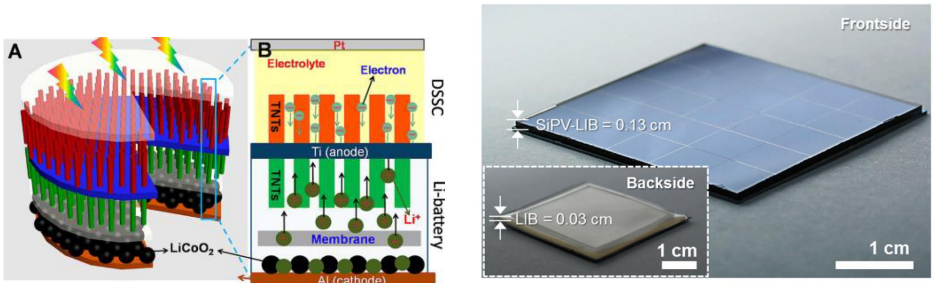

(a) (b)

Figure 2.6: (a) Three-electrode nanotube based integrated solar battery device. Reprinted with permission from [70]. Copyright 2012, American Chemical Society. (b) Monolithic integration of solar cell and solid state Li-ion battery for a more easy manufacturing process. Reproduced from [73] with permission from the The Royal Society of Chemistry.

In order to improve the manufacturing process of integrated devices, a new method of assembly has been presented to favour an easy and scalable manufacturing process [73], opening the possibility of using this portable solar-batteries for low consumption electronics. The monolithically integrated approach uses 25 c-Si photovoltaic cells in series producing a total voltage of 14.1 V (Figure 2.6b) and a bipolar printed solid-state $Li_4Ti_5O_{12}$ battery. The complete device has a total area of 9 cm^2 with an overall generation-storage efficiency of 7.61%, while the battery is completely charged in 2 min and discharged at 28 C-rate. With the same objective, the roll-to-roll manufacturing process can be used to directly integrate an organic solar cell and pouch li-ion cell, providing a fast manufacturing process [79].

2.3.4. General perspectives and gaps

Because batteries and supercapacitors are combined following similar approaches and are integrated with the same photovoltaic technologies, they face common challenges to become viable concepts for high power systems, which are addressed as part of this section.

Materials compatibility

When building PSCs and solar batteries, the compatibility of active materials is primordial. For instance, their appropriate selection helps reduce electron recombination and increase conversion efficiency [5]. At the same time, the selected materials should not chemically react between them to ensure long-term stability. However, choosing the right redox couple is challenging as only a few of them are available [11].

Fibre devices

In the case of fibre-based devices, it is important to outline the interdependency between performance and fibre length. As the device length increases, the performance of the device decreases [89]; therefore, more developments towards highly conductive electrodes are fundamental. At the same time, new weaving techniques are needed for

more stable and powerful devices [90], especially considering the increasing complexity of more recent devices [91].

Binder issue

In some devices, binders are employed to put in contact the solar cells and the storage part. However, the use of binders is normally counter-productive as they are commonly electrical insulators, that increases the resistivity of the integrated device [4]. Therefore, other techniques to attach both components must be researched to avoid this problem.

Mechanical stability

In flexible devices, special attention must be paid to the metallic pieces, because they tend to fail faster than the other pieces [4]. As a result, more light and flexible materials should substitute these materials in order to achieve more stable flexible devices. Another characteristic that should be improved is the structural design of the integrated devices with the objective of ensuring longer functioning times.

Liquid electrolyte issue

Regular electrochemical cells and DSSC utilize liquid electrolytes to provide a path for the ions to flow, which create potential for possible leakages or evaporation that could compromise the correct functioning of the device [4]. To prevent this problem, there are two possible solutions: improve the capabilities and properties of the encapsulation or focus efforts on the development of devices that operate using solid stated electrolytes [7, 37, 92], but with the inherent compromise on power density. Although solid electrolyte devices have been already built [66], there is still room for improvements on the assembly of the complete device.

Lack of standardized testing protocols

On several occasions, it is difficult to compare the performance of different devices using a common benchmark because there are no protocols to follow [7]. Consequently, efficiency values like those reported in Tables 2.2, 2.4, and 2.6 are normally not comparable as the test and procedures differ. Protocols for measuring efficiencies, lifetime, and mechanical stability should also be defined to quantify the progress on the field of integrated devices.

Long-term feasibility

Normally, published papers are merely dedicated to introducing new types of devices using novel materials or structures instead of providing well-developed devices [13]. Consequently, the devices are not as efficient as they could be and their long-term stability is also questionable [5, 31]. In particular, there is no information about how aging affects parameters such as efficiency, capacitances, PV output, and battery capacity. In summary, little information is available about how feasible is a concept to move from lab-scale to practice. This issue is fundamental in not so mature concepts like flexible devices and fibres [91].

Indoor vs. outdoor

In general, integrated devices can be used for outdoor or indoor conditions; however, indoor testing and applications are more prominent. This is the rule because, in indoor applications, the operational conditions are not as demanding as in outdoor applications [3]. Outdoor conditions imply higher irradiation and temperature, which affects the performance of the devices making the solar generation more inefficient while increasing the risk of system failure. Furthermore, if long-term testing is performed the mechanical stresses due to temperature gradients can deteriorate the lifetime of the components and at the same time reducing the PV generation to the energy storage performance in comparison with indoor cases.

Solar generation and storage mismatch

A notable fact when integrating solar cells and energy storage devices is the mismatch between them, which could be related the physical size of the devices (solar and storage) or by the significant difference in PV rating and energy storage capacity [9]. For e.g., a battery with a capacity much more higher than the energy that the PV cell generate. The mismatch may occur when the physical dimension of one of the components is imposed on the other component [31]. In planar structures, for instance, the physical size of the electrochemical cell or supercapacitor is the same as the solar cell, which often results in electrical under-sizing or over-sizing of the storage part. This mismatch again provokes low-efficient concepts [13], especially when power electronic conversion stages are not utilized.

An example of this problem can be seen in Figure 2.4, where the power produced by the solar cell increases but capacitances remain almost constant (blue star markers). In the same figure, one device clearly outperforms the rest, due to its appropriate PV efficiency and high capacitance (star marker at the top right corner). When considering gravimetric capacitance as a reference, one integrated device presents outstanding features almost 150 F g^{-1} and a solar cell with an efficiency close to 14% [24]. Although according to this metric various devices exhibited acceptable values of gravimetric capacitance (top left red triangles), the efficiency of the solar part needed further improvements.

Constant strive for higher energy density and efficiency

Photovoltaic materials are getting closer to the theoretical maximums [93], with 29.43% reported for c-Si [94] under 1-sun condition. However, these highly efficient materials have not been integrated with SC or electrochemical cells. Additionally, as Figures 2.4 and 2.5 suggest, solar cells with efficiency bigger than 15% have not been explored[1].

From the battery's point of view, appropriate materials to achieve high energy storage capacity and efficiency also need further improvements. Particularly for Li-ion batteries, a goal has been set to double the average energy density to 250 mWh g^{-1} [95], a goal that has not been achieved yet. Therefore, there is significant room for improvement for Li-ion batteries, from which the more commonly used are $LiFePO_4$, $LiCoO_2$, and $Li_4Ti_5O_{12}$ according to Figure 2.5, with $LiFePO_4$ being the most selected in high power applications.

[1] [27] was not included, as details about solar cell testing were not provided.

The increase in power and energy density is needed to prove its feasibility in practical applications, in particular, for low power devices by being able to supply energy to basic loads. In general terms, a low power device should be at least able to supply power to a single white LED, where values of 60 mW are the minimum [96].

Relevance of power electronics

As mentioned before, there is a natural mismatch between solar cells and storage devices. Even if in theory the voltages of both of them are comparable, the system efficiency can be improved by incorporating power electronics units in order to control the storage charging and discharging process. Additionally, the possibility to perform maximum power point tracking (MPPT) is fundamental to obtain appropriate solar-battery efficiency values, but most importantly in solar-supercapacitor systems where the efficiency reduce by half if MPPT is not implemented [3]. In the case of solar-battery systems, the absence of MPPT can be compensated by selecting a PV cell with a voltage similar to the expected nominal voltage of the cell.

Moreover, power electronics conversion stages can aid increasing lifetime of components like batteries by avoiding overcharging and overcharging issues, while ensuring a safe operation. Another important feature of power electronics is that the charging and discharging processes can be decoupled, and the power flows can be managed to perform energy management increasing flexibility of integrated devices [14].

In cases where including power electronics cannot be implemented, a basic electric component, the blocking diode, is crucial as it impedes the discharging of the storage unit to the PV cell that could be seen as a load during dark instances [3].

2.3.5. Particular challenges

Although batteries and supercapacitors are classified as energy storage devices, their natures are different; therefore, their integration with the variety of PV technologies leads to particular issues that are presented as follows.

Solar cells and supercapacitor

When integrating solar cells and supercapacitors, there is a consensus that the higher the possible capacitance values, the better. Therefore, plenty of papers focus on optimizing the design to fulfill this goal. On the other hand, most of the integrated devices are characterized by their low voltages. A device with low voltage is not able to meet the voltage requirements to power even small electronics devices. The relatively low voltage of a photo-capacitor is given by the intrinsic low voltage of both, individual solar cells and supercapacitors. A possible solution to this problem is to connect multiple solar cells in series to increment the voltage, and at the same time more supercapacitors could be connected in series and parallel, in parallel to increase the total capacitance of the device, and in series to also increase the voltage.

Solar cells and batteries

Single junction solar cells exhibit a nominal voltage lower than the voltage of the electrochemical cells. The operational voltage depends on many factors, but the concentration of electrons and holes in the junction primarily defines the PV voltage along with the

semiconductor bandgap [97]. The concentration of holes, electrons, and bandgap is tightly related to the semiconductor material of the cells, where the open circuit voltage of single junction cells is usually around 0.2–1.5 V. While in many cases Li-ion cells have a nominal voltage above 3 V, solar cells are not able to match this voltage, and as a consequence, the charging process does not occur unless a power electronic conversion stage is involved to step up the voltage. Three approaches have been explored previously, the usage of multi-junction solar cells [67, 86], the exploration of electrochemical cells with a lower voltage range of operation [71], and the interconnection of single junction solar cell in series to elevate the voltage [73, 74]. However, even if the voltage mismatch is handled, the relatively low power density of the combination of PV and electrochemical cells must be improved, as presented in Table 2.6 and Figure 2.5.

With the more recent attention dedicated to other electrochemical cells inside the family of Li-ion cells, new opportunities have arisen, and new concepts may be developed shortly. In particular, Li-air and Li-S stand out among the multiple options [98]; although, these are still technologies under development.

Additionally, in devices with shared electrodes and interfaces among the solar cell part and the electrochemical cell, it is a challenge to contain the Li ions in the electrochemical cell part, so they do not interfere with the normal functioning of the solar cell. In [66], TiN is proposed to prevent Li^+ diffusion to the PV part. This kind of device results in typically low-power devices along with low efficiencies.

2.3.6. Applications

Due to the advances in combining photovoltaic and energy storage technologies, some integrated devices have been dedicated to applications such as flexible power devices, microsystems, and aerospace applications. The most important features of relevant devices are introduced in this section.

Flexible devices

Advances in the mechanical properties of solar cells have propitiated its incursion in flexible electronics applications [100–102], while similar progress has been made to enable flexible storage devices [103–108]. As a consequence, combined solutions with flexible properties have been reported during the last years, especially in wearable applications [109, 110], due to their low weight, bendable, and form factor capabilities. Additionally, PI fibre-shape devices have shown potential to be woven in clothing manufacturing [90, 111, 112].

A wearable textile solar battery was developed in [99], and as a result, the mechanical properties of the battery were modified using textile electrodes. After the changes, the battery with a $Li_4Ti_5O_{12}$ anode and $LiFePO_4$ cathode performed similarly to a conventional metal foil based battery. Six solar cells in series were connected to the textile battery and supplied a LED load that consumed 4.2 mW (Figure 2.7a). A direct relationship between mechanical endurance and battery capacity was also observed. This because an increase in electrode thickness (directly related to battery capacity) negatively affected the mechanical stability, limiting the design.

Furthermore, semitransparent flexible polymer solar cells were integrated with small pouch batteries and white light LEDs to form a solar lamp [78]. This lamp was created

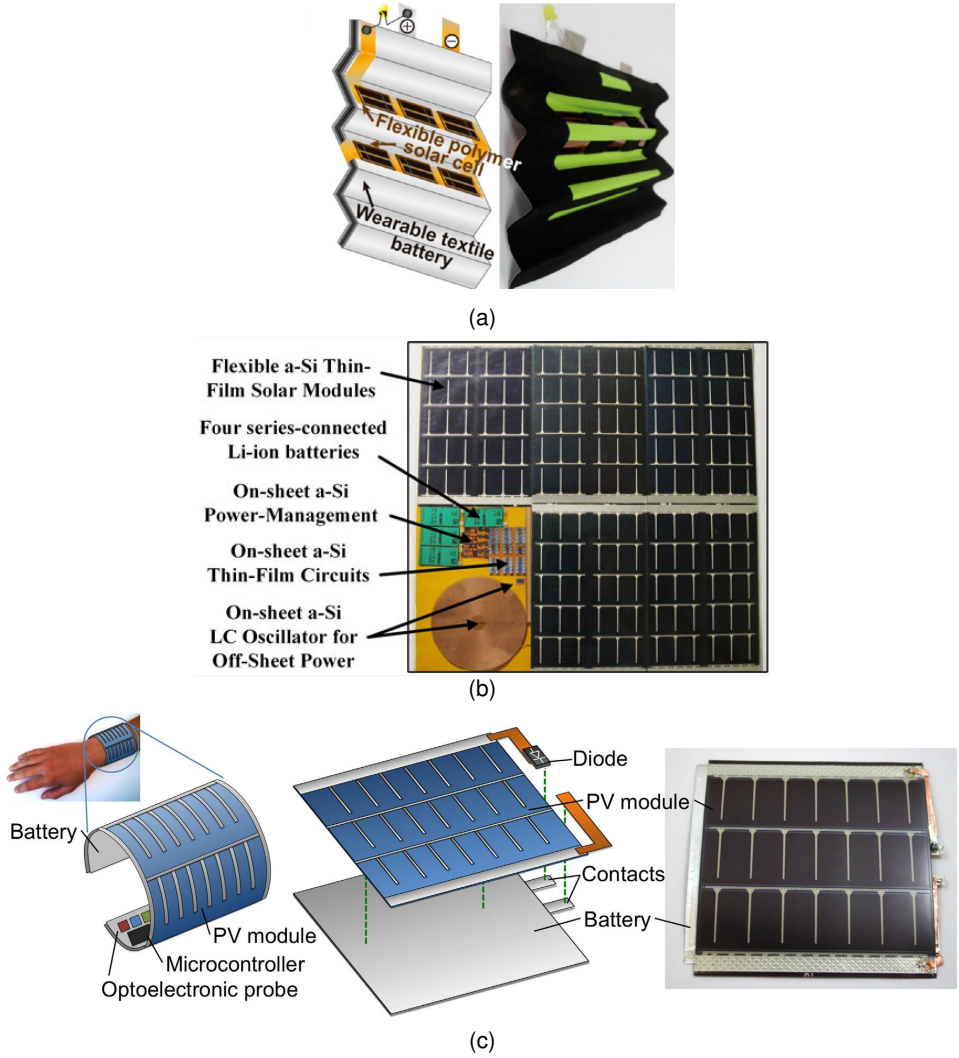

Figure 2.7: (a) Wearable textile solar battery. Reprinted with permission from [99]. Copyright 2013, American Chemical Society. (b) Power harvesting, management, storage, and delivery concept. Reproduced with permission [84]. Copyright 2014, IEEE. (c) Flexible energy harvesting and storage system comprising PV module and battery. Reproduced with permission [85]. Copyright 2016, Nature Publishing Group.

to provide light in places with limited access to electricity. The completed device consisted of a front cover and a back cover which give mechanical stability to the device. The battery, solar cell, connections, and components were attached using adhesive layers. This solar lamp was 12.5 × 8.8 × 2.4 cm^3, and weighted 50 g, proving to be a more sustainable solution compared to conventional lighting system when evaluating its environmental impact the rural communities studied [113]. In addition, another paper assessed the integration of battery and solar cells in a flexible substrate [76], making flexible Li-ion batteries a flexible electronics enabler [114].

Microsystems

With the development of self-sustainable solutions by combining storage and solar cells, it is possible to elaborate new devices that perform specific functions such as monitoring and sensing [115] [116]. To power an 8.75 mm autonomous microsystems for temperature sensing purposes, a thin film battery (12 μ Ah), two 1 mm^2 solar cells (5.48 %) and the power management (DC/DC converter) were built and stuck together as a compact solution [117]. In the same line, a dual-band wearable textile antenna for on-body medical applications composed of a flexible solar cell and energy storage was introduced in [118], where the maximum solar production could reach 53 mW.

As mentioned before, supercapacitors are used to stabilize solar cells output power for reduced periods as in [119], where an LCD clock was connected and powered uninterruptedly under intermittent light conditions. Moreover, the preliminary design of a Bluetooth Low Energy Beacon was introduced in [120], wherein a coin cell battery was integrated along with a solar cell to deliver power.

Furthermore, a flexible system that combined an amorphous silicon solar module, Li-ion thin-film batteries, and battery management was introduced in [84], and it is presented in Figure 2.7b. This device can supply load directly integrated into the device as well as external loads via wireless power transfer. It is important to mention that all the circuitry needed for the operation of the system was also integrated on the flexible sheet. The system was able to provide 5 mW to the internal loads (60% efficiency), while up to 8 mW via the wireless power system with an efficiency of 21%.

For a wearable health monitoring device, flexible energy storage and an amorphous Si solar cell were monolithically combined as Figure 2.7c shows. The printed battery, with a graphite anode and $LiCoO_2$ cathode, had a capacity of 47.5 mAh, and maximum solar power of around 230 mW [85]. This device was made for indoor lighting conditions and tested under electrical and mechanical stress cycles, showing good capacity retention. Here, the battery powered a pulse oximeter. Other wearable textile devices have been reported as a prominent application [40, 121, 122].

Off-grid electrification

Recent years have seen a meteoric rise in the use of integrated PV-battery devices for off-grid lighting applications [123], as lighting is seen as primary need falling in the first tier of household electricity access [124].

These products have a small, portable form factor with integrated PV and battery storage, and potentially some power electronics. These products are known as pico-solar products in the solar off-grid appliance market and are classified in the power

rating of up to 10 W_p [123]. These products usually include integrated PV-battery and LED lights, and sometimes also include USB-charging options for higher rated devices.

A prominent example is WakaWaka light, the most basic in the WakaWaka company's product portfolio. It has an integrated lithium polymer (Li-Po) battery of 500 mAh, LED lights up to 25 lumens, and monocrystalline silicon-based PV cell with 18% efficiency and surface area of 11 x 6 cm^2 [125]. A higher-end product from the same company, WakaWaka Power+, includes a 1 W_p monocrystalline-based PV cell with 22% efficiency, 3000 mAh of Li-Po battery, LED of up to 70 lumens, and additional USB outlet for charging of USB-power appliances with a max current of 2.1 A [126].

Another example is the company d.light design, which offers a variety of such pico-solar products as well. The product d.light S30, for instance, includes a monocrystalline silicon-based PV cell rated 0.33 W_p, a 450 mAh lithium iron phosphate battery with 2 LED lights capable of producing up to 60 lumens of light [127]. Another product called Radiance Lantern from the company Freeplay Energy offers a powerful 2 W_p PV panel integrated with 2600 mAh Li-ion battery, electronics for USB-based charging, and LED lighting (up to 200 lumens) with an additional integrated feature of an 85 dB safety siren [128].

Aerospace applications

In aerospace applications, the challenge for reducing launch mass and the assembly process is identified as the main benefits of the physical integration. A monolithic structure using a flexible PV layer, flexible solid-state battery, and a flexible power management unit has been proposed and tested for space applications [129]. Moreover, an integrated power supply has been assessed and found suitable as an autonomous power source for nanosatellites [75], where a monolithic package supply continuous power during space missions.

2.4. High power PV-storage devices

The prices of solar panels and batteries are decreasing faster than expected [130, 131], which is helping to minimize the cost of PV-storage solutions. However, further improvement can be made from the balance of system components point of view, but also from the soft cost side (i.e., installation cost and designing costs). More integrated and simple manufacturing process would aid in achieving this goal.

Apart from reducing systems costs, ancillary services such as energy balance, peak shaving, backup energy, and power stability for the distribution grid are also perceived as beneficial. Therefore, the possibility of PV-storage units is essential for low and medium voltage levels. As a consequence, integrated devices are able to produce power at higher values are fundamental in this context.

This section presents a comprehensive analysis of the published high power integrated solutions while analyzing the issues that must be solved as well as giving an indication of future trends and perspectives. A summary of the main features of these devices can be seen in Table 2.7. Also an indication of an ideal integrated device is introduced and graphically described in Figure 2.14.

2.4.1. Integration of power electronics

While some prototypes or existent products do not include all the components of the PV-storage system, previous efforts have been made either by integrating PV and power electronics converters [132–134], or by combining power electronics and energy storage in one device [135].

DC/DC optimizers and microinverters are already available in the solar market. The main advantages of these solutions are reductions on installation time and improvements in system efficiency in comparison to PV systems with central inverters. They are placed close to the solar panel [136, 137], implementing maximum power point tracking (MPPT). However, the connection between them and the panel is made during the installation process, which is not an entirely integrated solution.

A more integrated approach is achieved by combining the DC/DC converter with the PV module. In [138], a thin flexible converter is directly coupled with the PV panel in the same flexible substrate (Figure 2.8). Here, a boost converter 2 mm thick is designed to match the characteristics of a 124 W_p flexible solar panel, operating with a switching frequency between 0.1 MHz and 1 MHz and input voltage range of 25–45 V. The design procedure for such thin flexible converter is presented, highlighting the challenges when finding flexible and thin materials for the core. The efficiency was 84% for the rated power.

Another approach that consisted of controlling groups of individual solar cells of the PV module (235 W_p) has been studied [139]. To implement this device, several cells are connected to a DC/DC flyback converter which performs MPPT. They are also grouped and attached to an H-bridge inverter that produces a 120/240 VAC voltage. By extracting the maximum power from a group of PV cells, the maximum possible PV power for a particular module can be obtained. A solution like this is especially suitable for PV systems placed on curved surfaces, where gradients on irradiation might have a

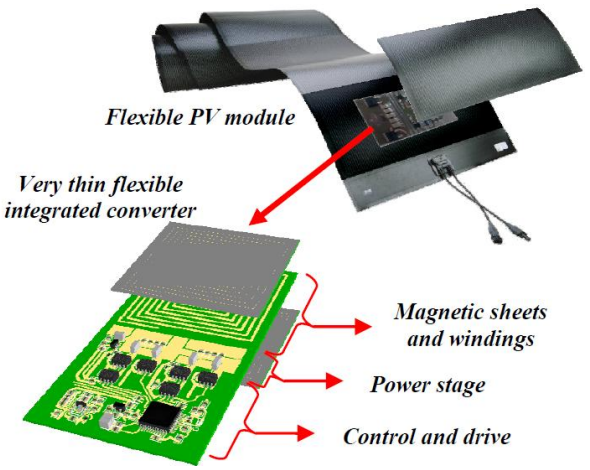

Figure 2.8: DC/DC converter integrated in a flexible PV module. Reproduced with permission [138]. Copyright 2012, IEEE.

considerable influence on performance.

2.4.2. PV and supercapacitor

A supercapacitor bank of 28 units was integrated with a PV panel and power electronics interface in [140], with the purpose of providing services such as power support to distribution networks to account for the intermittent and uncertain nature of PV generation. The output of the so-called smart PV module is DC (Figure 2.9a left), and when various modules are connected in parallel to the DC bus, the modules are coupled with a central inverter for AC applications. Two DC/DC conversion stages are also proposed (Figure 2.9a right), in order to boost the voltage of the PV panel (around 30 V) to the voltage of the DC bus (400 V). The complete system is shown in Figure 2.9b, there the supercapacitor bank is placed at the back of the PV panel as well as the power electronics interface unit. Because this solution is developed for micro-grids, the following modes of operation are defined: 1) PV and SCs provide the power available as

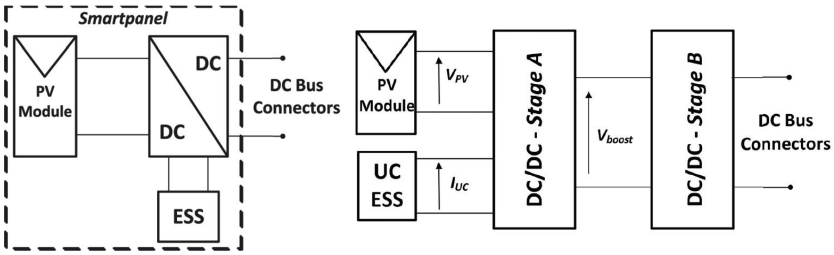

(a)

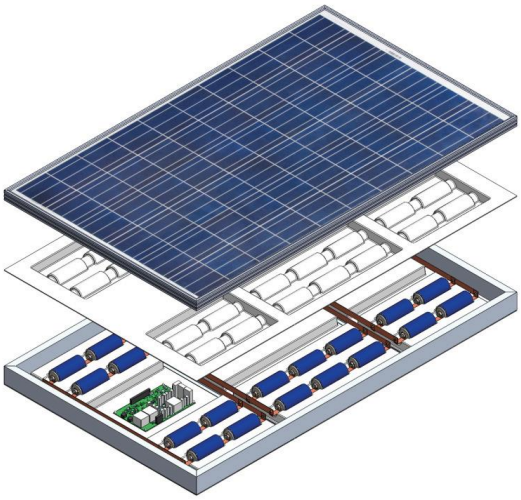

(b)

Figure 2.9: Characteristics of a high power PV-supercapacitor integrated device: (a) system components (left), power conversion stages (right), and (b) complete integrated system. Reproduced with permission [140]. Copyright 2016, IEEE.

requested by the micro-grid, 2) when PV power must lessen, the remaining power will be transferred to the SCs, and 3) the SCs are operated for a minimal impact on lifetime. The power electronics interface keeps the module operating in four states: charge, discharge, standby, and float. The decision of the state is based on the instantaneous voltage and its comparison to reference voltages. The testing of the buck-boost converter for the first conversion stage and the flyback converter for the second stage conversion was performed using a test bench. A maximum efficiency of 92.5% was reached for a PV power of around 160 W. The specifications of this solution are presented in Table 2.7, where it is also compared to other solutions.

2.4.3. PV and battery

First attempts of integration consisted of voluminous concepts, as presented in [141], with a significant structure combining a PV panel, active cooling system, lead-acid battery, and inverter as an all-in-one solution. However, improvements in battery technology and power electronics have made possible less space-consuming solutions.

A compact integration of a PV panel, battery pack, and an electronic control unit for relatively high power was suggested initially in [142]. This solution proposed multiple configurations: DC connection, AC connection, and grid-tied. According to the defined specifications, a solar module with a rated output power of 70 W_p is proposed, where the weight of the complete device should not exceed 15 kg and last for at least 15 years. The temperature range in which the PV panel, battery pack, and power electronics will operate are as follows: 85°C to -40°C, 60°C to -20°C, and 85°C to -40°C, respectively. The electronic control unit of the so-called *multifunctional module* has a converter that performs maximum power point tracking, a charge controller to take care of power flowing in and out of the battery pack, and a battery balancing system for monitoring and controlling individual cells of the pack.

As a continuation, a prototype of the MPPT circuit board and battery management system board were presented and individually tested in [143]. The battery management system (BMS) was designed to keep the cell operating safely and to reduce the impact on lifetime. The BMS limits the charging and discharging process by monitoring the voltage and comparing it to predefined thresholds, calculating the rate of discharging and charging, implementing specific charging or discharging method (i.e., constant current or constant voltage), and determining battery state of health (SOH). It also enables cell balancing to avoid over-charging or over-discharging of the weakest cell. To ensure the protection of the battery system, a set of alarm signals were defined, e.g., for a temperature higher than maximum, low SOH, maximum current reached, a voltage higher than maximum/minimum, and short-circuit protection.

The same concept was proposed as a building block to scale up the grid-connected system by connecting modules in parallel [144], as it is illustrated in Figure 2.10a. In such a system, all the integrated modules are connected to a central DC/DC converter, and this converter is linked to a single-phase inverter attached to the grid. A model to show the dynamic behaviour of two multifunctional modules in parallel was built, the parameter of the boost converter was also reported. To test the idea of integration, a prototype was tested (75 W_p PV panel coupled with a battery pack of 15 $LiFePO_4$ (48 V) cells with a capacity of 10 Ah (Figure 2.10b)). The efficiency of the converter used was

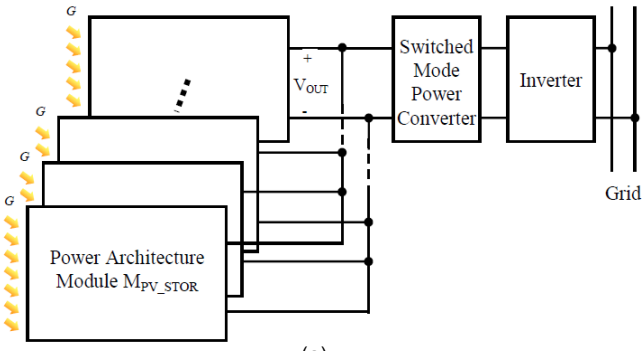

(a)

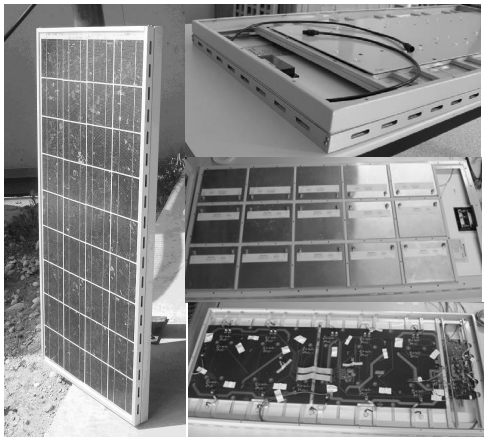

(b)

Figure 2.10: Features of the *Multifunctional module*(a) Distributed architecture and (b) prototype. Reproduced with permission [144]. Copyright 2010, IEEE.

90% when the system operates at rated power. Regarding the energy management system, battery charging is the priority. However, in some cases if the battery is above the minimum voltage and PV power is not enough to satisfy the load, the PV production will go directly to the load and the battery discharges. On the contrary, if the PV is at some time higher than the load, the power demanded is provided entirely by the PV, and the battery charge again. Experiments were carried out, and the performance was presented for two particular cases.

Another approach was introduced in [145]. This paper focuses on portable applications for places with no connection to the electricity grid (Figure 2.11). The proposed integrated solution uses a PV panel of 100 W_p, and a battery pack placed (13.2 V, 19.6 Ah) at the rear side of the PV module frame. The selection of commercial components that matched the specification of the PV and batteries are suggested; one element controls the charging while another the discharging process, for both devices the schematics are provided. Finally, the authors recommend the proposed solution for

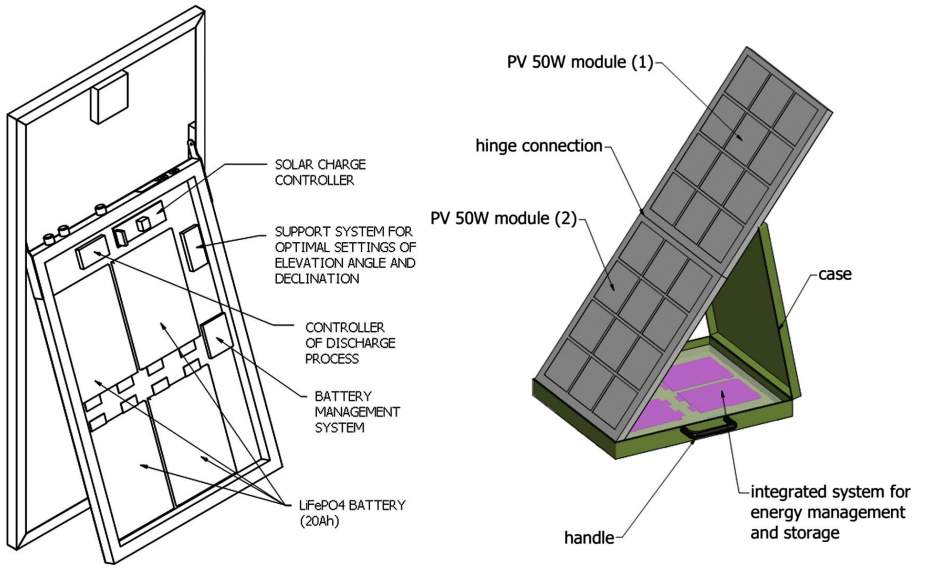

Figure 2.11: System for off-grid (left) and portable solutions (right). Reproduced with permission [145]. Copyright 2016, Elsevier.

camping, monitoring systems, and mobile systems.

Although previous papers studied the necessary design and implementation of the power electronics to ensure proper operation of the battery pack [143], the pronounced thermal stresses that the components of a fully integrated solution must handle is fundamental and deserve to be further explored [146, 147].

In [148], a thermal model that considers all heat generation sources was introduced in order to find an optimum placement of the components. This model was validated by testing a prototype (Figure 5.6b) in a solar simulator, where the temperature of the components was monitored during a 120 min test, and the Infrared (IR) photograph was taken for validation purposes as illustrated in Figure 5.6f. The thermal effect over the battery pack is the focus of this paper, as it is the most delicate component. By means of the model, it was determined that attaching the battery pack directly to the solar panel results in extreme temperature (Figure 5.3a). As a consequence, an air gap was found necessary, finding that the battery pack and other components must be placed at a distance of 5–7 cm from the solar panel to ensure a safe operation (Figure 5.3d). By including this air gap, even under severe conditions, the maximum battery temperature never surpassed 39°C. Moreover, an additional decrease of 5°C in the maximum battery temperature was achieved using a phase change material as a passive cooling method.

Moreover, the thermal effect of the solar panel was also analyzed in [149]. In this research, the batteries were mounted on the back side of a PV panel at 2 cm from it, as can be seen in Figure 2.12b. The PV temperature and battery temperature were measured using an IR camera, finding localized hotspots caused by the proximity of the battery to the PV panel which impede an efficient heat dissipation, as can be noticed in

the PV panel in the centre (Figure 2.12a). By analyzing the results from experiments, a thermal model was set, and its results were validated with the aim of being used to estimate the thermal behaviour of the module under various conditions. Consequently, it was found that in average the PV panel with batteries integrated is 10–15°C hotter than PV panel without batteries; as a consequence, the battery integrated PV panel is 6% less efficient for a defined scenario.

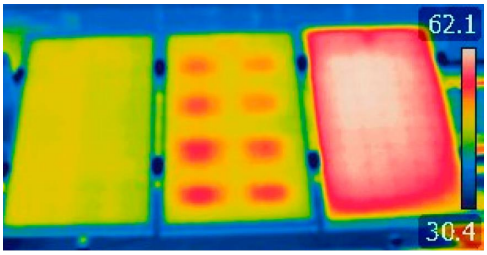

(a)

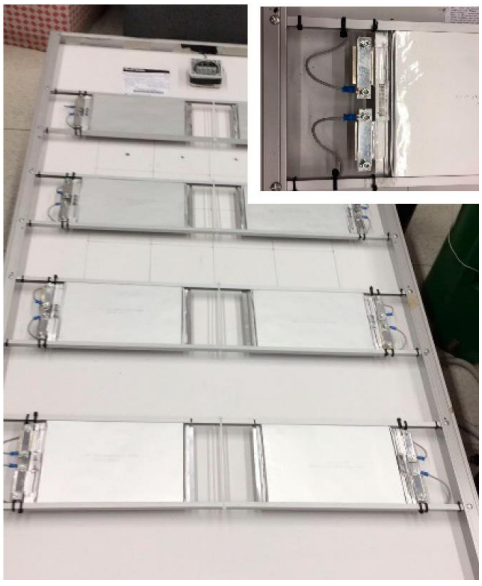

(b)

Figure 2.12: (a) Thermal image of the module with batteries attached and (b) placement of batteries. Reproduced with permission [149]. Copyright 2017, MDPI.

2.4.4. Integrated products

Among the PV products already in the market, the majority of them include batteries according to [15], lead acid and Li-ion being the most popular. However, just a few products have targeted applications with loads higher than 40 W_p in one single unit. One of them is for solar street lighting applications. The solar lamp is shown in Figure

Table 2.7: Features of PV panel and storage integrated devices for high power concepts.

Article	PV power (W_p)	ES capacity (Wh)	ES type	Capacity (Ah[a],F[b])
[140]	250	174	hybrid SC	4285[b]
[142][143][144]	75	480	$LiFePO_4$	10[a]
[145]	100	198	$LiFePO_4$	19.6[a]
[148]	265	965	$LiFePO_4$	20[a]
[141]	60	1260	Lead acid	105[a]
[150]	72	600	–	–
[149]	–	–	$LiFePO_4$	–

2.13a includes a solar module (60 W_p), a charge controller, Li-ion battery pack, and a LED array. This kind of lighting solutions have been implemented since several years ago, and it is expected to grow as the prices of PV modules, LED lighting systems, and batteries continue to reduce. Another solution is the product *Solpad* [150], which is designed to provide an AC output (115/230 V_{AC}) and plug-and-play solution for portable purposes.

2.4.5. Challenges and perspectives

For high power devices, some of the challenges found in low power concepts still hold; for instance, the importance of developing solid-state-electrolyte storage devices. However, new problems have come out such as thermal stability and its relation with battery, solar cells, and power electronics aging; the importance of system sizing, and modularity. While facing these problems, it is also relevant to pay attention to the economic considerations that could make these solutions economically feasible for the solar systems.

(a)

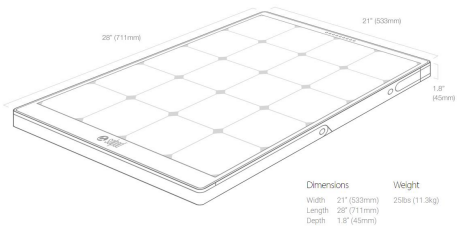

(b)

Figure 2.13: Two examples of integrated products. (a) Solar street lamp. Reproduced with permission [151]. Copyright 2016, John Wiley & Sons. (b) Solpad integrated module [150]. Reproduced with permission of Solpad.

Thermal effects of integration

As supported in [148], the battery pack operates at a higher temperature in integrated devices when compared to batteries operating inside buildings or households in non-integrated systems. Therefore, it is fundamental to study how these additional thermal stresses impact the dynamic functioning of the batteries. Moreover, the PV panel also operates at a more elevated temperature in integrated devices than when no components are attached at its rear side [148, 149, 152] with the unavoidable consequence of having a solar panel operating at lower efficiency. How much the temperature of the PV panel can be reduced and what is the optimum placement for all the components inside the casing are still open questions. Additionally, the effect of high temperature over the power electronics performance must be analyzed as suggested in [153].

Aging in integrated devices

As stated above, all components of the integrated device are subject to a higher temperature than usual, accelerating the aging mechanisms. In the case of batteries, because they are electrochemical cells, the instantaneous capacity of the battery increases following temperature rises, but in the long-term, it results in faster degradation rates across battery technologies [154]. This degradation is due to the increase in battery electrochemical activity, which accelerates the intercalation process in Li-ion batteries, but at the same time foster undesired side reactions which result in losses of active material (Li).

From the PV panel perspective, the rise in temperature of operation has detrimental consequences, lowering the lifespan although a precise indication of its magnitude must be clarified in the future. Future research should contemplate which failure mechanisms are promoted in Si solar cells as it is the most widely used solar cells technology. At the same time, the impact on power electronics aging must be addressed.

The widespread Li-ion batteries are composed of liquid electrolytes, which in cases of intensive operation can leak causing sudden failures that could lead to a potential explosion or malfunction. Consequently, with the recent advent of solid-electrolyte-batteries is convenient to start incorporating and testing its feasibility to cope with the aging and safety issues previously described.

Quest for the ideal system

Due to the more accelerated aging expected in integrated devices when compared to a conventional discrete PV-storage system, the components will fail faster; therefore, failing components must be replaced in an easy manner. To achieve this, the high power integrated devices have to be designed to account for these replacements while also maintaining a high level of integration. Accordingly, an ideal PV-storage system can be seen as a system that combines the benefits of actual low power integrated devices, which are characterized by its high level of integration, and state-of-the-art discrete PV-storage systems, where the components can be substituted easily. The ideal system is introduced in Figure 2.14 as the green box at the top right.

System sizing

For integrated devices, an optimum electrical system sizing is crucial considering both cost and space constraints. Batteries, for instance, are the most costly component, and

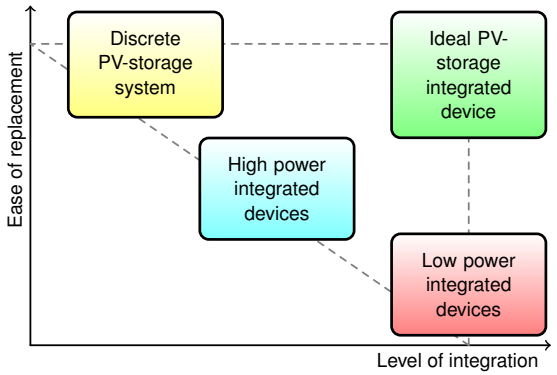

Figure 2.14: Comparison of existing approaches in terms of level of integration and ease of replacement; an ideal integrated device shown in green.

there is a consensus that battery capacity should be kept as low as possible. Nonetheless, the relationship between battery size and subsequent battery cycling must be considered, as the depth and velocity of charging/discharging is linked closely to its end of life.

The adequate combination of energy storage and solar generation is part of an appropriate sizing methodology. The battery capacity and PV panel rating depends on the application and relates to the criteria that control the power flow of the system. The approach that the controller of the system follows is called an energy management system, and it is another aspect to consider during the sizing as it determines the cycling, depth of discharge, and C-rates. Additionally, the power electronics takes care of controlling the power flow inside the integrated device, and its size (power rating) and architecture must be established considering the EMS system.

Importance of modularity

When the energy need augments, having a system that can be scaled up without a total reconstruction of the system is ideal [146]. In these lines, a modular solution provides flexibility, acting as a building block when energy demand changes [144]. Hence, it is essential to incorporate the possibility of developing modular solutions in the design via power electronic enabler platform. Later on, if a modular solution is developed, next steps towards how to optimized the modular growing of the system could become a promising research area.

Economic analysis

As the integrated solutions intend to become an alternative to conventional PV-storage systems, aspects such as cost and possible benefits derived from the use of integrated devices, deserve to be put under scrutiny. For instance, new studies are required to quantify the tentative reduction on cost due to more simple and easy manufacturing processes for integrated devices, when compared to conventional systems. A similar

analysis is needed for high power integrated devices, where possible reduction on installation cost is foreseen in comparison to standard PV-storage systems. It is also essential to study how integrated products might be perceived by potential clients to evaluate its need and acceptance in the solar market.

2.5. Conclusion

This chapter summarizes the efforts when combining PV panels, power electronics, and energy storage components in one device. The gaps to fill and challenges to tackle are introduced and analyzed. For the low power integrated concepts, it is essential to incorporate the benefits obtained by means of power electronics to achieve higher efficiencies and ensure safe operation of components. Moreover, while novel ideas of integration are promising, long-term testing including cycling analysis is fundamental when validating the feasibility of the approaches.

In the case of high power devices, the thermal stresses induced by outdoor conditions are fundamental; therefore, this will be studied in chapter 5; also, the thermal stresses and its relation to aging will be investigated in more detail in chapter 6. Additionally, the electrical system sizing is vital as integrated concepts experience space, and application-related constraints. This will be covered in chapter 3.

Finally, this chapter describes the progress on the integration on solar energy and energy storage devices as an effort to identify the challenges and further research to be done in order achieve more stable power integrated devices for PV systems, to move from the laboratory or proof of concept to practical applications.

References

[1] V. Vega-Garita, L. Ramirez-Elizondo, N. Narayan, and P. Bauer, *Integrating a photovoltaic storage system in one device: A critical review,* Progress in Photovoltaics: Research and Applications **27**, 346 (2019), https://onlinelibrary.wiley.com/doi/pdf/10.1002/pip.3093 .

[2] Y. Zhong, X. Xia, W. Mai, J. Tu, and H. J. Fan, *Integration of Energy Harvesting and Electrochemical Storage Devices,* Advanced Materials Technologies **2**, 1 (2017).

[3] A. E. Ostfeld and A. C. Arias, *Flexible photovoltaic power systems: integration opportunities, challenges and advances,* Flexible and Printed Electronics **2**, 013001 (2017).

[4] L. Li, Z. Wu, S. Yuan, and X.-B. B. Zhang, *Advances and challenges for flexible energy storage and conversion devices and systems,* Energy & Environmental Science **7**, 2101 (2014).

[5] Y. Sun and X. Yan, *Recent Advances in Dual-Functional Devices Integrating Solar Cells and Supercapacitors,* Solar RRL **1**, 1700002 (2017).

[6] J. Xu, X. Wang, X. Wang, D. Chen, X. Chen, D. Li, and G. Shen, *Three-Dimensional Structural Engineering for Energy-Storage Devices: From Microscope to Macroscope,* ChemElectroChem **1**, 975 (2014).

[7] H. Wei, D. Cui, J. Ma, L. Chu, X. Zhao, H. Song, H. Liu, T. Liu, N. Wang, and Z. Guo, *Energy conversion technologies towards self-powered electrochemical energy storage systems: the state of the art and perspectives,* J. Mater. Chem. A **5**, 1873 (2017).

[8] X. Cai, C. Zhang, S. Zhang, Y. Fang, and D. Zou, *Application of carbon fibers to flexible, miniaturized wire/fiber-shaped energy conversion and storage devices,* J. Mater. Chem. A **5**, 2444 (2017).

[9] X. Pu, W. Hu, and Z. L. Wang, *Toward Wearable Self-Charging Power Systems: The Integration of Energy-Harvesting and Storage Devices,* Small **1702817**, 1 (2017).

[10] S. Pan, Z. Zhang, W. Weng, H. Lin, Z. Yang, and H. Peng, *Miniature wire-shaped solar cells, electrochemical capacitors and lithium-ion batteries,* Materials Today **17**, 276 (2014).

[11] C. H. Ng, H. N. Lim, S. Hayase, I. Harrison, A. Pandikumar, and N. M. Huang, *Potential active materials for photo-supercapacitor: A review,* Journal of Power Sources **296**, 169 (2015).

[12] R. Liu, Y. Liu, H. Zou, T. Song, and B. Sun, *Integrated solar capacitors for energy conversion and storage,* Nano Research **10**, 1545 (2017).

[13] B. Luo, D. Ye, and L. Wang, *Recent Progress on Integrated Energy Conversion and Storage Systems,* Advanced Science **4**, 1 (2017).

[14] J.-H. Lee, J. Kim, T. Y. Kim, M. S. Al Hossain, S.-W. Kim, and J. H. Kim, *All-in-one energy harvesting and storage devices,* J. Mater. Chem. A **4**, 7983 (2016), arXiv:1612.08814 .

[15] G. Apostolou and A. H. M. E. Reinders, *Overview of Design Issues in Product-Integrated Photovoltaics,* Energy Technology **2**, 229 (2014).

[16] V. Vega-Garita, L. Ramirez-Elizondo, G. R. C. Mouli, and P. Bauer, *Review of residential PV-storage architectures,* 2016 IEEE International Energy Conference, ENERGYCON 2016 (2016), 10.1109/ENERGYCON.2016.7514039.

[17] Z. Ouyang, S. N. Lou, D. Lau, J. Chen, S. Lim, P.-C. Hsiao, D.-W. Wang, R. Amal, Y. H. Ng, and A. Lennon, *Monolithic Integration of Anodic Molybdenum Oxide Pseudocapacitive Electrodes on Screen-Printed Silicon Solar Cells for Hybrid Energy Harvesting-Storage Systems,* Advanced Energy Materials , 1602325 (2016).

[18] T. Miyasaka and T. N. Murakami, *The photocapacitor: An efficient self-charging capacitor for direct storage of solar energy,* Applied Physics Letters **85**, 3932 (2004).

[19] T. N. Murakami, N. Kawashima, and T. Miyasaka, *A high-voltage dye-sensitized photocapacitor of a three-electrode system,* Chemical Communications , 3346 (2005).

[20] Y.-W. Su, S.-C. Lan, and K.-H. Wei, *Organic photovoltaics,* Materials Today **15**, 554 (2012).

[21] B. P. Lechêne, M. Cowell, A. Pierre, J. W. Evans, P. K. Wright, and A. C. Arias, *Organic solar cells and fully printed super-capacitors optimized for indoor light energy harvesting,* Nano Energy **26**, 631 (2016).

[22] F. C. Krebs, N. Espinosa, M. Hösel, R. R. Søndergaard, and M. Jørgensen, *25th anniversary article: Rise to power - OPV-based solar parks,* (2014).

[23] C. T. Chien, P. Hiralal, D. Y. Wang, I. S. Huang, C. C. Chen, C. W. Chen, and G. A. Amaratunga, *Graphene-Based Integrated Photovoltaic Energy Harvesting/Storage Device,* Small **11**, 2929 (2015).

[24] J. Kim, S. M. Lee, Y.-H. Hwang, S. Lee, B. Park, J.-H. Jang, and K. Lee, *A highly efficient self-power pack system integrating supercapacitors and photovoltaics with an area-saving monolithic architecture,* J. Mater. Chem. A **5**, 1906 (2017).

[25] F. Zhou, Z. Ren, Y. Zhao, X. Shen, A. Wang, Y. Y. Li, C. Surya, and Y. Chai, *Perovskite Photovoltachromic Supercapacitor with All-Transparent Electrodes,* ACS Nano **10**, 5900 (2016).

[26] A. S. Westover, K. Share, R. Carter, A. P. Cohn, L. Oakes, and C. L. Pint, *Direct integration of a supercapacitor into the backside of a silicon photovoltaic device,* Applied Physics Letters **104**, 1 (2014).

[27] Z. Gao, C. Bumgardner, N. Song, Y. Zhang, J. Li, and X. Li, *Cotton-textile-enabled flexible self-sustaining power packs via roll-to-roll fabrication,* Nature Communications **7**, 11586 (2016).

[28] Z. Yang, L. Li, Y. Luo, R. He, L. Qiu, H. Lin, and H. Peng, *An integrated device for both photoelectric conversion and energy storage based on free-standing and aligned carbon nanotube film,* J. Mater. Chem. A **1**, 954 (2013).

[29] J. Liang, G. Zhu, C. Wang, Y. Wang, H. Zhu, Y. Hu, H. Lv, R. Chen, L. Ma, T. Chen, Z. Jin, and J. Liu, *MoS2-Based All-Purpose Fibrous Electrode and Self-Powering Energy Fiber for Efficient Energy Harvesting and Storage,* Advanced Energy Materials (2016), 10.1002/aenm.201601208.

[30] N. Bagheri, A. Aghaei, M. Y. Ghotbi, E. Marzbanrad, N. Vlachopoulos, L. Häggman, M. Wang, G. Boschloo, A. Hagfeldt, M. Skunik-Nuckowska, and P. J. Kulesza, *Combination of asymmetric supercapacitor utilizing activated carbon and nickel oxide with cobalt polypyridyl-based dye-sensitized solar cell,* Electrochimica Acta **143**, 390 (2014).

[31] D. Schmidt, M. D. Hager, and U. S. Schubert, *Photo-Rechargeable Electric Energy Storage Systems,* Advanced Energy Materials **6**, 1 (2016).

[32] M. Skunik, P. J. Kulesza, N. Vlachopoulos, L. Haggman, A. Hagfeldt, E. C. S. Transactions, T. E. Society, M. Skunik, P. J. Kulesza, N. Vlachopoulos, L. Haggman, and A. Hagfeldt, *Development of Hybrid Organic-Inorganic Materials for Efficient Charging/Discharging in Electrochemical and Photoelectrochemical Capacitors,* ECS Transactions **35**, 93 (2011).

[33] T. Chen, L. Qiu, Z. Yang, Z. Cai, J. Ren, H. Li, H. Lin, X. Sun, and H. Peng, *An integrated "energy wire" for both photoelectric conversion and energy storage,* Angewandte Chemie - International Edition **51**, 11977 (2012).

[34] P. A. Mini, S. V. Nair, and K. R. V. Subramanian, *Design and development of an integrated device consisting of an independent solar cell with electrical,* Progress in Photovoltaics: Research and Applications , 1153 (2013).

[35] P. J. Kuleszaa, M. Skunik-Nuckowskaa, K. Grzejszczyka, N. Vlachopoulosb, L. Yangb, L. Haggmanb, and A. Hagfeldtb, *Development of Solid-State Photo-Supercapacitor by Coupling Dye-Sensitized Solar Cell Utilizing Conducting Polymer Charge Relay with Proton-Conducting Membrane Based Electrochemical Capacitor,* **50**, 235 (2013).

[36] H. Li, Q. Zhao, W. Wang, H. Dong, D. Xu, G. Zou, H. Duan, and D. Yu, *Novel planar-structure electrochemical devices for highly flexible semitransparent power generation/storage sources,* Nano Letters **13**, 1271 (2013).

[37] M. Skunik-Nuckowska, K. Grzejszczyk, P. J. Kulesza, L. Yang, N. Vlachopoulos, L. Häggman, E. Johansson, and A. Hagfeldt, *Integration of solid-state dye-sensitized solar cell with metal oxide charge storage material into photoelectrochemical capacitor,* Journal of Power Sources **234**, 91 (2013).

[38] X. Zhang, X. Huang, C. Li, and H. Jiang, *Dye-sensitized solar cell with energy storage function through PVDF/ZnO nanocomposite counter electrode,* Advanced Materials **25**, 4093 (2013).

[39] Z. Zhang, X. Chen, P. Chen, G. Guan, L. Qiu, H. Lin, Z. Yang, W. Bai, Y. Luo, and H. Peng, *Integrated polymer solar cell and electrochemical supercapacitor in a flexible and stable fiber format,* Advanced Materials **26**, 466 (2014).

[40] X. Chen, H. Sun, Z. Yang, G. Guan, Z. Zhang, L. Qiu, and H. Peng, *A novel energy fiber by coaxially integrating dye-sensitized solar cell and electrochemical capacitor,* Journal of Materials Chemistry A **2**, 1897 (2014).

[41] X. Huang, X. Zhang, and H. Jiang, *Energy storage via polyvinylidene fluoride dielectric on the counterelectrode of dye-sensitized solar cells,* Journal of Power Sources **248**, 434 (2014).

[42] Z. Yang, J. Deng, H. Sun, J. Ren, S. Pan, and H. Peng, *Self-powered energy fiber: Energy conversion in the sheath and storage in the core,* Advanced Materials **26**, 7038 (2014).

[43] X. Xu, S. Li, H. Zhang, Y. Shen, S. M. Zakeeruddin, M. Graetzel, Y. B. Cheng, and M. Wang, *A power pack based on organometallic perovskite solar cell and supercapacitor,* ACS Nano **9**, 1782 (2015).

[44] R. Narayanan, P. N. Kumar, M. Deepa, and A. K. Srivastava, *Combining Energy Conversion and Storage: A Solar Powered Supercapacitor,* Electrochimica Acta **178**, 113 (2015).

[45] C. Shi, H. Dong, R. Zhu, H. Li, Y. Sun, D. Xu, Q. Zhao, and D. Yu, *An "all-in-one" mesh-typed integrated energy unit for both photoelectric conversion and energy storage in uniform electrochemical system,* Nano Energy **13**, 670 (2015).

[46] X. Zhang and H. Jiang, *Scattering-layer-induced energy storage function in polymer-based quasi-solid-state dye-sensitized solar cells,* Applied Physics Letters **106** (2015), 10.1063/1.4914585.

[47] A. P. Cohn, W. R. Erwin, K. Share, L. Oakes, A. S. Westover, R. E. Carter, R. Bardhan, and C. L. Pint, *All Silicon Electrode Photocapacitor for Integrated Energy Storage and Conversion,* Nano Letters **15**, 2727 (2015).

[48] S. Selvam, B. Balamuralitharan, S. N. Karthick, A. D. Savariraj, K. V. Hemalatha, S.-K. Kim, and H.-J. Kim, *Novel high-temperature supercapacitor combined dye sensitized solar cell from a sulfated β-cyclodextrin/PVP/MnCO ₃ composite,* J. Mater. Chem. A **3**, 10225 (2015).

[49] B. N. Reddy, R. Mukkabla, M. Deepa, and P. Ghosal, *Dual purpose poly(3,4-ethylenedioxypyrrole)/vanadium pentoxide nanobelt hybrids in photo-electrochromic cells and supercapacitors,* RSC Adv. **5**, 31422 (2015).

[50] H. Sun, Y. Jiang, L. Qiu, X. You, J. Yang, X. Fu, P. Chen, G. Guan, Z. Yang, X. Sun, and H. Peng, *Energy harvesting and storage devices fused into various patterns,* J. Mater. Chem. A **3**, 14977 (2015).

[51] C. Li, M. M. Islam, J. Moore, J. Sleppy, C. Morrison, K. Konstantinov, S. X. Dou, C. Renduchintala, and J. Thomas, *Wearable energy-smart ribbons for synchronous energy harvest and storage,* Nature Communications **7**, 13319 (2016).

[52] F.-W. Lee, C.-W. Ma, Y.-H. Lin, P.-C. Huang, Y.-L. Su, and Y.-J. Yang, *A Micromachined Photo-Supercapacitor Integrated with CdS-Sensitized Solar Cells and Buckypaper,* Sensors and materials **28**, 749 (2016).

[53] J. Xu, Z. Ku, Y. Zhang, D. Chao, and H. J. Fan, *Integrated Photo-Supercapacitor Based on PEDOT Modified Printable Perovskite Solar Cell,* Advanced Materials Technologies , 1 (2016).

[54] X. Huang, X. Zhang, and H. Jiang, *Photovoltaically self-charging cells with WO_3H_2O/CNTs/PVDF composite,* RSC Adv. **6**, 96490 (2016).

[55] Z. Wen, M.-H. Yeh, H. Guo, J. Wang, Y. Zi, W. Xu, J. Deng, L. Zhu, X. Wang, C. Hu, L. Zhu, X. Sun, and Z. L. Wang, *Self-powered textile for wearable electronics by hybridizing fiber-shaped nanogenerators, solar cells, and supercapacitors,* Science Advances **2**, e1600097 (2016).

[56] Z. Chai, N. Zhang, P. Sun, Y. Huang, C. Zhao, H. J. Fan, X. Fan, and W. Mai, *Tailorable and Wearable Textile Devices for Solar Energy Harvesting and Simultaneous Storage,* ACS Nano **10**, 9201 (2016).

[57] A. Scalia, F. Bella, A. Lamberti, S. Bianco, C. Gerbaldi, E. Tresso, and C. F. Pirri, *A flexible and portable powerpack by solid-state supercapacitor and dye-sensitized solar cell integration,* Journal of Power Sources **359**, 311 (2017).

[58] F. Zhang, W. Li, Z. Xu, M. Ye, W. Guo, H. Xu, and X. Liu, *Transparent conducting oxide- and Pt-free flexible photo-rechargeable electric energy storage systems,* RSC Advances **7**, 52988 (2017).

[59] R. Liu, C. Liu, and S. Fan, *A photocapacitor based on organometal halide perovskite and PANI/CNT composites integrated using a CNT bridge,* J. Mater. Chem. A **5**, 23078 (2017).

[60] Q. Wang, H. Chen, E. McFarland, and L. Wang, *Solar Rechargeable Batteries Based on Lead-Organohalide Electrolyte,* Advanced Energy Materials **5**, 1 (2015).

[61] A. Hauch, A. Georg, U. O. Krasovec, B. Orel, U. Opara Krašovec, and B. Orel, *Photovoltaically Self-Charging Battery,* Journal of The Electrochemical Society **149**, A1208 (2002).

[62] M. Yu, W. D. McCulloch, Z. Huang, B. B. Trang, J. Lu, K. Amine, and Y. Wu, *Solar-powered electrochemical energy storage: an alternative to solar fuels,* J. Mater. Chem. A **4**, 2766 (2016).

[63] S. Licht, G. Hodes, R. Tenne, and J. Manassen, *A light-variation insensitive high efficiency solar cell, Nature*, **326**, 863 (1987).

[64] A. Paolella, C. Faure, G. Bertoni, S. Marras, A. Guerfi, A. Darwiche, P. Hovington, B. Commarieu, Z. Wang, M. Prato, M. Colombo, S. Monaco, W. Zhu, Z. Feng, A. Vijh, C. George, G. P. Demopoulos, M. Armand, and K. Zaghib, *Light-assisted delithiation of lithium iron phosphate nanocrystals towards photo-rechargeable lithium ion batteries,* Nature Communications **8**, 1 (2017).

[65] M. Yu, X. Ren, L. Ma, and Y. Wu, *Integrating a redox-coupled dye-sensitized photoelectrode into a lithium–oxygen battery for photoassisted charging,* Nature communications **5**, 5111 (2014).

[66] V. Chakrapani, F. Rusli, M. A. Filler, and P. A. Kohl, *A combined photovoltaic and Li ion battery device for continuous energy harvesting and storage,* Journal of Power Sources **216**, 84 (2012).

[67] S. N. Agbo, T. Merdzhanova, S. Yu, H. Tempel, H. Kungl, R. A. Eichel, U. Rau, and O. Astakhov, *Photoelectrochemical application of thin-film silicon triple-junction solar cell in batteries,* Physica Status Solidi (A) Applications and Materials Science **213**, 1926 (2016).

[68] P. Rand, Bermejo*, J. Genoe, P. Heremans, and J. Poortmans, *Light harvesting photovoltaic mini-generator,* Prog. Photovolt: Res. Appl. **15**, 967 (2011), arXiv:1303.4604 .

[69] R. B. Ye, K. Yoshida, K. Ohta, and M. Baba, *Integrated thin-film rechargeable battery on α-Si thin-film solar cell,* Advanced Materials Research **788**, 685 (2013).

[70] W. Guo, X. Xue, S. Wang, C. Lin, and Z. L. Wang, *An integrated power pack of dye-sensitized solar cell and Li battery based on double-sided TiO2 nanotube arrays,* Nano Letters **12**, 2520 (2012).

[71] T. Meister, K. Ishida, R. Shabanpour, B. K. Boroujeni, C. Carta, F. Ellinger, N. Munzenrieder, L. Petti, G. A. Salvatore, G. Troster, M. Wagner, P. Ghesquiere, S. Kiefl, and M. Krebs, *Bendable energy-harvesting module with organic photovoltaic, rechargeable battery, and a-IGZO TFT charging electronics,* 2015 European Conference on Circuit Theory and Design, ECCTD 2015 , 7 (2015).

[72] G. Dennler, S. Bereznev, D. Fichou, K. Holl, D. Ilic, R. Koeppe, M. Krebs, A. Labouret, C. Lungenschmied, A. Marchenko, D. Meissner, E. Mellikov, J. Méot,

A. Meyer, T. Meyer, H. Neugebauer, A. Öpik, N. S. Sariciftci, S. Taillemite, and T. Wöhrle, *A self-rechargeable and flexible polymer solar battery,* Solar Energy **81**, 947 (2007).

[73] handon Um, K.-H. Choi, I. Hwang, S.-H. Kim, K. Seo, and S.-Y. Lee, *Monolithically integrated, photo-rechargeable portable power sources based on miniaturized Si solar cells and printed solid-state lithium-ion batteries,* Energy Environ. Sci. **10**, 931 (2017).

[74] J. Xu, Y. Chen, and L. Dai, *Efficiently photo-charging lithium-ion battery by perovskite solar cell,* Nat Commun **6**, 1 (2015), arXiv:arXiv:1011.1669v3 .

[75] R. P. Raffaelle, A. F. Hepp, G. A. Landis, and D. J. Hoffman, *Mission applicability assessment of integrated power components and systems,* Progress in Photovoltaics: Research and Applications **10**, 391 (2002).

[76] H. S. Kim, J. S. Kang, J. S. Park, H. T. Hahn, H. C. Jung, and J. W. Joung, *Inkjet printed electronics for multifunctional composite structure,* Composites Science and Technology **69**, 1256 (2009).

[77] F. C. Krebs, J. Fyenbo, and M. Jørgensen, *Product integration of compact roll-to-roll processed polymer solar cell modules: methods and manufacture using flexographic printing, slot-die coating and rotary screen printing,* Journal of Materials Chemistry **20**, 8994 (2010).

[78] F. C. Krebs, T. D. Nielsen, J. Fyenbo, M. Wadstrom, and M. S. Pedersen, *Manufacture, integration and demonstration of polymer solar cells in a lamp for the "Lighting Africa" initiative,* Energy & Environmental Science **3**, 512 (2010).

[79] F. C. Krebs, J. Fyenbo, D. M. Tanenbaum, S. a. Gevorgyan, R. Andriessen, B. van Remoortere, Y. Galagan, and M. Jørgensen, *The OE-A OPV demonstrator anno domini 2011,* Energy & Environmental Science **4**, 4116 (2011).

[80] V. Chakrapani, F. Rusli, M. A. Filler, and P. A. Kohl, *A combined photovoltaic and Li ion battery device for continuous energy harvesting and storage,* Journal of Power Sources **216**, 84 (2012).

[81] P. Liu, H. X. Yang, X. P. Ai, G. R. Li, and X. P. Gao, *A solar rechargeable battery based on polymeric charge storage electrodes,* Electrochemistry Communications **16**, 69 (2012).

[82] Y. H. Lee, J. S. Kim, J. Noh, I. Lee, H. J. Kim, S. Choi, J. Seo, S. Jeon, T. S. Kim, J. Y. Lee, and J. W. Choi, *Wearable textile battery rechargeable by solar energy,* Nano Letters **13**, 5753 (2013).

[83] J. Kim, C. Kim, M. Fojtik, D. Kim, G. Chen, Y.-S. Lin, D. Fick, J. Park, M. Seok, M.-T. Chen, Z. Foo, D. Blaauw, and D. Sylvester, *A Millimeter-Scale Energy-Autonomous Sensor System With Stacked Battery and Solar Cells,* IEEE Journal of Solid-State Circuits **48**, 801 (2013).

[84] W. Rieutort-Louis, L. Huang, Y. Hu, J. Sanz-Robinson, S. Wagner, J. C. Sturm, and N. Verma, *A complete fully thin-film pv harvesting and power-management system on plastic with on-sheet battery management and wireless power delivery to off-sheet loads,* IEEE Journal of Photovoltaics **4**, 432 (2014).

[85] A. E. Ostfeld, A. M. Gaikwad, Y. Khan, and A. C. Arias, *High-performance flexible energy storage and harvesting system for wearable electronics,* Scientific Reports **6**, 26122 (2016).

[86] S. N. Agbo, T. Merdzhanova, S. Yu, H. Tempel, H. Kungl, R. A. Eichel, U. Rau, and O. Astakhov, *Development towards cell-to-cell monolithic integration of a thin-film solar cell and lithium-ion accumulator,* Journal of Power Sources **327**, 340 (2016).

[87] H. Sun, Y. Jiang, S. Xie, Y. Zhang, J. Ren, A. Ali, S.-G. Doo, I. H. Son, X. Huang, and H. Peng, *Integrating photovoltaic conversion and lithium ion storage into a flexible fiber,* Journal of Materials Chemistry A **4**, 7601 (2016).

[88] F. Sandbaumhüter, S. N. Agbo, C. L. Tsai, O. Astakhov, S. Uhlenbruck, U. Rau, and T. Merdzhanova, *Compatibility study towards monolithic self-charging power unit based on all-solid thin-film solar module and battery,* Journal of Power Sources **365**, 303 (2017).

[89] S. Pan, J. Ren, X. Fang, and H. Peng, *Integration: An Effective Strategy to Develop Multifunctional Energy Storage Devices,* Advanced Energy Materials **6**, 1 (2016).

[90] T. Song and B. Sun, *Towards photo-rechargeable textiles integrating power conversion and energy storage functions: Can we kill two birds with one stone?* ChemSusChem **6**, 408 (2013).

[91] T. Chen, Z. Yang, and H. Peng, *Integrated devices to realize energy conversion and storage simultaneously,* ChemPhysChem **14**, 1777 (2013).

[92] X. Lu, M. Yu, G. Wang, Y. Tong, and Y. Li, *Flexible solid-state supercapacitors: design, fabrication and applications,* Energy & Environmental Science **7**, 2160 (2014).

[93] M. A. Green, Y. Hishikawa, E. D. Dunlop, D. H. Levi, J. Hohl-Ebinger, and A. W. Ho-Baillie, *Solar cell efficiency tables (version 52),* Progress in Photovoltaics: Research and Applications **26**, 427 (2018), arXiv:1303.4604 .

[94] A. Richter, M. Hermle, and S. W. Glunz, *Crystalline Silicon Solar Cells Reassessment of the Limiting Efficiency for Crystalline Silicon Solar Cells,* IEEE Journal of Photovoltaics **3**, 1184 (2013).

[95] A. Thielmann, A. Sauer, R. Isenmann, and M. Wietschel, *Fraunhofer Institute for Systems and Innovation Research ISI*, Tech. Rep. 1 (2013).

[96] Everlight, *Technical data sheet,* 5 mm Round White LED (T-1 3/4) (2007).

[97] O. Isabella, A. Smets, K. Jäger, M. Zeman, and R. van Swaaij, *Solar energy: The physics and engineering of photovoltaic conversion, technologies and systems,* UIT Cambridge Limited (2016).

[98] A. Vlad, N. Singh, C. Galande, and P. M. Ajayan, *Design Considerations for Unconventional Electrochemical Energy Storage Architectures,* Advanced Energy Materials **5**, 1 (2015).

[99] J. Seo, S. Jeon, T.-s. Kim, J.-y. Lee, and J. W. Choi, *Wearable Textile Battery Rechargeable by Solar Energy,* Nano letters (2013).

[100] J. S. Kim, D. Ko, D. J. Yoo, D. S. Jung, C. T. Yavuz, N. I. Kim, I. S. Choi, J. Y. Song, and J. W. Choi, *A Half Millimeter Thick Coplanar Flexible Battery with Wireless Recharging Capability,* Nano Letters **15**, 2350 (2015).

[101] F. Di Giacomo, A. Fakharuddin, R. Jose, and T. M. Brown, *Progress, challenges and perspectives in flexible perovskite solar cells,* Energy Environ. Sci. **9**, 3007 (2016).

[102] G. Li, R. Zhu, and Y. Yang, *Polymer solar cells,* Nature Photonics **6**, 153 (2012).

[103] K. Xie and B. Wei, *Materials and structures for stretchable energy storage and conversion devices,* Advanced Materials **26**, 3592 (2014).

[104] G. Zhou, F. Li, and H.-M. Cheng, *Progress in flexible lithium batteries and future prospects,* Energy Environ. Sci. **7**, 1307 (2014).

[105] S.-Y. Lee, K.-H. Choi, W.-S. Choi, Y. H. Kwon, H.-R. Jung, H.-C. Shin, and J. Y. Kim, *Progress in flexible energy storage and conversion systems, with a focus on cable-type lithium-ion batteries,* Energy & Environmental Science **6**, 2414 (2013).

[106] Z. Song, X. Wang, C. Lv, Y. An, M. Liang, T. Ma, D. He, Y.-J. Zheng, S.-Q. Huang, H. Yu, and H. Jiang, *Kirigami-based stretchable lithium-ion batteries,* Scientific Reports **5**, 10988 (2015).

[107] Z. Song, T. Ma, R. Tang, Q. Cheng, X. Wang, D. Krishnaraju, R. Panat, C. K. Chan, H. Yu, and H. Jiang, *Origami lithium-ion batteries,* Nature Communications **5**, 1 (2014).

[108] N. Singh, C. Galande, A. Miranda, A. Mathkar, W. Gao, A. L. M. Reddy, A. Vlad, and P. M. Ajayan, *Paintable battery,* Scientific Reports **2**, 6 (2012).

[109] K. Jost, G. Dion, and Y. Gogotsi, *Textile energy storage in perspective,* Journal of Materials Chemistry A **2**, 10776 (2014).

[110] X. Wang, K. Jiang, and G. Shen, *Flexible fiber energy storage and integrated devices: Recent progress and perspectives,* Materials Today **18**, 265 (2015).

[111] T. Lv, Y. Yao, N. Li, and T. Chen, *Wearable fiber-shaped energy conversion and storage devices based on aligned carbon nanotubes,* Nano Today **11**, 644 (2016).

[112] S. Zhai, H. E. Karahan, L. Wei, Q. Qian, A. T. Harris, A. I. Minett, S. Ramakrishna, A. K. Ng, and Y. Chen, *Textile energy storage: Structural design concepts, material selection and future perspectives,* Energy Storage Materials **3**, 123 (2016).

[113] N. Espinosa, R. García-Valverde, and F. C. Krebs, *Life-cycle analysis of product integrated polymer solar cells,* Energy & Environmental Science **4**, 1547 (2011).

[114] B. J. Kim, D. H. Kim, Y.-Y. Lee, H.-W. Shin, G. S. Han, J. S. Hong, K. Mahmood, T. K. Ahn, Y.-C. Joo, K. S. Hong, N.-G. Park, S. Lee, and H. S. Jung, *Highly efficient and bending durable perovskite solar cells: toward a wearable power source,* Energy Environ. Sci. **8**, 916 (2015).

[115] S. Oshima, K. Matsunaga, H. Morimura, and M. Harada, *3D integration techniques using stacked PCBs and small dipole antenna for wireless sensor nodes,* , 3 (2012).

[116] F. Horiguchi, *Integration of series-connected on-chip solar battery in a triple-well CMOS LSI,* IEEE Transactions on Electron Devices **59**, 1580 (2012).

[117] G. Chen, M. Fojtik, D. Kim, D. Fick, J. Park, M. Seok, M.-t. Chen, Z. Foo, and D. Sylvester, *A Millimeter-Scale Nearly Perpetual Sensor System with Stacked Battery and Solar Cells,* **48**, 166 (2010).

[118] S. Lemey, F. Declercq, and H. Rogier, *Dual-band substrate integrated waveguide textile antenna with integrated solar harvester,* IEEE Antennas and Wireless Propagation Letters **13**, 269 (2014).

[119] J. Cai, C. Lv, and A. Watanabe, *Laser direct writing of high-performance flexible all-solid-state carbon micro-supercapacitors for an on-chip self-powered photodetection system,* Nano Energy **30**, 790 (2016).

[120] K. E. Jeon, T. Tong, and J. She, *Preliminary design for sustainable BLE Beacons powered by solar panels,* Proceedings - IEEE INFOCOM **2016-Septe**, 103 (2016).

[121] C. Li, M. Islam, J. Moore, J. Sleppy, C. Morrison, and K. Konstantinov, *Energy Harvest and Storage,* Nature Publishing Group **7**, 1 (2016).

[122] X. Dong, L. Chen, X. Su, Y. Wang, and Y. Xia, *Flexible Aqueous Lithium-Ion Battery with High Safety and Large Volumetric Energy Density,* Angewandte Chemie - International Edition **55**, 7474 (2016).

[123] Global Off-Grid Lighting Association, *Global Off-Grid Solar Market Report - Semi-Annual Sales and Impact Data*, Tech. Rep. (GOGLA, Lighting Global and Berenschot, 2018).

[124] M. Bhatia and A. Nicolina, *Capturing the Multi-Dimensionality of Energy Access* (Live Wire, 2014/16. World Bank, Washington, DC. ©World Bank, 2014).

[125] Wakawaka, *Datasheet,* Waka Waka Light – solar-powered LED flashlight (2014).

[126] Wakawaka, *Datasheet,* Waka Waka Power+ – solar-powered charger + light (2015).

[127] D.Light Design, *Datasheet,* D.light S30 solar lantern (2016).

[128] Freeplay Energy, *Datasheet,* Radiance – solar-powered lantern (2016).

[129] C. Clark, J. Summers, and Armstrong, *Innovative flexible lightweight thin-film power generation and storage for space applications,* in *Collection of Technical Papers. 35th Intersociety Energy Conversion Engineering Conference and Exhibit (IECEC)*, Vol. 1 (2000) pp. 692–698 vol.1.

[130] B. Nykvist and M. Nilsson, *Rapidly falling costs of battery packs for electric vehicles,* Nature Climate Change **5**, 329 (2015).

[131] A. Jäger-waldau, *PV Status Report 2016*, October (2016).

[132] W. Swiegers and J. Enslin, *An integrated maximum power point tracker for photovoltaic panels,* IEEE International Symposium on Industrial Electronics. Proceedings. ISIE'98 (Cat. No.98TH8357) **1** (1998), 10.1109/ISIE.1998.707746.

[133] R. H. Wills, S. Krauthamer, A. Bulawka, and J. P. Posbic, *The AC Photovoltaic Module Concept,* Proceedings of the 32nd Intersociety Energy Conversion Engineering Conference (IECEC) , 1562 (1997).

[134] J. H. R. Enslin, M. S. Wolf, D. B. Snyman, and W. Swiegers, *Integrated photovoltaic maximum power point tracking converter,* Ieee Transactions on Industrial Electronics **44**, 769 (1997).

[135] R. Y. Kim, C. S. Lim, H. J. Jung, and S. B. Cho, *A general-purpose integrated battery energy module for non-isolated energy storage system applications,* 2012 IEEE Vehicle Power and Propulsion Conference, VPPC 2012 , 1503 (2012).

[136] *Solar Power Optimizer - English,* .

[137] *Microinverter: Enphase Inverter Technology | Enphase,* .

[138] M. Acanski, Z. Ouyang, J. Popovic-Gerber, and B. Ferreira, *Very thin flexible coupled inductors for PV module integrated GaN converter,* Conference Proceedings - 2012 IEEE 7th International Power Electronics and Motion Control Conference - ECCE Asia, IPEMC 2012 **1**, 693 (2012).

[139] P. Mazumdar, P. N. Enjeti, and R. S. Balog, *Analysis and Design of Smart PV Modules,* IEEE Journal of Emerging and Selected Topics in Power Electronics **2**, 451 (2014).

[140] A. Dede, D. D. Giustina, G. Massa, M. Pasetti, and S. Rinaldi, *A smart PV module with integrated electrical storage for smart grid applications,* 2016 International Symposium on Power Electronics, Electrical Drives, Automation and Motion, SPEEDAM 2016 **40545387**, 895 (2016).

[141] S. Krauter and F. Ochs, *All-in-one solar home system,* Conference Record of the IEEE Photovoltaic Specialists Conference , 1668 (2002).

[142] J. F. Reynaud, C. Alonso, P. Aloisi, C. Cabal, B. Estibals, G. Rigobert, G. Sarre, H. Rouault, D. Mourzagh, F. Mattera, and S. Genies, *Multifunctional module lithium-ion storage and photovoltaic conversion of solar energy,* in *Conference Record of the IEEE Photovoltaic Specialists Conference* (2008) pp. 1–5.

[143] J. F. Reynaud, O. Gantet, P. Aloïsi, B. Estibals, and C. Alonso, *New adaptive supervision unit to manage photovoltaic batteries,* IECON Proceedings (Industrial Electronics Conference) , 664 (2009).

[144] J. F. Reynaud, O. Gantet, P. Aloisi, B. Estibals, and C. Alonso, *A novel distributed photovoltaic power architecture using advanced Li-ion batteries,* Proceedings of EPE-PEMC 2010 - 14th International Power Electronics and Motion Control Conference , 6 (2010).

[145] W. Grzesiak, P. Mackow, T. Maj, A. Polak, E. Klugmann-Radziemska, S. Zawora, K. Drabczyk, S. Gulkowski, and P. Grzesiak, *Innovative system for energy collection and management integrated within a photovoltaic module,* Solar Energy **132**, 442 (2016).

[146] V. Vega-Garita, A. P. Harsarapama, L. Ramirez-Elizondo, and P. Bauer, *Physical integration of PV-battery system: Advantages, challenges, and thermal model,* 2016 IEEE International Energy Conference, ENERGYCON 2016 (2016), 10.1109/ENERGYCON.2016.7514038.

[147] M. Ačanski, J. Popović-Gerber, and B. Ferreira, *Thermal modeling of the module integrated DC-DC converter for thin-film PV modules,* Proceedings of EPE-PEMC 2010 - 14th International Power Electronics and Motion Control Conference , 160 (2010).

[148] V. Vega-Garita, L. Ramirez-Elizondo, and P. Bauer, *Physical integration of a photovoltaic-battery system: A thermal analysis,* Applied Energy **208**, 446 (2017).

[149] M. Hammami, S. Torretti, F. Grimaccia, and G. Grandi, *Thermal and Performance Analysis of a Photovoltaic Module with an Integrated Energy Storage System,* Applied Sciences **7**, 1107 (2017).

[150] *SolPad - The smart home solar solution is here,* .

[151] R. Ciriminna, F. Meneguzzo, L. Albanese, and M. Pagliaro, *Solar street lighting: A key technology en route to sustainability,* Wiley Interdisciplinary Reviews: Energy and Environment (2016), 10.1002/wene.218.

[152] V. Vega-Garita, S. Garg, N. Narayan, L. Ramirez-Elizondo, and P. Bauer, *Testing a pv-battery integrated module prototype,* in *2018 IEEE 7th World Conference on Photovoltaic Energy Conversion (WCPEC)* (2018) pp. 1244–1248.

[153] N. Narayan, V. Vega-Garita, Z. Qin, J. Popovic-Gerber, P. Bauer, and M. Zeman, *A modeling methodology to evaluate the impact of temperature on solar home systems for rural electrification,* in *2018 IEEE International Energy Conference (ENERGYCON)* (2018) pp. 1–6.

[154] M. R. Palacin and A. de Guibert, *Why do batteries fail?* Science **351**, 1253292 (2016).

3

System Sizing Based on Loss of Load Probability

As defined in chapter 2, an optimally sized system is essential, because it impacts the total cost of the system and its performance. Therefore, this chapter introduces a sizing methodology based on system availability —in the form of loss of load probability (LLP)— that will be used as a reference for implementing a energy management in chapter 4, thermal analysis in chapter 5, and battery testing in chapter 6. Also, the boundaries of the *PV-battery Integrated Module* (*PBIM*) are explored based on the level of availability (LLP) that can be achieved using a single *PBIM*. The system is sized for a standalone solar home system composed of one PV panel and a battery pack. When sizing the *PV-battery Integrated Module* aspects such as the ratio of PV rated power to storage capacity and appropriate case studies must be determined. These two aspects are interrelated as different case studies or applications can lead to different optimum system sizes. The sizing method used in this thesis consists of an iterative process that varies the PV rating and battery capacity while evaluating its impact on LLP, which has to be minimized to ensure the continuity of the energy supply to the load. The model also takes into account the battery capacity degradation throughout the simulation and the thermal conditions expected in the *PBIM*, using an energy throughput aging model and a 1-D steady state thermal model. Moreover, the system is sized using a typical average load in rural Cambodia and a tier 3 profile defined by the multi-tier framework in the context of electricity access— which includes appliances such as TV, fridge, and radio— in order to explore the boundaries of a single *PBIM* in off-grid applications. Also, a basic energy management (EM) strategy that prioritizes load fulfillment either by solar power or battery discharging is proposed. The implementation of an EMS is further explored in chapter 4, where a grid-connected system is also studied.

This chapter is partially based on V. Vega-Garita, D. De Lucia, N. Narayan, L. Ramirez-Elizondo, and P. Bauer. *PV-Battery Integrated Module as a Solution for Off-Grid Applications in the Developing World*. IEEE International Energy Conference 2018 (2018) [1].

3.1. Introduction

Energy access remains as a challenge to overcome. It is estimated that 17% of world population have no access to electricity. Moreover, 95% of this population is located in developing regions like Asia and sub-Saharan Africa, of which 85% live in rural locations [2]. Hence, the widespread availability of solar resource drives its usage in countries in these latitudes, easing the access and becoming a global alternative for areas with and especially without connection to the electricity grid, as the case of rural Cambodia (studied in this chapter) which has a low electrification rate of 49.2% in 2014 according to the World Bank [3]. However, PV energy must be handled smartly because its power varies with the environmental conditions, resulting in an intermittent energy source. This intermittency and the mismatch between the power demanded by the loads and the solar generation makes the use of energy storage devices essential. Therefore, batteries are considered an integral component in off-grid systems due to their ability to react fast when power is demanded by the load, along with the possibility of storing energy for relatively long periods —months. Although the price of batteries and PV panels has decreased continuously during the last years [4, 5], an optimal battery and PV sizing is fundamental for reducing the up-front cost of the system particularly for applications in the developing world [6]. A PV-battery system can be size following intuitive methods such days of autonomy where the battery is able to store enough energy to supply the load for a previously defined number of days, but these methods tend to oversize the system and consequently result economically unfeasible.

Consequently, this chapter introduces an iterative sizing method based on the availability of the system (LLP), where PV and battery sizes are changed and the LLP is calculated. For the same location in rural Cambodia, two different load profiles were used as case studies to find optimum PV and battery combination that could be employed in the next chapters.

3.1.1. Contributions

This chapter contributes to

- formulate a methodology to find the optimum battery capacity and PV power rating based on loss of load probability (Section 3.3),
- quantify the impact of cycling on battery aging simulating the system dynamics for one year (Section 3.3.4),
- propose an integrated model that couples the thermal effects of the physical integration and the battery aging (Section 3.3.6), and
- explore the sizing boundaries of a single *PBIM* in the form of PV rating and battery capacity using two different load profiles (Section 3.4.4).

3.2. Definitions

Before introducing the features of the model for sizing the system, several terms must be defined as they will be used frequently throughout the chapter.

Loss of load probability

One criterion to determine the availability of an off-grid PV system is the loss of load probability. It is determined to calculate the relation between the energy not provided (E_{np}) by the energy sources and the energy required by the load (E_{load}) in a particular time frame. A low value of LLP is always desired because the system downtime is reduced leading to a more reliable system. LLP is computed using the equation that follows:

$$LLP = \frac{E_{\text{np}}}{E_{\text{load}}} \times 100 \quad [\%]. \tag{3.1}$$

Depending on the availability required by the application, the recommended values for LLP are 10% for appliances, 1% for domestic illumination, and 0.01% for telecommunication [7]. In this chapter, the calculated for a period of one year.

State of charge

The state of charge (SOC) relates to the energy remaining (E_{battery}) in the battery that can be extracted as a fraction of the rated capacity (E_{rated}), and can be expressed as follows

$$SOC = \frac{E_{\text{battery}}}{E_{\text{rated}}} \times 100 \quad [\%]. \tag{3.2}$$

State of health

The state of health (SOH) of a battery is a measure of the degradation suffered by the battery after a specified period. The SOH is the ratio of usable capacity (C_{actual}) to the nominal capacity C_{rated}, as per the following equation

$$SOH = \frac{C_{\text{actual}}}{C_{\text{rated}}} \times 100 \quad [\%]. \tag{3.3}$$

For a good approximation of SOH, long-term testing must be carried out. Therefore, in this paper, the manufacturer datasheet of the batteries selected for the *PBIM* module is used to estimate capacity fading. As can be seen in Figure 3.5, SOH depends on the number of cycles but also on the temperature of operation of the battery.

Cycling

A complete cycle occurs when the battery has been charged and discharge completely. In terms of energy, the total cycling (C) of a battery can be estimated by dividing the total energy processed through the battery ($E_{\text{throughput}}$) to the battery nominal capacity using the following equation

$$C = \frac{E_{\text{throughput}}}{2E_{\text{nominal}}}. \tag{3.4}$$

3.3. Methodology

As this chapter delves on system sizing, the location plays an important role as well as the application. In this case, rural Cambodia was selected considering the low percentage of rural electrification, and therefore, lack of connection to the electricity grid for many people [1]. Moreover, in a previous article of our research group [8], the energy needs of a particular community were mapped and resulted in a realistic average load profile for already installed solar home systems.

Having chosen the location, environmental conditions such as irradiation, ambient temperature, and wind speed were gathered to estimate the PV production and incorporate their influence on battery aging. These two effects are calculated using a 1-D steady state thermal model and a battery aging model based on energy throughput.

Based on the PV generation and load consumption, the power direction and magnitude is decided by performing power balance. Once the energy processed by the battery is calculated, the effect of cycling and temperature on aging can be quantified.

3.3.1. Inputs to the models

Meteorological data

The data for direct normal irradiance and diffuse horizontal irradiation, wind speed, and ambient temperature were obtained from Meteonorm for the selected place in rural Cambodia, Stung Treng (13.517°N, 105.967°E). The time step was 10 min for all the inputs. In Figure 3.1, the data series for a chosen year is depicted. The seasonal effects are evident in Figure 3.1a, where a considerable reduction in irradiation is observed in the middle of the year as a consequence of the rainy season. Also, an average increase in temperatures can be observed during the rainy season (Figure 3.1b), with the temperatures changing between 16°C to less than 40°C.

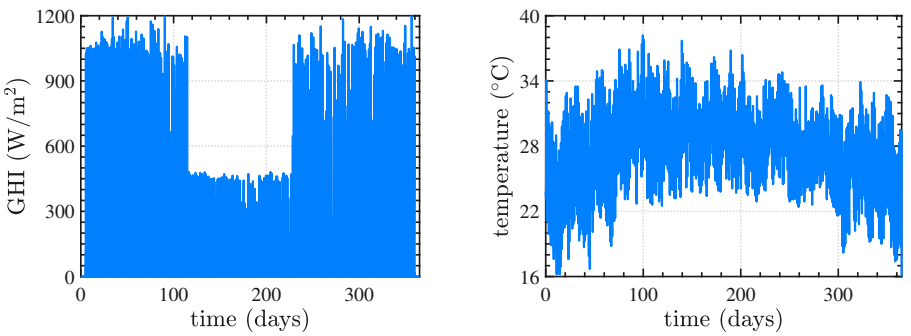

Figure 3.1: Yearly environmental data (a) global horizontal irradiation (GHI) and (b) ambient temperature. Location: Cambodia, Stung Treng (13.517°N, 105.967°E).

3.3.2. PV production

The PV production was estimated following the procedure described in [9], where the Global Horizontal Irradiation (GHI) is estimated from the contributions of the diffuse light and direct incident light. The optimum orientation of the PV panel is defined for the combination of azimuth and altitude where the GHI is maximum for an entire year. Once the optimum tilt of the PV panel is fixed, 24° facing south in this case, the temperature of the panel is calculated.

In this chapter, the temperature of the PV panel is expected to be higher than in a standard PV-battery system. The efficiency of the PV panel is calculate according to the temperature found by the thermal model defined in Section 3.3.3 using the following equation:

$$\eta_{\mathrm{pv}}(T) = \eta_{\mathrm{pv}}(\mathrm{STC})(1 + \beta(T_{\mathrm{pv}} - 25°C)) \quad [\%], \tag{3.5}$$

where β is the thermal coefficient, which value is 0.35 %/°C for a Si based solar panel and $\eta_{\mathrm{pv}}(\mathrm{STC})$ is the efficiency of the PV panel at standard test conditions (1000 W/m^2 and 25°C).

Based on this efficiency and knowing the irradiation falling into the PV panel (G_{m}) as well as the panel area (A_{pv}), the PV power is obtained solving the following equation:

$$P_{\mathrm{pv}}(T) = G_{\mathrm{m}}\eta_{\mathrm{pv}}(T)A_{\mathrm{pv}} \quad [\mathrm{W}]. \tag{3.6}$$

A crystalline silicon (c-Si) PV panel with a rated power of 320 W_p was selected as a reference for the PV sizing, and its features are presented in Table 3.1. This PV panel is scaled down by reducing its area in order to decrease the PV rating and power generated (see Equation 3.6), but properties such as efficiency and power coefficient (β) can be assumed invariable for simplicity.

Load profiles

In Figure 3.2, two loads for one household with a similar profile but different power values are illustrated. As can be observed, the power consumption slightly increases at sunrise, when the household members prepare food and switch on the lights. In the coming hours, the load demand remains low until a small increase is seen at lunchtime.

Table 3.1: Characteristics of the reference PV panel

Parameters	Value
P_{max}	320 W_p
V_{mpp}	54.7 V
I_{mpp}	5.86 A
V_{OC}	64.8 V
I_{SC}	6.24 A
η_{PV}	20%
A_{PV}	1.5 x 1 m^2
T_{NOCT}	47 °C
β	0.35%/°C

Table 3.2: Average daily load for different energy levels

Load	Average	Tier 3
Average daily load (Wh)	313.21	994.22

The most prominent peak occurs during the night, where multiple appliances demand power at the same time. After the peak, the power demand decreases steadily to the minimum.

The average load is a result of the mean consumption of 111 solar home systems equipped with 100 W_p and a 1200 Wh battery [8]. Additionally, the tier 3 load takes into account LED lights, mobile phone charging, radio, fan, TV, and fridge power consumption [10]. This load profile changes every day, and capture the more dynamic nature of energy consumption during the day compared to the average load. Table 3.2 presents the average energy needs for the load profile used in this chapter. As can be seen, tier 3 requires more than three times energy in comparison to the average load.

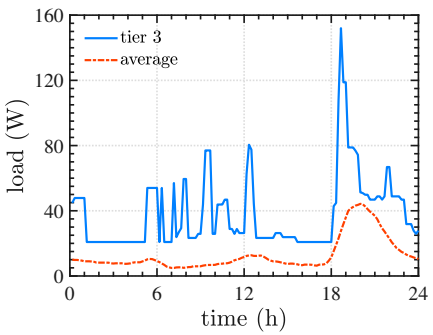

Figure 3.2: Load profile for an average daily load profile and a tiers 3. Based on [8, 10]

3.3.3. 1-D steady state thermal model

The 1-D thermal model considers the physical arrangement of the components of the *PBIM* as illustrated in Figure 3.3. The PV panel consists of 4 layers: glass, EVA (ethylene-vinyl acetate), c-Si (crystalline silicon), and Tedlar (Polyvinyl fluoride). The EVA serves as an encapsulant and adhesive to join the glass layer and the solar cells. EVA is also used to agglutinate the Si layer and the solar cell backsheet (Tedlar) together. Between the solar panel and batteries, there is an air gap, and an aluminum frame holds the battery pack. All these layers are considered in an unidimensional manner, which for the model means that all the heat produced by the PV panel is transferred in the direction of the x-axis.

The model takes into account the heat generated inside the solar cell and the battery pack. In the solar cell, the heat is assumed to be produced on the glass layer and the Si layer (q_{glass} and q_{Si}, respectively). Of the incident light, the majority is transmitted through the glass layer without integrating, but a 7% is assumed to be dissipated as heat

(q_{glass}) and a 3% reflected out of the glass surface. The remaining irradiance is either converted into electricity or in heat (q_{Si}). From the battery point of view, charging or discharging results in ohmic and reversible losses which contribute to heat generation inside the individual cells (q_{battery}).

The heat produced in the glass layer can be estimated using the following expression:

$$q_{\text{glass}} = \alpha G A_{\text{PV}} \quad [\text{W}], \tag{3.7}$$

where α is the light absorbed by the glass layer (7%), G is the incident global horizontal irradiation, and A_{PV} is the surface area of the PV panel.

The heat generated in the Si layer is calculated by subtracting from the incident light the heat generated on the glass layer, the portion of light reflected out of the PV panel, and the light converted into electricity in the Silicon, which can be written as follows

$$q_{\text{Si}} = (1 - \alpha - \beta)(1 - \eta_{\text{PV}}) G A_{\text{PV}} \quad [\text{W}], \tag{3.8}$$

where β is the light reflected at the glass surface and η_{PV} is the efficiency of the PV panel.

Inside the battery, a fraction of the power is converted into heat. It can be computed subtracting the complement of the efficiency of the battery from the charging or discharging power, as stated in the following equation

$$q_{\text{battery}} = IV(1 - \eta_{\text{battery}}) \quad [\text{W}], \tag{3.9}$$

where I is the charging ($-$) or discharging ($+$) current of the battery, V is the battery voltage, and η_{battery} is the efficiency of the battery (assumed as 96% for Li-ion).

The heat generated inside of the *PBIM* is dissipated to the surrounding in the form of convection (q_{c}) and radiation (q_{rad}) at the top (glass layer) and the bottom (aluminum frame). These are expressed in term of thermal resistances in equations 3.10 and 3.14.

$$q_{\text{c}} = \frac{T_{\text{s}} - T_{\text{amb}}}{R_{\text{c}}} \quad [\text{W}], \tag{3.10}$$

where T_{s} is the surface area (glass or frame temperature), T_{amb} is ambient temperature, and R_{c} is the thermal resistance related to convection.

The Equation to obtain R_{c} and R_{c} as introduced as follows:

$$R_{\text{c}} = \frac{1}{h_{\text{c}} A_{\text{surface}}} \quad [^{\circ}\text{Cm}^2/\text{W}], \tag{3.11}$$

$$R_{\text{rad}} = \frac{1}{h_{\text{rad}} A_{\text{surface}}} \quad [^{\circ}\text{Cm}^2/\text{W}], \tag{3.12}$$

where h_{c} is the convection coefficient, and h_{rad} is the radiation coefficient which formula is

$$h_{\text{rad}} = \epsilon\sigma(T_{\text{s}} + T_{\text{sky,g}})(T_{\text{s}}^2 + T_{\text{sky,g}}^2) \quad [1/\text{m}^2{}^{\circ}\text{C}], \tag{3.13}$$

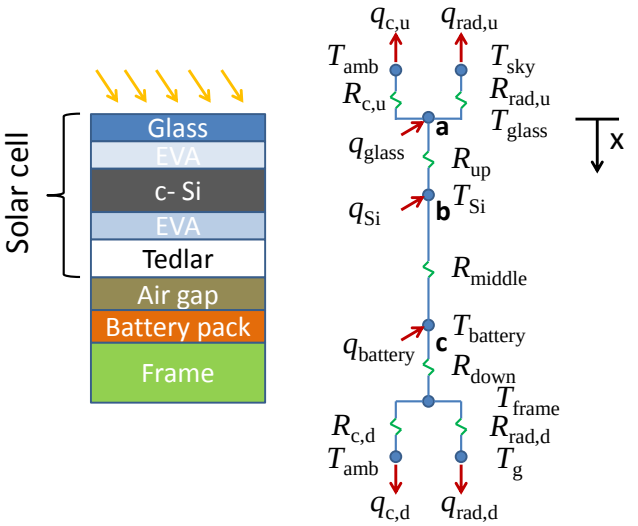

Figure 3.3: 1-D steady state thermal model based on thermal resistances.

$$q_{\text{rad}} = \frac{T_s - T_{\text{sky,g}}}{R_{\text{rad}}} \quad [\text{W}], \tag{3.14}$$

where T_s is the surface area (glass or frame temperature), $T_{\text{sky,g}}$ is the sky temperature (at glass layer) or ground temperature (at frame layer), and R_{rad} is the thermal resistance related to radiation.

The general definition of thermal resistance associated with conduction is introduced in Equation 3.15. Also, the values of layer length (L_{layer}), conduction conductivity are presented in Table 3.3.

$$R_{\text{layers}} = \frac{L_{\text{layer}}}{k_{\text{layer}} A_{\text{layer}}} \quad [^\circ\text{C/W}]. \tag{3.15}$$

From simplicity, the thermal resistances are grouped into three: R_{up}, R_{middle}, and

Table 3.3: Properties of the layers used to calculate the thermal resistances

layer	**L** (mm)	**k** (W/m°C)
Glass	3	1.38
EVA	0.5	0.38
c-Si	0.3	130
Tedlar	0.5	0.15
Air	50	0.0295
Battery	7.25	0.81
Frame	2	238

R_{down}. In equations 3.16, 3.17, and 3.18, the definitions of these resistances are introduced:

$$R_{\text{up}} = R_{\text{glass}} + R_{\text{eva}} + \frac{R_{\text{Si}}}{2} \quad [^{\circ}\text{C/W}], \tag{3.16}$$

$$R_{\text{middle}} = \frac{R_{\text{Si}}}{2} + R_{\text{eva}} + R_{\text{ted}} + R_{\text{air}} + \frac{R_{\text{battery}}}{2} \quad [^{\circ}\text{C/W}], \tag{3.17}$$

$$R_{\text{down}} = \frac{R_{\text{battery}}}{2} + R_{\text{frame}} \quad [^{\circ}\text{C/W}], \tag{3.18}$$

where R_{glass} is the thermal resistance of the glass layer, R_{eva} is the is the thermal resistance of the EVA layer, R_{Si} is the thermal resistance of the c-Si layer, R_{ted} is the thermal resistance of the Tedlar layer, R_{air} is the thermal resistance of the air gap, R_{battery} is the thermal resistance of the battery layer, and R_{frame} is the thermal resistance of the frame (aluminum).

As can be observed in Figure 3.3, four temperatures are of the interest of in the analysis, namely, T_{glass}, T_{Si}, T_{battery}, and T_{frame}. To obtain the value of these temperatures, a general energy balance is performed in Equation 3.19 and in nodes a, b, and c, as formulated in Equations 3.20, 3.21, and 3.22. By solving these equations every time step the thermal behavior of the solar cell and battery pack is estimated.

The general energy balance, which relates the heat generation and heat dissipation can be written as follows

$$q_{\text{glass}} + q_{\text{Si}} + q_{\text{battery}} = q_{\text{c}} + q_{\text{rad}}. \tag{3.19}$$

The energy balance in node **a**, **b**, and **c** are as follows

$$q_{\text{glass}} + \frac{T_{\text{Si}} - T_{\text{glass}}}{R_{\text{top}}} = \frac{T_{\text{glass}} - T_{\text{amb}}}{R_{\text{c,u}}} + \frac{T_{\text{glass}} - T_{\text{sky}}}{R_{\text{rad,u}}}. \tag{3.20}$$

$$q_{\text{Si}} = \frac{T_{\text{Si}} - T_{\text{glass}}}{R_{\text{top}}} + \frac{T_{\text{Si}} - T_{\text{battery}}}{R_{\text{middle}}}. \tag{3.21}$$

$$q_{\text{battery}} = \frac{T_{\text{Si}} - T_{\text{battery}}}{R_{\text{middle}}} + \frac{T_{\text{battery}} - T_{\text{frame}}}{R_{\text{down}}}. \tag{3.22}$$

3.3.4. Battery energy throughput aging model

The battery aging model employed in this chapter is based on energy throughput, and therefore, only includes the effects of cycling while ignoring calendar aging. Every time step in which the battery is active ($P_{\text{b}} \neq 0$), the energy processed is calculated along with the equivalent cycles using Equation 3.4. Once the amount of cycles is known as well as its relation with SOH (Figure 3.5 in this case), a small portion decreases the actual capacity of the battery due to the previous activity period. Consequently, in this model the battery capacity is dynamically changing after every period of activity.

The reduction of battery capacity is carried out using reference curves given by the battery manufacturer data sheet that correlates the cycling, SOH, and battery temperature. From Figure 3.5, it can be observed the linearity between SOH and the number of cycles for the different battery temperatures, when the influence of battery depth of discharge in not taken into account. Therefore, the SOH for a defined temperature and time step i ($SOH(i,T)$) is defined in the next equation as:

$$SOH(i,T) = mC(i) + 100, \quad [\%], \tag{3.23}$$

where m is the slope of the curve and $C(i)$ is the cycles performed in one-time step.

Having calculated the SOH, the capacity for the current time step ($C_{\text{battery}}(i)$) is calculated by Equation 3.24, where $C_{\text{battery}}(i-1)$ is the battery capacity during the previous time step $i-1$.

$$C_{\text{battery}}(i) = SoH(i,T)C_{\text{battery}}(i-1) \quad [\text{Ah}]. \tag{3.24}$$

The general battery degradation model is described in Figure 3.4, where the input to the model are the temperature and current of battery pack. Based on these inputs, the model calculates the remaining battery capacity of every time step considering the capacity of the previous instant.

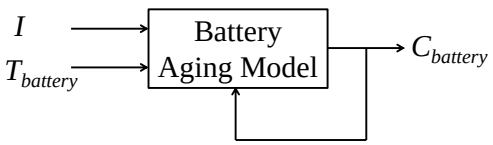

Figure 3.4: General battery aging model based on energy throughput with current and battery temperature as inputs.

As can be observed in Figure 3.5 for the selected battery technology, higher temperatures result in a faster degradation for the same amount of cycles [11]. The temperature of the battery in this chapter is calculated by means of the model described in Section 3.3.3. Moreover, it important to note that the battery chosen for this chapter is supported by the analysis and results presented in chapter 6.

3.3.5. Power flow management

The power flow management dictates the direction and priority of the power flow. In Figure 3.6, the steps followed to control the magnitude and direction of the power are illustrated. The power from the PV panel (P_{PV}) and the power demanded by the load (L) are used as a first reference point. If the PV power is bigger than the battery, the battery may be charged with the power excess. On the contrary, when the load demands more power than the produced by the PV panel the battery may be discharged. However, the charging of discharging of the battery strongly depends on the current state of the battery. Consequently, in a second step, the SOC of the battery is checked and compared to two reference points: the maximum and minimum allowable SOC, which have been defined as 10% and 90%, respectively. On the one hand, when the battery

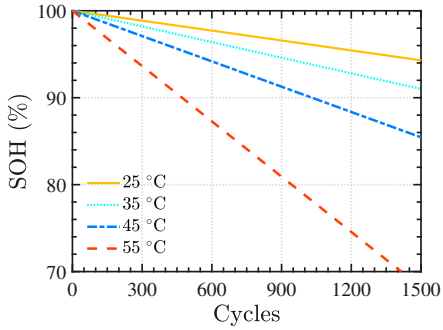

Figure 3.5: SOH as a function of cycles and battery temperature. The cycles are performed fully charging and discharging the $LiFePO_4$ pouch cell of 20 Ah. Source: [11].

power is required because of PV generation deficit and the SOC is below the or equal to the minimum (10%), the battery is not discharged. On the other hand, if the battery SOC has reached 90%, and there is an excess of PV generation, the excess must be dump as the battery is not able to accommodate more influx power.

The power flow model not only decides the magnitude of the power stored or released from the batteries (P_{battery}), it also calculates the actual power supplied to the load (P_{l}), the PV excess power dumped (P_{dump}), and deficit of power in cases where battery is discharged and PV power is not enough (P_{np}). For the four different combination defined by the power flow model, the formulae for estimating P_{b}, P_{l}, P_{dump}, and P_{np} are introduced in Equations from 3.25 to 3.40.

- $P_{\text{PV}} \geq L \;\&\; SOC \geq SOC_{\text{max}}$

$$P_{\text{battery}} = 0, \tag{3.25}$$

$$P_{\text{l}} = L, \tag{3.26}$$

$$P_{\text{dump}} = P_{\text{PV}} - L, \tag{3.27}$$

$$P_{\text{np}} = 0. \tag{3.28}$$

- $P_{\text{PV}} \geq L \;\&\; SOC < SOC_{\text{max}}$

$$P_{\text{battery}} = (P_{\text{PV}} - P_{\text{L}})\eta_{\text{battery}}, \tag{3.29}$$

$$P_{\text{l}} = L, \tag{3.30}$$

$$P_{\text{dump}} = 0, \tag{3.31}$$

$$P_{\text{np}} = 0. \tag{3.32}$$

- $P_{\text{PV}} < L \;\&\; SOC > SOC_{\text{min}}$

$$P_{\text{battery}} = \frac{-(L - P_{\text{PV}})}{\eta_{\text{battery}}}, \tag{3.33}$$

$$P_{\text{l}} = L, \tag{3.34}$$

$$P_{\text{dump}} = 0, \tag{3.35}$$

$$P_{\text{np}} = 0. \tag{3.36}$$

- $P_{\text{PV}} < L \;\&\; SOC < SOC_{\text{min}}$

$$P_{\text{battery}} = 0, \tag{3.37}$$

$$P_{\text{l}} = P_{\text{PV}}, \tag{3.38}$$

$$P_{\text{dump}} = 0, \tag{3.39}$$

$$P_{\text{np}} = L - P_{\text{PV}}. \tag{3.40}$$

The losses in the power conversion stages are neglected in this chapter to keep the model simple. Moreover, the battery efficiency is assumed 96% for the charging and discharging processes.

3.3.6. Integrated model

The thermal model (Section 3.3.3), battery aging model (Section 3.3.4), and power flow management model (Section 4.6.1) are combined to form an integrated model that link the individual model into one that more realistically reproduces the conditions expected in the *PBIM*. This integrated model is depicted in Figure 3.7, where it can be observed that the thermal model is interconnected to the power flow management model via the PV efficiency. The efficiency also defines the PV power output (P_{PV}) based on the temperature of the PV panel. Similarly, the current of the battery is needed to find the battery heat generation, which is feed to the thermal model. This process is iteratively repeated several times till the value T_{PV} and T_{battery} does not vary more than 0.01 °C. Once the iterative process between the thermal model and power management model has finished, the power needed from the battery (P_{battery}) and the temperature of the battery is used by the aging model to estimate the new capacity of the battery that is updated in the power management model for the next time step.

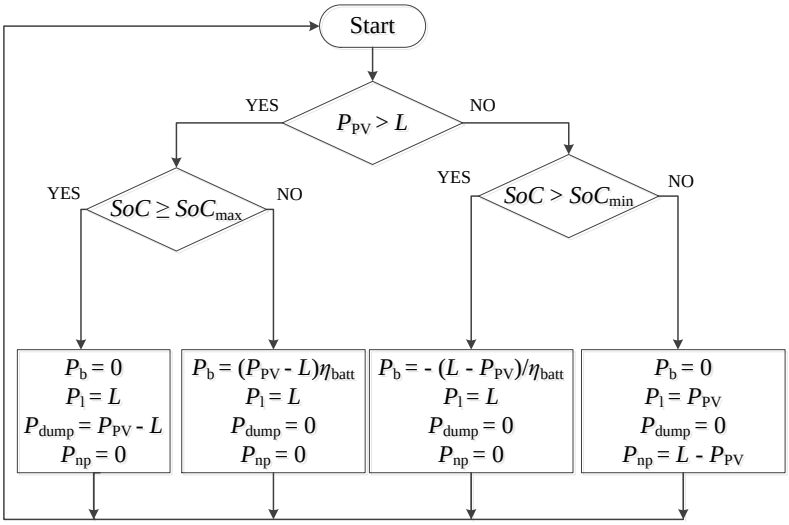

Figure 3.6: Power flow management for a battery efficiency (η_{battery}) is 96%.

The integrated model takes the inputs introduced in Section 3.3.1, and solves every time step for T_{PV} and T_{battery} as well as the C_{battery}. Additionally, LLP is calculated at the end of one-year simulation. Lastly, the simulations are performed for the range of PV ratings and battery capacities defined by the case study.

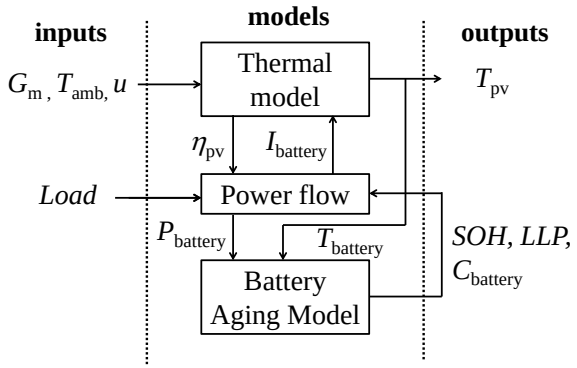

Figure 3.7: Integrated model that consits of a thermal model, a power flow management, and an aging model.

3.4. Results

This section starts by providing the results of simulation performed for the one-year data set. The integrated model examines the performance of the *PBIM* concerning the PV and battery temperature, power balance of the system, and battery capacity fading.

Moreover, the effect of two different load profiles on system sizing is studied. Particular attention is paid to the relationship between PV rating power and battery capacity in order to ensure a reliable power delivery. The expected battery degradation is included by having a look at battery cycling, also heavily influenced by the generation to storage ratio.

3.4.1. Integrated model

The results of the three models coupled in the integrated model are shown in Figure 3.8. In Figure 3.8a, it can be observed that the temperature of the PV panel reached almost 75°C, while the temperature of the battery pack is slightly higher than ambient temperature when the sun is shining, for an air gap of 4 cm. The battery pack raised its temperature to a peak of 37.1°C, ∼2.6°C more than the maximum reported ambient temperature for the selected day. Also, based on the same graph, the values of battery temperature follow ambient temperature in the absence of solar irradiation, but during the day the temperature of the PV panel is the responsible for the augment in temperature compared to ambient temperature —which provides the base temperature.

Figure 3.8b shows the power balance. Because the battery had remaining energy from the previous day, it is able to supply the load and started charging the solar radiation was enough to supply the load and produce an excess. For the selected day, the battery is completely charged and because of the considerable solar generation around half of the energy generated during a day by the PV panel must be dumped. Furthermore, the power no provided (E_{np}) stays at zero for the whole day. Later, in the afternoon, the energy harvested decreased, and the energy required by the load is again fulfilled by discharging the battery pack (negative power).

Different aging rates are observed for the three battery sizes introduced in Figure 3.8c (256, 512, and 1024 Wh), where a linear relationship between SOH and time is shown. However, the correspondence between battery size and SOH is not linear. This can be also be observed in Figure 3.8c, where the capacity reduced by 1.4, 0.8, and 0.4 for a battery pack with a capacity of 255, 512, and 1024 Wh, respectively. Moreover, because the aging model is based on energy processed —or energy throughput—, relatively speaking, a bigger battery pack processes less energy than a pack with a lower capacity, provoking a faster capacity fading for smaller battery packs.

3.4.2. Average load

Figure 3.9a depicts the interdependency between LLP, battery size and PV power ratings. On the one hand, there is a clear indication that low power PV rating results in elevated LLP values. On the other hand, an increase in battery size comes with an improvement in system availability, i.e., low probability of failure. However, there is a point at which (saturation point), for a given PV power, a further increase in battery capacity lead to a marginal reduction in LLP. The saturation occurs because the PV generation is the main source of energy, and therefore, it limits the storage positive effect on availability, which is related to the capacity of the battery to allocate solar energy in moments of low or zero PV generation.

Additionally, the saturation point of the contour show and tendency to increase as PV size and battery capacity augmented (Figure 3.9a). However, after a particular

value, around 200 W_p, the saturation point remained close to 300 Wh. Therefore, from the battery size perspective, the increasing the battery energy capacity beyond 300 Wh is not appropriate as the reduction in LLP is negligible after this point. Also, regarding system cost, a further increment in battery capacity contributes to elevating the cost, which is considered as a drawback that compromises system feasibility negatively.

From the contour plot in Figure 3.9b, two parameters affect battery SOH negatively: the raise on PV power and the reduction on battery size. These two trends are due to the relative increase in the battery energy throughput. Firstly, when the PV generation increases, for the same battery size, the energy charged and discharge from the battery increases leading to more cycles and causing a faster degradation. Secondly, for the same PV rating power, diminishing battery size results in a clear reduction on battery available capacity, because this results in more cycles for a small battery than for a bigger battery.

Referring back to Figure 3.9b, all the curves present an inflection point, more noticeable for the highest PV rating. This inflection point is directly connected to the LLP saturation point. It occurs at lower battery sizes for smaller PV rating, similarly to the

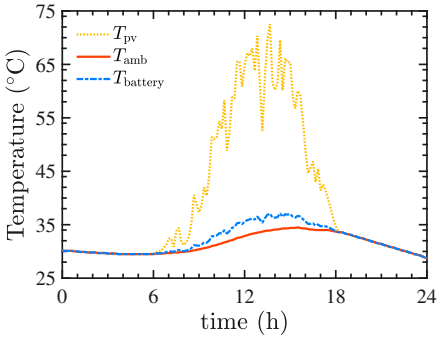

(a) Temperature variation.

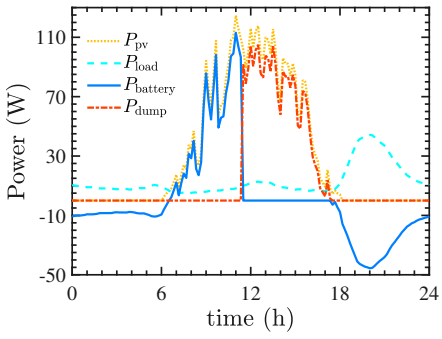

(b) Power flow variation.

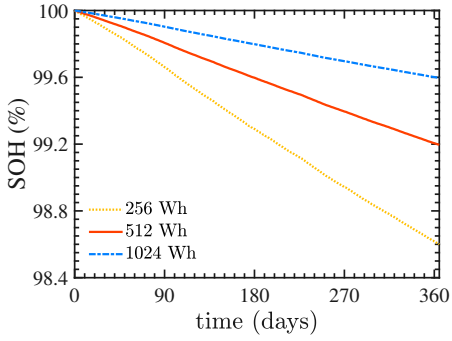

(c) SOH variation.

Figure 3.8: Results of the integrated model components temperature for the 97th day of the year (a) for an air gap of 4 cm, (b) power flow for a 160 W_p rated PV panel, and (c) SOH variation yearly variation.

LLP saturation point. Because the LLP value remains almost constant after saturation, the battery cycling increase more slowly beyond that region.

3.4.3. Tier 3

Tier 3 load profile represents a more realistic and energy demanding load when comparing to the previous average daily load profile (see 3.2). Therefore, it is expected that the PV generation required as well as the battery size needed should be superior in the tier 3 case study. Consequently, the saturation points in Figure 3.10a are found at larger battery sizes, for the same PV rating, than that the depicted by Figure 3.9a. Also, the saturation point of the LLP vs. battery size curves occurred around 700 Wh and stay merely constant irrespectively of the continuous raise on PV rating, as long as its power is more than 150 W_p.

In terms of SOH as a function of battery size and PV power, it can be seen an expected decrease in battery aging with oversized battery pack and low PV ratings as shown in Figure 3.10b. This is again associated with the more pronounced cycling undergone in cases of undersized batteries, due to more energy processed in cases of more solar generation. The change in the behavior of SOH vs. battery capacity, the observed inflection points, is caused by the fact that after a particular battery size, the use of the battery is more shallow and the degradation reduces its rate –for the same PV power. However, because even for the maximum PV rating the LLP value will not reach zero, the inflection points for tier 3 are not as considerable as in Figure illustrated in 3.9b.

The *PBIM* is limited by its physical size. PV panels exceptionally have areas that surpass 1.6 m^2, and PV panels (with $\eta_{pv} \approx 20\%$) with a peak power beyond 320 W_p are not common. Therefore, more PV generation is not feasible for the tier 3 load. The limitation on the area also restricts the battery sizing. Assuming that pouch cells Li-ion cells (20 Ah, 3.2 V, 0.036 m^2), as in [11], are integrated in the *PBIM* and that only a 75% of the total area is free, because power electronics is placed in the remaining 25%, only 33 cells could be located at the back side of the PV panel for maximum capacity of

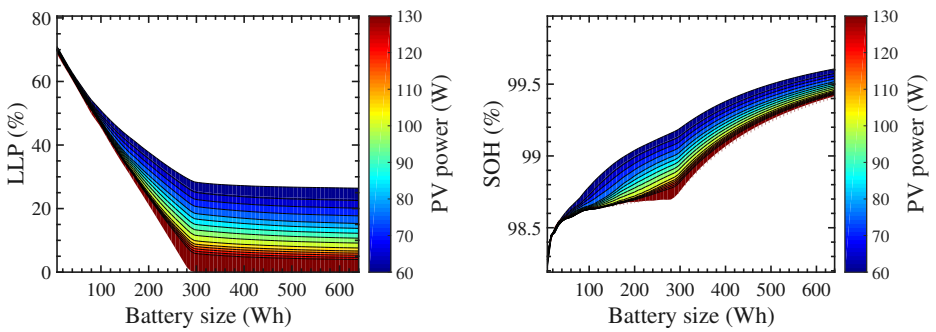

(a) (b)

Figure 3.9: (a) LLP and (b) SOH for an average daily load in rural Cambodia. Both metrics are estimated for various PV ratings.

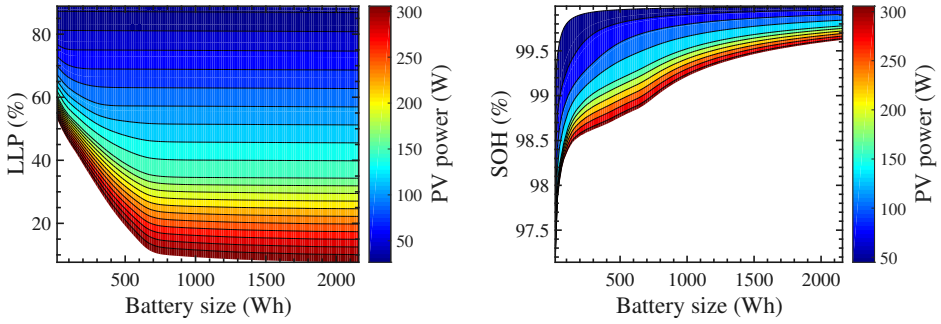

(a) (b)

Figure 3.10: (a) LLP and (b) SOH for a tier 3 load profile. Both metrics are estimated for various PV ratings.

Table 3.4: Optimum system sizing for an LLP below 10%.

Case	PV rating (W_p)	Battery capacity (Wh)	LLP (%)	SOH (%)
Average daily load	107	296	9.35	98.86
Tier 3	320	864	9.85	99.04

2,1 kWh – the limit in Figure 3.10.

3.4.4. Optimum sizing

For defining an optimum system, size is vital to set the level of system availability according to the application. Following the LLP values suggested in Section 3.2 for appliances, 10% is the reference value to find the minimum battery and PV size needed to satisfy both loads. Table 3.4 presents the combination of PV ratings and battery capacities able to ensure an LLP below 10%.

Additionally, it is important to point out that the minimum achievable LLP for the tier 3 load is 7.16%, and this can only be reached by raising the battery capacity to 2.1 kWh because augmenting PV rating is not physically possible. In the case of the average daily load, the LLP could be reduced to zero when a PV panel of 320 W_p and battery pack with a capacity of 296 Wh, or with a panel of 160 W_p and a battery of 520 Wh.

3.5. Conclusions

This chapter proposes a general sizing methodology that serves as a base for finding the boundaries of the *PBIM* and that will be used as a reference in the next chapters of this thesis. The boundaries of a single *PBIM* are studied based on the minimum PV rating and battery capacity required to reliably satisfy a predefined load profile. The methodology consists on an iterative sizing method that varies the PV rating and battery capacity while evaluating its impact on the system availability, viz. loss of load probability (LLP). The sizing exercise was performed for two load profiles in rural Cam-

bodia: a daily average load and a tier 3 load. For both case studies, an increase in PV generation and energy storage help lowering LLP, but at the same time resulting in more battery cycling and a faster degradation. However, in absolute terms, the optimum sizing for both systems required a different combination of PV panel peak power and battery pack storage capacity, which is mainly driven by the representative disparity on energy consumption in each case. When the minimum allowed LLP is set at 10%, the size of the PV power are 107 and 320, respectively W_p. Similarly, when it comes to the battery size, the size of tier 3 (864 Wh) load represents almost three times the optimum battery capacity for the average daily load (296 Wh). Chapter 3 serves as a starting point for chapter 4 — where the energy management system is introduced—, defining an intuitive sizing methodology to explore the limits on PV generation and energy storage capacity of an individual *PBIM*.

References

[1] V. Vega-Garita, D. D. Lucia, N. Narayan, L. Ramirez-Elizondo, and P. Bauer, *Pv-battery integrated module as a solution for off-grid applications in the developing world,* in *2018 IEEE International Energy Conference (ENERGYCON)* (2018) pp. 1–6.

[2] International Energy Agency, *Energy for All: Financing access for the poor (Special early excerpt of the World Energy Outlook 2011),* World Energy Outlook 2011 , 52 (2011).

[3] World Bank, *Access to electricity, rural population,* (2014).

[4] International Energy Agency, *Electricity Storage and Renewables: Costs and Markets to 2030),* (2017).

[5] International Energy Agency, *Technology Roadmap Solar Photovoltaic Energy,* (2014).

[6] N. Narayan, J. Popovic, J. C. Diehl, S. Silvester, P. Bauer, and M. Zeman, *Developing for developing nations: Exploring an affordable solar home system design,* GHTC 2016 - IEEE Global Humanitarian Technology Conference: Technology for the Benefit of Humanity, Conference Proceedings , 474 (2016).

[7] S. Silvestre, *Chapter ii-1-c - review of system design and sizing tools,* in *McEvoy's Handbook of Photovoltaics (Third Edition)*, edited by S. A. Kalogirou (Academic Press, 2018) third edition ed., pp. 715 – 734.

[8] T. Den Heeten, N. Narayan, J.-C. Diehl, J. Verschelling, S. Silvester, J. Popovic-Gerber, P. Bauer, and M. Zeman, *Understanding the present and the future electricity needs: Consequences for design of future Solar Home Systems for off-grid rural electrification,* 2017 International Conference on the Domestic Use of Energy (DUE) , 8 (2017).

[9] K. Jäger, O. Isabella, A. H. Smets, R. Van Swaaij, and M. Zeman, *Solar Energy: The physics and engineering of photovoltaic conversion, technologies and systems* (UIT Cambridge, 2016).

[10] N. Narayan, Z. Qin, J. Popovic-Gerber, J.-C. Diehl, P. Bauer, and M. Zeman, *Stochastic load profile construction for the multi-tier framework for household electricity access using off-grid dc appliances,* Energy Efficiency (2018), 10.1007/s12053-018-9725-6.

[11] A123 Systems, *Battery Pack Design , Validation , and Assembly Guide using A123 Systems AMP20M1HD-A Nanophosphate Cells,* , 1 (2014).

4

Energy Management System

Previously, chapter 3 discussed about the importance of system sizing. The choosing of the optimum PV rating and battery capacity is heavily dependent on the application but also on the criteria applied for defining the direction of the power flows. However, for managing the power flows, the system architecture must be established among the various options, along with the converter topology needed in every power conversion stage. Therefore, this chapter focuses on proposing an energy management system (EMS) that allows fulfillment of the load by optimally controlling the PV generation and the charging and discharging process of the battery pack. After analyzing the possible architectures, based on safety and system control complexity, the DC coupled architecture was selected. By controlling the boost converter for the PV panel, the buck-boost for the battery, and inverter the *PV-battery Integrated Module* (*PBIM*) is able to perform fundamental functions such as maximum power point tracking, PV curtailment, and battery charging and discharging. A model of the EMS was built to evaluate its behavior in three case studies, viz. off-grid solar home system, constant load, and peak shaving. The results show that the proposed EMS is able to perform within the defined modes of operation in conditions of variable solar generation with a dynamically changing load.

This chapter is based on V. Vega-Garita, M.F Sofyan, N. Narayan, L. Ramirez-Elizondo, P. Bauer. *Energy Management System for the Photovoltaic Battery Integrated Module*, Energies (2018) [1].

4.1. Introduction

To maximize the usage of clean energy produced by the PV panel, it is fundamental to define the appropriate times to charge and discharge the battery pack. For this reason, several energy management systems (EMS) have been proposed in the literature [2, 3]. In [4], self-consumption is prioritized taking into account the electricity prices while using model-based predictive control. The same control concept has been used to enable peak-shaving in grid-tied systems, including day ahead information to improve the effectiveness of the power management [5].

A previous paper has integrated a solar panel together with a servomotor, power electronics, and batteries that can be mounted in a wall; the PV panel position is dynamically controlled via a single axis solar tracker, demonstrating its applicability for a constant load [6]. In the case of static physically integrated PV battery systems, such as the *PBIM*, several studies have touched upon the energy management system and system architectures. According to [7], several commercial components can be picked based on the characteristics of the systems and coupled to operate the device. One element optimizes the PV output, while the charging and discharging processes are controlled in two different power stages. However, it is not clear how the power flows are controlled for the applications identified — camping, monitoring, and mobile systems.

Similarly, in [8], an electronic control unit includes a converter in charge of performing maximum power-point tracking (MPPT), a battery charge/discharge controller, and a battery management system. Particular interest is given to the battery management [9], where battery operation conditions are monitored closely including state of health, temperature, and state of charge levels. As a continuation, a boost converter is proposed to take care of the PV optimal operation, wherein three switches control the power flow [10]. There, just three modes are allowed: PV directly to load, PV to battery, or battery to load. Despite the progress shown in the previous papers, a discussion about the different architectures that can be used in integrated devices has not been explored. Neither the application of this kind of device to both off-grid and grid-connected (peak-shaving) systems using a common architecture, nor the possibility to use the battery together with the solar power to supply the load in particular cases have been thoroughly analyzed.

Therefore, this chapter focuses on choosing a suitable electrical architecture for the *PBIM* that enables the advantages provided by using a smart energy management system. The converter's control is also proposed to be able to perform MPPT, PV curtailment, and battery charging or discharging for an off-grid, constant load, and peak-shaving case studies.

4.1.1. Contributions of the chapter

In this chapter, the following contributions can be highlighted.

- A suitable system architecture for a PV-battery integrated device is selected based on systems complexity and number of conversion stages (Section 4.2).
- An EMS is proposed to manage the DC/DC converters and perform MPPT, excess solar curtailment, and battery charging and discharging (Section 4.3).

- Seven modes of operation were introduced to set the possible power flow directions in applications such as off-grid solar home system, constant load, and peak-shaving (Section 4.3.3).

4.2. System architecture

This section presents three system architectures that could be used to control the *PBIM* together with a qualitative analysis of their advantages and disadvantages with the objective to find the most suitable one.

4.2.1. In line

This architecture is the simplest due to its minimum number of components (Figure 4.1a), one unidirectional DC/DC and one unidirectional DC/AC converters. The DC/DC converter takes care of performing MPPT, and it is typically sized based on the rated PV power. The inverter, on the other hand, must be sized not just by considering the maximum PV output but also taking into account the maximum load power demand and the battery highest power defined by the manufacturer or application. This is because at specific instances both PV and battery could supply the load at maximum power if demanded by the load.

Contrary to the PV panel, which is attached to the DC bus through a DC/DC converter, the battery is linked directly to the DC bus, which could compromise its safety in cases of short circuit [11, 12]. Because of the lack of control over the discharging and charging processes in the in line architecture due to the absence of a converter for the battery, the battery's safety could be now put in jeopardy due to high temperatures that could lead to thermal runaway in cases of extremely high discharging currents [13]. Moreover, the battery pack voltage in such a configuration is limited by the fixed voltage of the DC bus, and therefore battery pack voltage can not be updated if needed. Additionally, because the voltage of battery sets the bus voltage, the input voltage perceived by inverter would change accordingly, inducing possible instabilities.

4.2.2. DC coupled

In comparison to the previous architecture, the battery pack is coupled to a bidirectional converter, see Figure 4.1b. In terms of components sizing, the battery pack is not limited by the defined DC bus voltage as seen in the in line architecture, resulting in a more flexible architecture. The battery converter and inverter power rating are decided based on the load maximum allowable power. By adding the battery converter, the DC bus can be controlled and monitor more easily while protecting the battery pack. Also, the input voltage of the inverter would be more stable, when compare to the in line architecture.

However, because just one DC/AC converter is used, its power rating is limited by the PV and battery ratings. Moreover, the DC/AC converter is likely to fail as the power from both energy sources is processed through the DC/AC converter [14]. This issue also holds for the in line architecture.

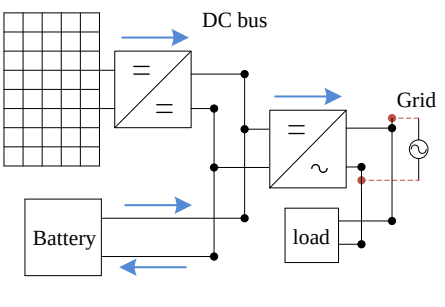

(a) In line architecture

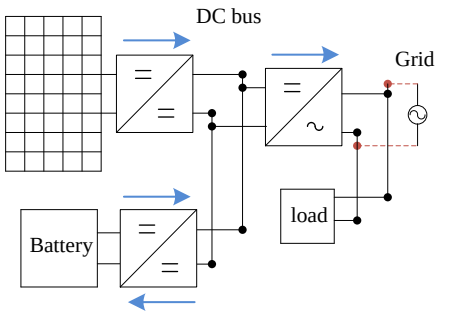

(b) DC coupled architecture

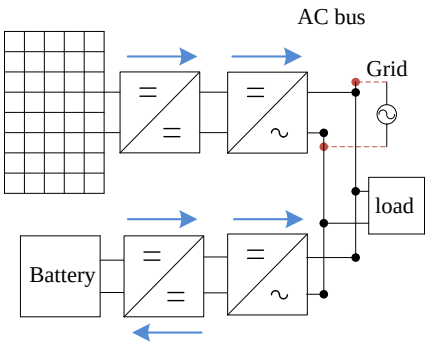

(c) AC coupled architecture

Figure 4.1: *PV Battery-Integrated Module* (*PBIM*) possible architectures: (a) in line, (b) DC coupled, and (c) AC coupled.

4.2.3. AC coupled

In an AC coupled architecture, the PV panel and the battery pack share a single AC bus (Figure 4.1c). From the PV side, this architecture is composed of a unidirectional DC/DC converter and an additional inverter, while from the battery side the DC/DC converter must be bidirectional along with an individual inverter.

In this architecture, the battery pack and the PV panel ratings can be chosen independently, providing flexibility regarding system sizing and enabling modularity, i.e., PV or battery sizes could be upgraded without changing inverter size. However, since this architecture has two DC/AC converters, their phases must be synchronized, requiring the implementation of phase control, increasing the complexity of the controller.

4.2.4. Selecting the architecture

In Table 4.1, the pros and cons of each architecture are summarised as a guide to chose the architecture. Although the simplest architecture is the in line with the least number of conversion steps, the issues related to battery safety (as introduced in [11–13]) and negative impact on battery lifetime together with the DC bus voltage instability make this architecture discardable. Both the DC and the AC couple architectures avoid this

Table 4.1: Pros and cons of possible architectures for the *PBIM*.

Architecture	Pros	Cons
In line	simplest	possible safety issues for the battery pack
DC coupled	simple and safe for batteries	single point of failure
AC coupled	easy to change battery capacity and PV rating	maximum number of converters and high control complexity

problem. Consequently, control complexity is selected as a critical parameter to decide between these two architectures. In this regard, the AC coupled architecture is more complicated than the DC coupled, as more converters need to be controlled along with the fact that an additional stage must be added to ensure phase synchronization. As a result, for the *PBIM* the DC coupled architecture is selected and will be used from now on in this thesis.

In this chapter, the DC voltage has been set to be higher than the PV voltage and the maximum battery voltage cells when completely charged. Therefore, for the solar panel, a unidirectional boost converter is required to increase the voltage from to the DC bus voltage reference. Also, a buck-boost converter is selected for the battery to step up the voltage when power is extracted from the battery, and to step down the bus voltage when battery is directly powered from solar. The battery voltage is based on the amount of batteries connected series. For instance, for the off-grid cases study the defined DC bus voltage was 36V; therefore, 10 cells are the maximum that can be connected in series. Otherwise, the battery voltage could surpass the DC bus voltage for $LiFePO_4$ technology.

4.3. Controlling the converters

In this section, the procedure followed to define the power flow directions and control the converters for the chosen architecture is proposed. For doing so, various modes of operation and control methods are introduced to adjust the duty cycle of the converters and to ensure an efficient power delivery within the operating limits. It is important to clarify that the inverter operates in constant modulation while the DC bus is kept at its reference value, which allows us to avoid the inverter's control for simplicity of the presented analysis.

4.3.1. PV converter

The PV converter is a unidirectional boost converter in charge of performing MPPT and PV curtailment. By setting a voltage reference, the DC/DC converter discriminates between these two modes of operation.

MPPT and curtailment

The PV voltage reference is set based on the desired converter mode of operation as can be seen in Figure 4.2a.

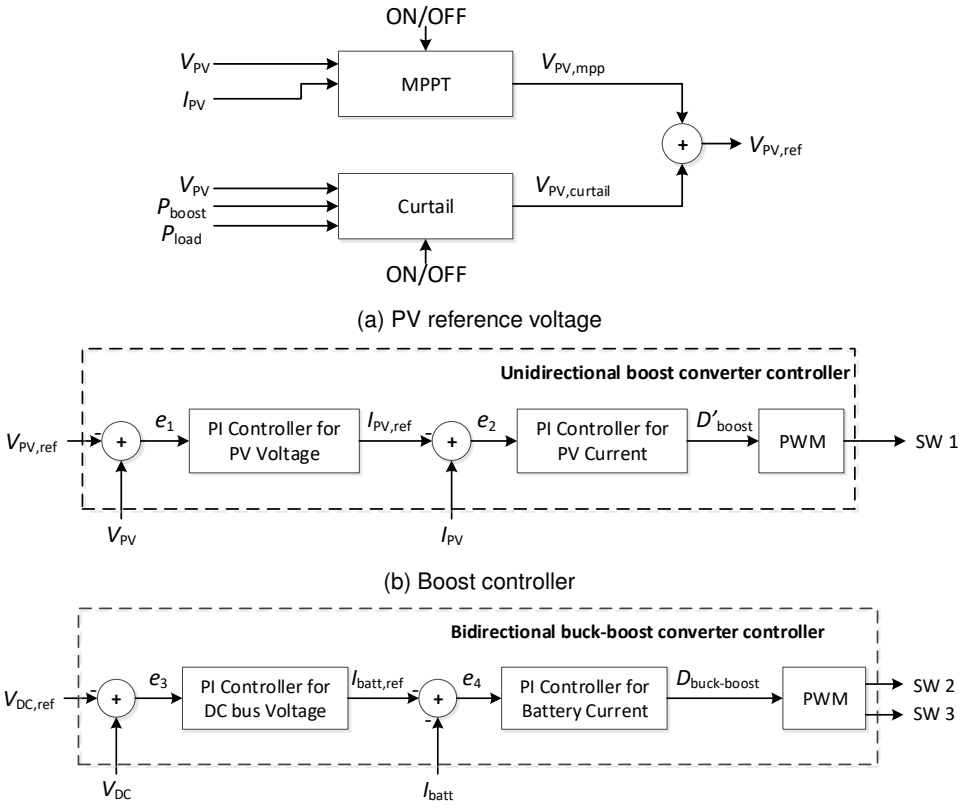

Figure 4.2: Feedback loops for (a) PV reference control, (b) feedback loop for boost converter, and (c) feedback loop for buck-boost converter.

When the MPPT mode is inactive, the PV-curtail mode of operation sets voltage reference; otherwise, the PV panel will operate at MPP. Equation 4.1 is employed to determine the solar power output (P_{PV}) when the MPPT condition is met, whereas Equation (4.2) defines it when the PV curtailment mode is active

$$P_{\mathrm{PV}} = V_{\mathrm{PV,mpp}} I_{\mathrm{PV,mpp}}. \tag{4.1}$$

$$P_{\mathrm{PV}} = V_{\mathrm{PV,curtail}} I_{\mathrm{PV,curtail}}. \tag{4.2}$$

Among the various methods to achieve MPP tracking, the incremental conductance MPPT method was used in this chapter based on a previous paper [15].

The PV curtailment is related to the instances where the PV generation exceeds the energy needed by the load, and the battery is not able to store the excess. In off-grid systems, the PV power must be dumped to maintain the power balance and a constant DC voltage. Once the unbalance is detected, the operating point of the PV

panel should be shifted to a region that results in lower PV efficiency. To accomplish this, the PV voltage reference is slightly increased moving the operating point of the solar panel to the right of the power-voltage curve, while reducing the power. Even though the rate of change at the right side of the power-voltage curve is faster than a voltage change to the left side regarding power reduction, it is beneficial for the boost converter as it can operate in a narrow duty cycle range with a small change in PV voltage. This concept, which defines $V_{\mathrm{PV,curtail}}$, is used for feedback loop control of the DC/DC boost converter as the PV voltage reference.

PV converter (boost converter)
To determine the duty cycle of the converter switch (SW 1), the feedback loop control shown in Figure 4.2b is used. The feedback loop control consists of two proportional-integral (PI) controllers; the first loop sets the panel current and the second the voltage.

The reference voltage of the panel is obtained from the MPPT or curtailment process as indicated previously. After that, the pulse width modulation (PWM) generator receive the information, which is a result of the previously determined D'_{boost} (see Equation A.4). Please refer to Appendix A.1, where the equations and coefficients used for this converter are summarized.

4.3.2. Battery converter (buck-boost)

Figure 4.2c presents the feedback control loop that defines the required duty cycle for the switches SW 2 ($D_{\mathrm{buck\text{-}boost}}$) and SW 3 (1-$D_{\mathrm{buck\text{-}boost}}$) (see Equation A.8). They are estimated based on two PI controllers; the first of them set the battery current while the second the DC bus voltage. As previously described, the PWM establishes the duty cycles of SW 2 and SW 3 to set the bus voltage.

4.3.3. Modes of operation

To study the power flow directions, 7 modes of operation describe all the possible cases. These modes are represented in Figure 4.3 and are explained as follows.

- **Mode 1**: PV produces power at MPP, while the battery is discharging with the bidirectional converter boosting the voltage. The inverter is active, and the load is fulfilled
- **Mode 2**: PV produces power at MPP, while the battery is charging with the bidirectional converter stepping down the voltage. The inverter is on, and the load is supplied.
- **Mode 3**: The solar panel is disconnected, and the converter switched off. The battery is discharged while the converter boosts the voltage, the DC/AC converter is active, and the load is powered.
- **Mode 4**: The PV produces power at a lower value than MPP, while the battery is discharging with the bidirectional converter boosting the voltage. The inverter is active, and the load is powered. This mode is only present in the off-grid case study as the PV surplus cannot be given to electricity grid.

- **Mode 5**: All the converters are switched off. This tends to occur in when the battery is empty at night.
- **Mode 6**: The solar generation performing at MPPT is solely supplying the load. This mode occurs only on the peak-shaving case when the battery is full, and its energy is saved to be used in peak times.
- **Mode 7**: The PV power generated at MPP is exclusively used to charge the battery while the bidirectional converter steps down the voltage.

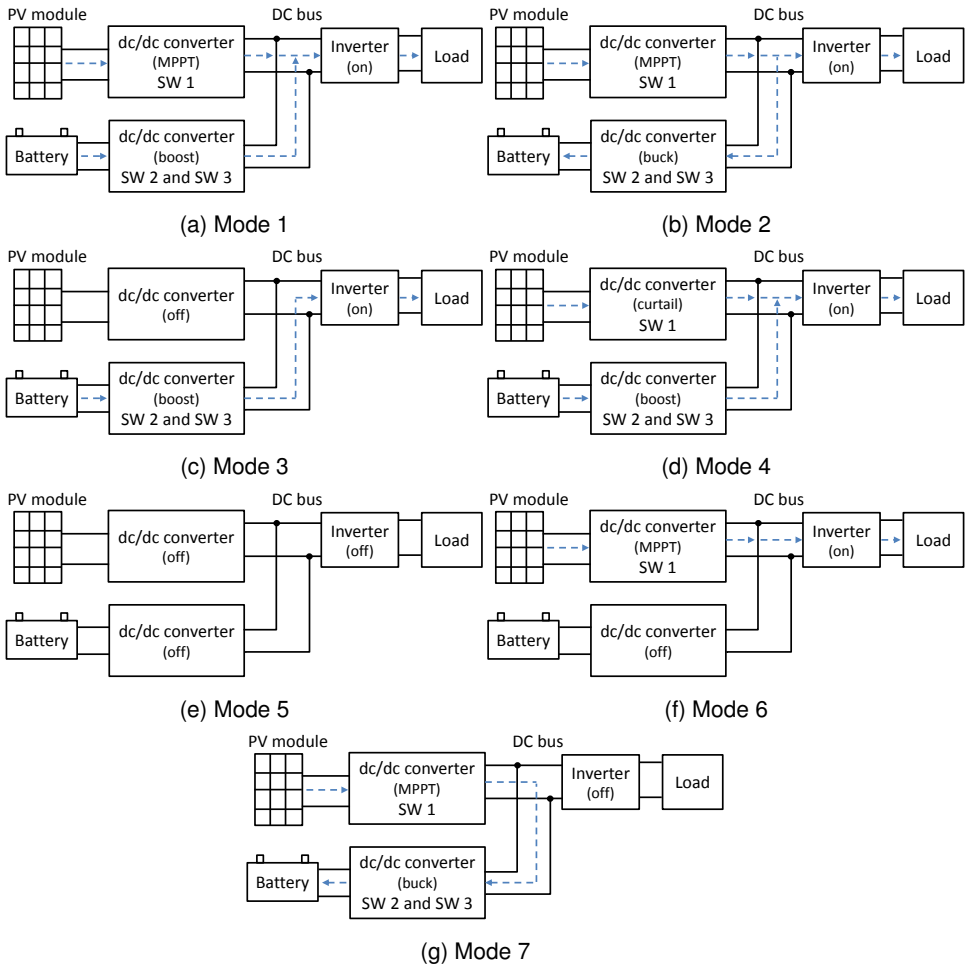

Figure 4.3: Power flow directions for the 7 modes of operation: (a) Mode 1, (b) Mode 2, (c) Mode 3, (d) Mode 4, (e) Mode 5, (f) Mode 6, and (g) Mode 7.

Similarly, Table 4.2 summarizes the relationship between the modes of operation and the activity of the converters.

Table 4.2: Converter operation for various modes of operation.

Converter	Mode 1	Mode 2	Mode 3	Mode 4	Mode 5	Mode 6	Mode 7
Unidirectional	MPP	MPP	OFF	Curtail	OFF	MPP	MPP
Bidirectional	Boost	Buck	Boost	Boost	OFF	OFF	Buck
Inverter	ON	ON	ON	ON	OFF	ON	OFF

Please refer to Appendix A, where the transient analysis is performed to the PV and battery converters.

4.4. Energy management

In this section, three case studies are explored: an off-grid, constant load, and peak-shaving for a grid-connected system. The particularities of each one, the power balance equations, and the energy management criteria are introduced as follows.

4.4.1. Off-grid

Off-grid solar systems only rely upon the PV power and store energy inside the batteries to supply the load, and consequently, a smart energy management is fundamental to administrate moments of energy deficit and excess. As introduced by Figure 4.4a, the solar energy must be used to directly supply the load and the energy surplus stored in the batteries to be used during the night. However, sometimes the solar generation is not enough and must be complemented by discharging the batteries. Other times, the solar energy is abundant and the batteries full. Therefore, the solar generation should be curtailed to maintain the power balance.

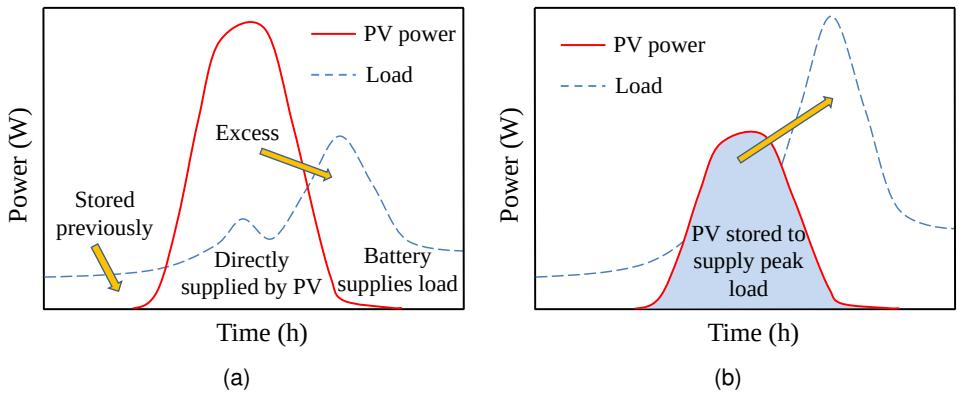

Figure 4.4: Energy management for (a) off-grid and (b) peak-shaving concepts.

The power flow is decided based on the flowchart shown in Figure 4.5, where the upper and lower limits for the SOC are set to determine the modes of operation. Six modes are used in this application, and the power balance equations for each mode

are introduced as follows.

- Mode 1

$$P_{\text{boost}} \cdot \eta_{\text{inv}} + P_{\text{batt}}^{\text{out}} \cdot \eta_{\text{buck-boost}} \cdot \eta_{\text{inv}} - P_{\text{load}} = 0. \tag{4.3}$$

- Mode 2

$$P_{\text{boost}} \cdot \eta_{\text{inv}} - P_{\text{batt}}^{\text{in}} \cdot \eta_{\text{buck-boost}} - P_{\text{load}} = 0. \tag{4.4}$$

- Mode 3

$$P_{\text{batt}}^{\text{out}} \cdot \eta_{\text{buck-boost}} \cdot \eta_{\text{inv}} - P_{\text{load}} = 0. \tag{4.5}$$

- Mode 4

$$P_{\text{boost,curtail}} \cdot \eta_{\text{inv}} + P_{\text{batt}}^{\text{out}} \cdot \eta_{\text{buck-boost}} \cdot \eta_{\text{inv}} - P_{\text{load}} = 0. \tag{4.6}$$

- Mode 5

$$P_{\text{fail}} = P_{\text{load}}. \tag{4.7}$$

- Mode 7

$$P_{\text{boost}} \cdot \eta_{\text{buck-boost}} - P_{\text{batt}}^{\text{in}} = 0. \tag{4.8}$$

Due to the difficulty to match the load when performing PV curtailment (mode 4), a new intermediate SOC upper level (85%) is introduced to prevent sudden and frequent changes between modes 2 and 4. If mode 4 was operational in the previous time step, and the SOC is higher than 85%, mode 4 remains operational in the current time step mode prevails until SOC is lower than 85%.

Also, an intermediate SOC lower level is employed to prevent sudden changes between modes 1 and 7. When the mode 7 was active previously and the SOC is below 15%, the integrated module keeps operating in mode 7 as long as SOC is above 15%, as can be appreciated in Section 4.6.1.

4.4.2. Peak-shaving

In peak-shaving applications, the primary purpose is to partially supply the residential load by a combination of previously stored solar energy from the battery and instantaneous solar during peak times to reduce the electricity bill. Unlike off-grid systems, where the availability of the system only relies on the battery pack and solar energy, the load can be met by using energy from the grid. Therefore, the power flows must be managed differently. In this case, the battery is charged directly from solar energy, and once it is full, the PV production can be used to also deliver power to the load as Figure 4.4b shows.

According to the flowchart depicted in Figure 4.6, the definition of peak is related to a particular time in a day. The charging and discharging times can be programmed while checking if the actual battery SOC is between the defined limits. Only modes 1, 3, 5, 6, and 7 are used in this case. The power balance for all the modes is as follows.

- Mode 1

$$P_{\text{boost}} \cdot \eta_{\text{inv}} + P_{\text{batt}}^{\text{out}} \cdot \eta_{\text{buck-boost}} \cdot \eta_{\text{inv}} + P_{\text{grid}} - P_{\text{load}} = 0. \tag{4.9}$$

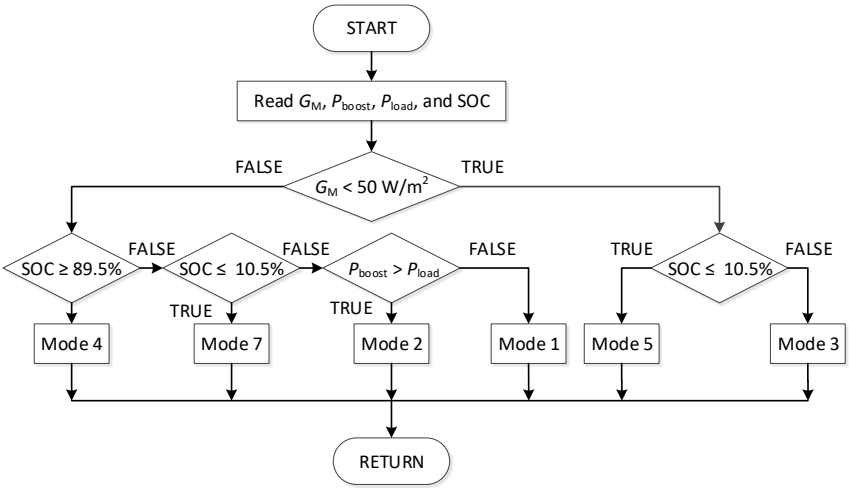

Figure 4.5: Power flow management for the off-grid case study

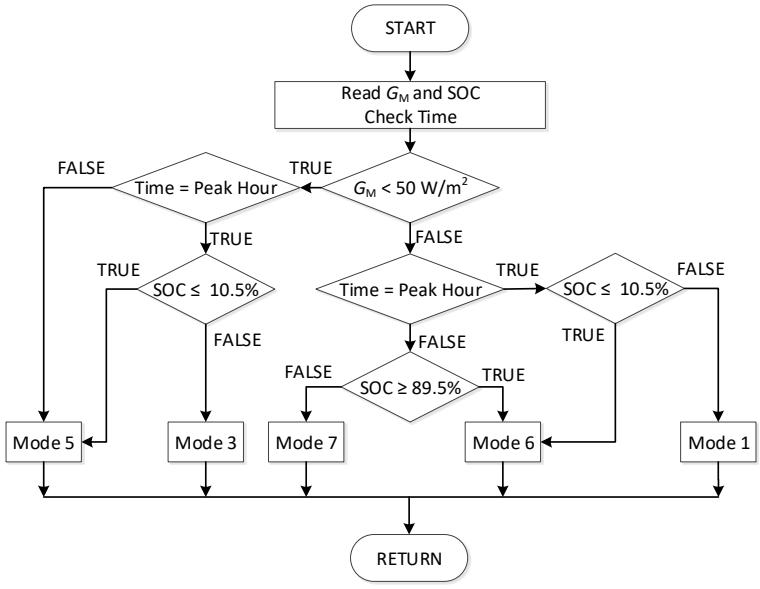

Figure 4.6: Power flow management for the peak-shaving case study.

- Mode 3

$$P_{\text{batt}}^{\text{out}} \cdot \eta_{\text{buck-boost}} \cdot \eta_{\text{inv}} + P_{\text{grid}} - P_{\text{load}} = 0. \tag{4.10}$$

- Mode 5

$$P_{\text{grid}} = P_{\text{load}}. \tag{4.11}$$

- Mode 6

$$P_{\text{boost}} \cdot \eta_{\text{inv}} + P_{\text{grid}} - P_{\text{load}} = 0. \tag{4.12}$$

- Mode 7

$$P_{\text{boost}} \cdot \eta_{\text{buck-boost}} - P_{\text{batt}}^{\text{in}} = 0. \tag{4.13}$$

Mode 3 is active during peak load times when the PV production is insufficient, and at the same time, the battery has remaining energy (SOC above lower limit). In that case, the battery is discharged to power the load; the grid can also partially supplied the load if required.

4.4.3. Constant load

This case is introduced to examine the ability of the *PBIM* to supply a load that consumes constant power by adjusting the PV generation and battery operation. The modes of operation established for the off-grid case study are applicable in this case study.

4.5. Model

The model consists of a PV power estimation model, a performance battery model, and an energy management controller that decides the power flow magnitudes and directions. These models receive as inputs meteorological data and load power consumption from the selected location, and based on that determines the power exchange, the voltage of the converters, and the battery bank SOC (refer to Figure 4.7).

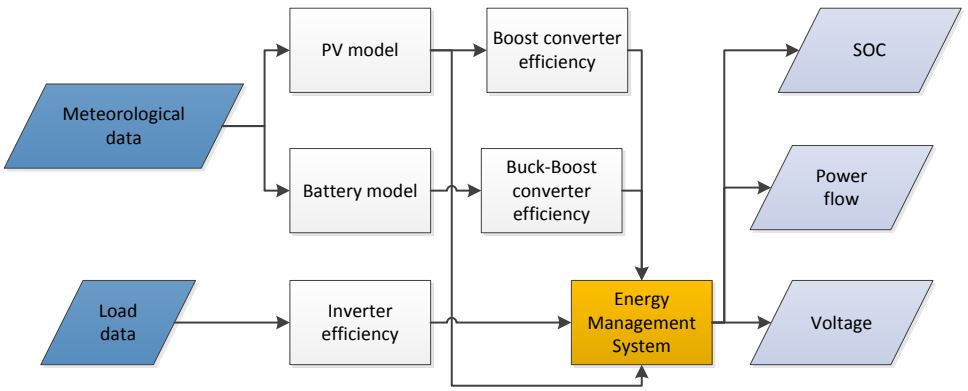

Figure 4.7: Overall model.

For estimating the PV production, a fluid dynamic model proposed previously was used [16]. In this model, irradiance, wind speed, and PV module geometry are required to estimate the PV panel temperature, which is later linked to the PV power production using a PV panel temperature coefficient. For modeling the battery behavior, a model that takes into account the particularities of battery technology by extracting key parameters from data sheets is used in the general model [17], which has been used

other solar system applications [18]. Also, the general model includes the losses expected in the conversion stages. To account for this factor, efficiency curves from known converter were taken into account, for the inverter [19], and for the converters [20].

A transient analysis was performed to study the dynamic response of the system in cases of abrupt changes in solar generation, refer to Appendix A. From the analysis, it can be noticed that the transient time (less than 0.1 s) is relatively shorter than the time step used for the power balance (one minute). Therefore, the transient transitions are not considered in this study.

4.5.1. Inputs

All the PV related data (irradiance, ambient temperature, and wind speed) were extracted from Meteonorm for both locations Cambodia (off-grid) and the Netherlands (peak-shaving).

For the off-grid case, environmental data from a rural area in Cambodia (Stung Treng) is used to obtain the PV power, and the data for the load is taken from a tier 2 case in a rural electrification study [21], both with one-minute time step.

In the case of the grid-connected case study, the typical load for a house in the Netherlands was selected including seasonal effects [22], while for environmental data (one minute time step), Delft was selected.

4.6. Results

4.6.1. Off-grid

Sizing

To size the system, the loss of load probability (LLP) was used to find the optimum battery capacity for a solar panel to power the tier 2 load selected (140 W, 18 V_{mpp}, 7.78 I_{mpp}). Because every pouch battery (20 Ah, 3.3 V) can deliver 65 Wh, the battery capacity is incremented from one cell to 20 cells in series in steps of 65 Wh.

Based on Figure 4.8, where the LLP is plotted as the battery size increases, LLP values reduce as the battery capacity increases; however, there is a point in which LLP continuous to lower but less drastically, and a further decrease on LLP is at the expense of extraordinarily high battery sizes. Therefore, the selected battery size was 390 Wh, for an LLP value of 1.53%. To have a battery size of 390 Wh, 6 batteries connected in series are needed.

Power balance

The power balance for a day with high and low irradiance are introduced in Figures 4.9a and 4.9b. Firstly, it is important to mention that the power of the battery is considered negative for charging and positive when discharging. Secondly, the initial SOC is set a 10% which means that neither the battery or solar panel are able to supply power to the load.

For the chosen day during the dry season, the *PBIM* operates in mode 5, but as soon as the sun rises the system changes briefly to mode 7, so the panel charges the battery (see Figures 4.9a and 4.9c). Later on, because of the vast solar generation at MPP, the battery can be charged and the load supplied at the same time (mode 2);

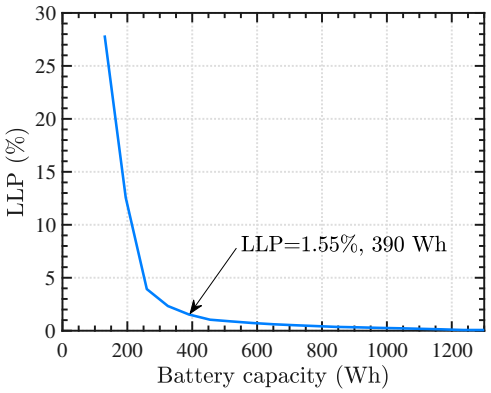

Figure 4.8: System sizing for the off-grid case study based on LLP.

however, after a while the solar generation is considerably higher than the load and the panel moves to a curtail operation, while the battery partially support the load. When the sun goes down, the device change to mode 3, which means that the power needed for the load is provided by the battery as long as there is enough energy remaining.

The three peaks observed between 12:00 and 16:00 are caused by low load consumption periods and excess of PV energy. Around 13:00, the battery (fully charged) is discharged from 90% to 85%, but as soon as the SOC decreases more, the PV panel operates at maximum power point again charging the battery and powering the load—first peak in battery and PV production. After some minutes, the battery is full again, and the same phenomenon occurs two more occasions for the dry season—two remaining peaks.

When comparing the selected days for the dry and rainy season, they are clear differences on the SOC level for both cases. As the generation is considerably less in the rainy season, as can be appreciated in Figure 4.9a and 4.9b. For the same reason, the mode of operation 4, where the PV generation is curtailed does not occur 4.9d. Also, mode 1 which was not present in the dry season, appears in the rainy season due to the inability of the PV panel to supply the load during the middle of the day needing the help of the battery.

PV and battery voltages

The changes in voltage for both PV and batteries for the dry and rainy season are illustrated in Figures 4.9e and 4.9f, respectively. Regarding the battery voltage, it can be noted that for the dry season the battery is charged until reaches the upper SOC limit and after some time is partially discharged, while for the rainy day due to the low PV generation the battery is charged and discharged several times. In the case of the PV voltage, it remains relatively constant throughout the day for the rainy season, while for the dry season the voltage dropped abruptly various occasions due to two reasons: the PV curtailment occurred more often, and mode 5 had to take place on various occasions as the load was zero and consequently the PV disconnected ($V_{\mathrm{PV}} = 0$).

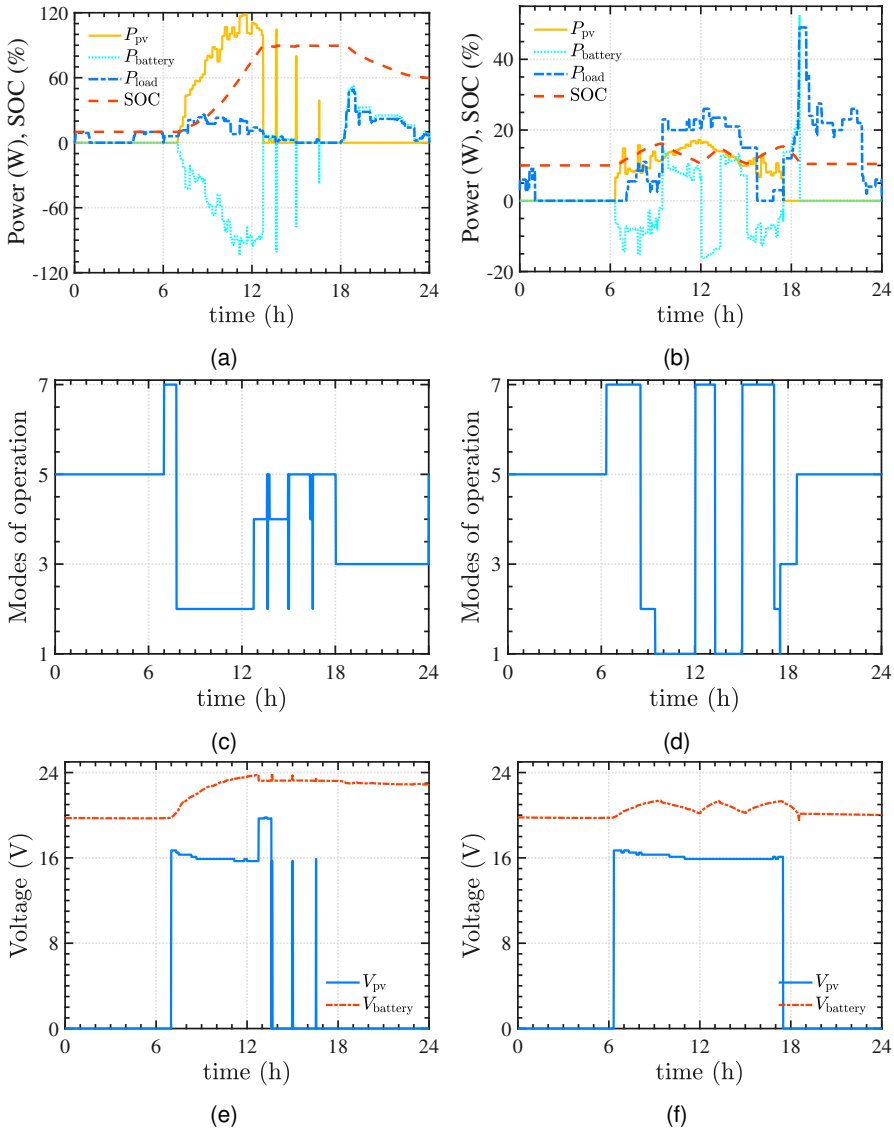

Figure 4.9: One day simulation for the dry and rainy season in a off-grid case study. (a) Power flows and SOC levels: dry season; (b) power flows and SOC levels for rainy season; (c) modes of operation for dry season; (d) modes of operation for rainy season; (e) PV and battery pack voltage for dry season; and (f) PV and battery pack voltage for rainy season.

4.6.2. Constant load

The objective of this section is to explore the ability of the *PBIM* to supply an individual appliance whose power consumption is relatively constant, as the *PBIM* might be useful for portable applications or as a backup in case of emergencies, where basic loads are

the priority.

Here, a *PBIM*, with the same PV and battery size as in Section 4.6.1, tries to deliver constant power to a 50 W load in an off-grid case study. As depicted in Figure 4.10, the integrated device powered the load successfully for about 14 hours even if the initial battery SOC was low. Because the battery was completely empty during the night, the *PBIM* was not able to satisfy the load demand, but soon in the morning time, the PV panel was enough to power the load and the remaining power was stored into the battery. In the afternoon, when the PV stated diminishing, the battery started supplying the load until the SOC reached its lower limit.

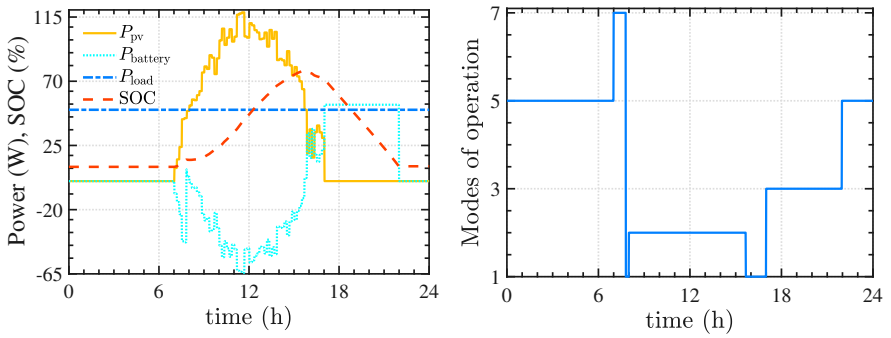

Figure 4.10: One day simulation for the constant load case study, (a) Power flows and (b) modes of operation for a constant load.

4.6.3. Peak-shaving

For this part of the study, a 265 W_p (31.44 V_{mpp}, 8.44 I_{mpp}) PV panel, a battery pack of 520 Wh (8 batteries in series), and a DC bus of 48 V are defined as the system characteristics. In this case study, the PV panel rating is increased compared to the previous case as well as the battery pack capacity. The energy consumed during the peak time in the Netherlands can be shaved by using a battery pack of 520 Wh. Also, the load can be partially supplied by the PV panel in off-peak times, ensuring not PV generation dumped (Figure 4.11).

Power balance

Before describing the power flow profiles, it is important to establish the peak consumption time, which in the Netherlands happens between 17:00 and 20:00 almost irrespectively of the season. Because the battery is initially empty during the night, at the beginning of the day the *PBIM* is in standby, as can be seen in Figure 4.11a. Therefore, the load is only supported by the grid. As a result, mode 5 represents the inactivity of the *PBIM* (Figure 4.11b). As soon as there is enough solar irradiation, the PV panel starts delivering power to the battery and changing to mode 7. A rapid fluctuation between mode 7 and mode 5 can also be seen in Figure 4.11b, because of low irradiance instances. Once the battery is completely charged, the solar panel is able

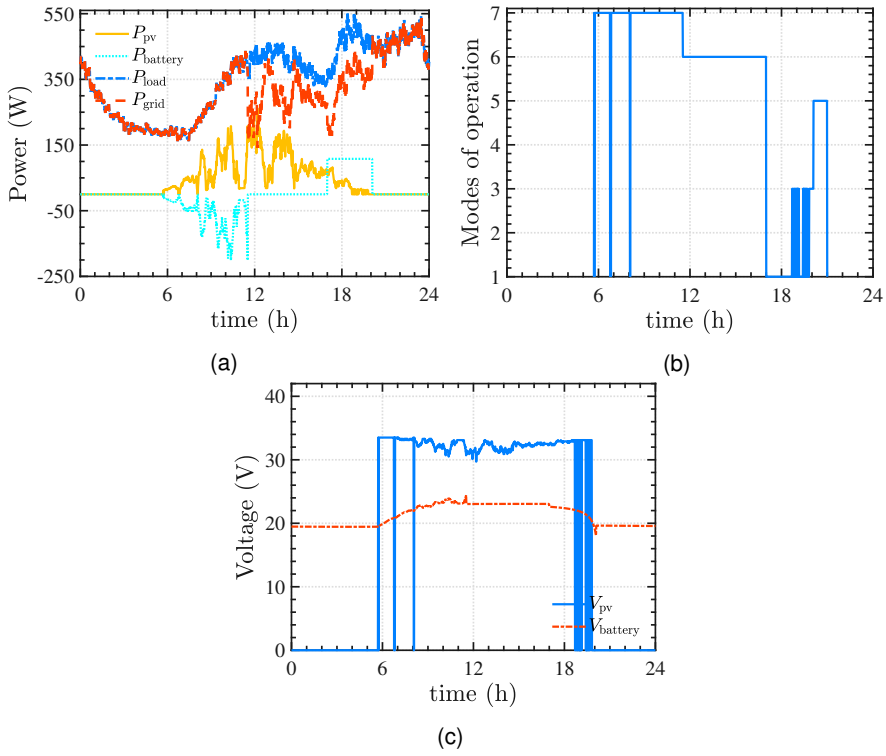

Figure 4.11: One day simulation for peak-shaving case study, (a) Power flow, (b) modes of operation, and (c) PV and battery pack voltage.

to supply the load partially, and the power extracted from the grid reduces (mode 6). Because the SOC of the battery reached the upper limit, the battery is disconnected to be later discharged during peak hours. At peak time, the diminished PV generation and the battery at constant power supply load. However, because the power required from the load is more than the *PBIM* combined production, power from the electricity grid is needed to complement the power from the *PBIM* as presented in mode 1. Again, the rapid changes between modes 1 and 3 are caused by the abrupt variations in incident irradiance on the solar panel.

PV and battery voltages

The solar panel and battery voltages are presented in Figure 4.11c. In this case, MPPT is always active when the PV produces power because PV power never surpasses the load required power. Regarding the battery voltage, the voltage does not vary when the battery completely charged and not used, but during peak times the voltage gradually decreases during peak hours as it is discharged. Figure 4.11c also shows that the PV panel voltage is zero in several occasions; this is because irradiance is below 50 W/m^2 during daylight, and in that condition the DC/DC boost converter is switched off.

4.7. Conclusions

This chapter focuses on controlling a *PV-battery Integrated Module* for performing energy management while paying attention to the system architecture. The most suitable architecture for the *PBIM* is the DC coupled. This decision is based on the number of conversion stages, battery safety, and converters control complexity. For this architecture, the control strategies needed to manage the converters are proposed. Seven modes of operation are presented to help the system define the most appropriate PV (MPPT, curtailment, or inactive) and battery operation (charging, discharging, or inactive), while the load is continuously changing. Based on this, three applications were explored: off-grid, constant load, and a peak shaving (grid-tied). For these cases, it was demonstrated that the *PBIM* can be managed to supply the load and regulate the power delivery.

Abbreviations

Table 4.3: Abbreviations used in the chapter.

Abbreviation	Description	Abbreviation	Description
SOC	State of charge	MPP	Maximum power point
ref	reference	batt	Battery
DC	direct current	AC	alternating current
SW	Converter switch	PI	Proportional integral

Nomenclature

The following nomenclature is used in this chapter:

Table 4.4: Nomenclature.

Variables	Description	Variables	Description
P_{PV}	PV power	V_{PV}	PV voltage
P_{boost}	power boost converter	$V_{\text{PV,mpp}}$	PV voltage at MPP
P_{load}	power demanded by the load	$V_{\text{PV,curtail}}$	PV voltage in curtail operation
$P_{\text{batt}}^{\text{out}}$	battery power discharged	$V_{\text{batt,nom}}$	battery nominal voltage
$P_{\text{boost,curtail}}$	battery power charged	V_{batt}	battery voltage
$P_{\text{batt}}^{\text{in}}$	power boost converter	V_{DC}	DC voltage
P_{fail}	power not provided to the load	$V_{\text{DC,ref}}$	DC voltage reference
P_{grid}	power required from the grid	I_{PV}	PV current
D_{boost}	boost converter duty cycle	$I_{\text{PV,mpp}}$	PV current at MPP
$D_{\text{buck-boost}}$	buck-boost converter duty cycle	$I_{\text{PV,ref}}$	PV current at reference level
η_{inv}	efficiency of DC/AC converter	$I_{\text{PV,curtail}}$	PV current in curtail operation
$\eta_{\text{buck-boost}}$	efficiency buck-boost converter	I_{batt}	PV current in curtail operation
e_1	PI error for PV voltage (boost converter)	$K_{\text{p,v}}$	controller gain parameter for $I_{\text{PV,ref}}$ and $I_{\text{batt,ref}}$
e_2	PI error for PV current (boost converter)	$K_{\text{i,v}}$	controller gain parameter for $I_{\text{PV,ref}}$ and $I_{\text{batt,ref}}$
e_3	PI error for PV voltage (buck-boost converter)	$K_{\text{p,i}}$	controller gain parameter for D_{boost} and $D_{\text{buck-boost}}$
e_4	PI error for PV current (buck-boost converter)	$K_{\text{i,v}}$	controller gain parameter for D_{boost} and $D_{\text{buck-boost}}$
C_{DC}	DC bus capacitance for buck-boost converter	C_{batt}	battery capacitance for buck-boost converter
$C_{\text{out,boost}}$	out capacitance for boost converter	$C_{\text{in,boost}}$	in capacitance for boost converter
L_{boost}	inductance for boost converter	$L_{\text{buck-boost}}$	inductance for buck-boost converter

References

[1] V. Vega-Garita, M. F. Sofyan, N. Narayan, L. Ramirez-Elizondo, and P. Bauer, *Energy management system for the photovoltaic battery-integrated module,* Energies **11** (2018), 10.3390/en11123371.

[2] R. Luthander, J. Widén, D. Nilsson, and J. Palm, *Photovoltaic self-consumption in buildings: A review,* Applied Energy **142**, 80 (2015).

[3] M. Bortolini, M. Gamberi, and A. Graziani, *Technical and economic design of photovoltaic and battery energy storage system,* Energy Conversion and Management **86**, 81 (2014).

[4] F. S. Sevilla, V. Knazkins, C. Park, and P. Korba, *Advanced control of energy storage systems for pv installation maximizing self-consumption,* IFAC-PapersOnLine **48**, 524 (2015), 9th IFAC Symposium on Control of Power and Energy Systems CPES 2015.

[5] Y. Riffonneau, S. Bacha, F. Barruel, and S. Ploix, *Optimal power flow management for grid connected pv systems with batteries,* IEEE Transactions on Sustainable Energy **2**, 309 (2011).

[6] C. Chin, A. Babu, and W. McBride, *Design, modeling and testing of a standalone single axis active solar tracker using matlab/simulink,* Renewable Energy **36**, 3075 (2011).

[7] W. Grzesiak, P. Mackow, T. Maj, A. Polak, E. Klugmann-Radziemska, S. Zawora, K. Drabczyk, S. Gulkowski, and P. Grzesiak, *Innovative system for energy collection and management integrated within a photovoltaic module,* Solar Energy **132**, 442 (2016).

[8] J. F. Reynaud, C. Alonso, P. Aloisi, C. Cabal, B. Estibals, G. Rigobert, G. Sarre, H. Rouault, D. Mourzagh, F. Mattera, and S. Genies, *Multifunctional module lithium-ion storage and photovoltaic conversion of solar energy,* in *Conference Record of the IEEE Photovoltaic Specialists Conference* (2008) pp. 1–5.

[9] J. F. Reynaud, O. Gantet, P. Aloïsi, B. Estibals, and C. Alonso, *New adaptive supervision unit to manage photovoltaic batteries,* IECON Proceedings (Industrial Electronics Conference) , 664 (2009).

[10] J. F. Reynaud, O. Gantet, P. Aloisi, B. Estibals, and C. Alonso, *A novel distributed photovoltaic power architecture using advanced Li-ion batteries,* Proceedings of EPE-PEMC 2010 - 14th International Power Electronics and Motion Control Conference , 6 (2010).

[11] A. A.-H. Hussein, S. Harb, N. Kutkut, J. Shen, and I. Batarseh, *Design considerations for distributed micro-storage systems in residential applications, Intelec 2010*, , 1 (2010).

[12] A. Mirzaei, M. Forooghi, A. A. Ghadimi, A. H. Abolmasoumi, and M. R. Riahi, *Design and construction of a charge controller for stand-alone PV/battery hybrid system by using a new control strategy and power management,* Solar Energy **149**, 132 (2017).

[13] X. Feng, M. Ouyang, X. Liu, L. Lu, Y. Xia, and X. He, *Thermal runaway mechanism of lithium ion battery for electric vehicles: A review,* Energy Storage Materials **10**, 246 (2018).

[14] V. Vega-Garita, L. Ramirez-Elizondo, G. R. C. Mouli, and P. Bauer, *Review of residential pv-storage architectures,* in *Proc. IEEE International Energy Conference (ENERGYCON)* (2016) pp. 85–94.

[15] R. I. Putri, S. Wibowo, and M. Rifai, *Maximum power point tracking for photovoltaic using incremental conductance method,* Energy Procedia **68**, 22 (2015), 2nd International Conference on Sustainable Energy Engineering and Application (ICSEEA) 2014 Sustainable Energy for Green Mobility.

[16] M. K. Fuentes, *A Simplified Thermal Model for Flat-Plate Photovoltaic Arrays*, Tech. Rep. (Sandia National Labs., Albuquerque, NM (USA), 1987).

[17] O. Tremblay, L. Dessaint, and A. Dekkiche, *A generic battery model for the dynamic simulation of hybrid electric vehicles,* in *2007 IEEE Vehicle Power and Propulsion Conference* (2007) pp. 284–289.

[18] V. Vega-Garita, D. D. Lucia, N. Narayan, L. Ramirez-Elizondo, and P. Bauer, *Pv-battery integrated module as a solution for off-grid applications in the developing world,* in *2018 IEEE International Energy Conference (ENERGYCON)* (2018) pp. 1–6.

[19] ABB, *Abb micro inverter system micro-0.25-i-outd,* (2015).

[20] G. R. Walker and P. C. Sernia, *Cascaded DC-DC converter connection of photovoltaic modules,* IEEE Transactions on Power Electronics (2004).

[21] N. Narayan, Z. Qin, J. Popovic-Gerber, J.-C. Diehl, P. Bauer, and M. Zeman, *Stochastic load profile construction for the multi-tier framework for household electricity access using off-grid dc appliances,* Energy Efficiency (2018), 10.1007/s12053-018-9725-6.

[22] B. Asare-Bediako, W. L. Kling, and P. F. Ribeiro, *Future residential load profiles: Scenario-based analysis of high penetration of heavy loads and distributed generation,* Energy and Buildings **75**, 228 (2014).

5

Thermal Management

In this chapter, a representative finite element method (FEM) model is set to describe the thermal behavior of the *PBIM*, and especially to quantify the adverse effect of placing the battery pack and power electronics components at the back of the PV panel. From the simulations, it is determined that the temperature of the components increases to a level that it might compromise their safe operation. As a consequence, two thermal management methods are explored: air gap and phase change materials. This chapter proves that batteries operate in a safe range when an air gap is added between the PV panel and the BoS components (battery pack and power electronics), as the temperature of the components is reduced drastically. An additional diminution in battery temperature is achieved by using phase change materials. At the beginning of the chapter, the FEM model is described, and the inputs introduced. The next sections deal with the effect of attaching, or not attaching, the components to the PV panel. As a follow-up, the optimum air gap thickness is found, as well as the influence of using phase change materials. The results of this chapter are fundamental to determine the suitable battery technology, which is studied in chapter 6.

This chapter is based on V. Vega-Garita, L. Ramirez-Elizondo, and P. Bauer. *Physical Integration of a Photovoltaic-battery System: a Thermal Analysis*, Applied Energy (2017) [1].

5.1. Introduction

Although some steps to integrate normal size PV panels and balance-of-system components (converters and batteries) have been reported [2, 3], just a few papers have coupled batteries directly with solar panels in one device. A combination of PV panel, battery, and electronic control unit was initially suggested in [4], stating the different advantages, general restrictions, and operational conditions of the so-called *multifunctional module*. Following this, the battery management system was proposed [5], and later, this concept was designed to supply bigger loads. The construction, control, and testing of the prototype were presented in [6]. Moreover, the details of the construction and installation of an integrated module for portable applications were published in [7].

However, little attention have been paid to the thermal implications derived from the physical integration (PI), as this chapter aims. A vast amount of previous papers have investigated the thermal behavior of PV panel and batteries operating individually [8, 9], finding that thermal management systems are necessary to decrease the impact on efficiency and safety [10]. Most of the active cooling solutions (e.g. air or liquid forced convection systems, heat pipe, thermoelectric devices, and cold pipe) are complex to implement and maintain, and therefore costly [11]. Additionally, active cooling consumes a portion of the power generated by the PV panels, decreasing the total efficiency of the system. Instead, phase change materials (PCM) have demonstrated to be a promising option as a passive thermal management system for PV panels and batteries [12]. In comparison to active cooling systems for batteries, PCM achieve higher temperature uniformity [13], prevent temperature peaks [14], provide temperature regulation [15], and keep battery operating under safe temperature thresholds [16]. These are the reasons behind the use of PCM in this study.

5.1.1. Contribution

While some researchers have developed similar ideas to integrate a PV-battery system in one device, there are still several gaps to fill regarding the feasibility of the PI concept. In particular, a thorough understanding of the thermal processes that take place when integrating all the components together, and their implications to the battery pack. This chapter contributes towards

- building (section 5.3) and validate (section 5.5) a thermal model for the *PBIM* using the Finite Element Method (FEM),
- understanding the effect of directly attaching the components to the PV panel (section 5.4.1) or including an air gap between them (section 5.4.2),
- estimating the maximum battery temperatures and PV temperatures reached under extreme conditions (section 5.4.3),
- evaluating the effectiveness of including a phase change material as thermal management method (section 5.4.4), and
- proving that, in the short term, batteries are expected to operate in a safe temperature range even under high ambient temperature and insolation, and the *PBIM* is technically feasible for solar energy applications (section 5.4.3).

5.2. Physical Design

For an optimal design of the *PBIM*, the following criteria must be satisfied:

- Heat has to be dissipated efficiently to avoid overheating.
- The *PBIM* must prevent the entrance of dust and water from the environment.
- A frame must hold the components to ensure they do not move when installing and operating.
- Total volume and weight of the *PBIM* should be reduced as much as possible.

Given the requirements, pouch cells or prismatic cells are preferred due to their thin profile; they help to achieve high packaging as well as notable storage energy capacity per unit of volume. This sort of cells also provides a more extended surface allowing better heat dissipation than other geometries. Therefore, for the modelling, fifteen $LiFePO_4$ cells (A123 AMP20) are used to store the energy coming from the PV panel (265 W_p from Jinko Solar). The PV panel was chosen after comparing several options, based on efficiency, weight, cost, and temperature coefficients as reported in [17].

Due to the fact that the integration concept is relatively new, the size of the components and other features are assumed similar to the commercial charge controllers and microinverters.

5.3. Finite Element Method Model

A thermal model able to include the heat generated and dissipated to the surroundings for a particular 3D and 2D geometry is complex to be developed from the beginning. As a consequence, an interface developed by COMSOL Multiphysics ® is selected. This interface (conjugate heat transfer) interrelates and solves the differential equations that describe the heat transfer and the fluid flow mechanisms.

A 3D model is used in section 5.4.1 and section 5.4.2, while in section 5.4.3 and section 5.4.4 a 2D model was developed to reduce computation time. The 2D geometry had 52203 elements, with 7420 boundary elements and average element quality of 0.85 for a triangular mesh. On the other hand, the quality of the elements was 0.7 for the 203110 tetrahedral elements, from which 40382 were at the boundaries. The element quality is related to metrics such as volume versus length ratio, volume versus circumradius relationship, where 1 is assigned to an optimal element and 0 to a degenerated element (lowest quality element).

5.3.1. Basic geometry

Figure 5.1a presents a 2D layout of the integrated module, including the materials and layers of the proposed design. The features of the components are detailed in Tables 5.3 and 5.2, including the parameters and subscripts used in the equations.

5.3.2. Governing equations

Heat transfer in solids

The heat that is transferred by conduction is given by the diffusion equation as follows:

$$\nabla \cdot (k\nabla T) + \dot{q} = \rho c_p \frac{\partial T}{\partial t}, \tag{5.1}$$

where k is the thermal conductivity, T temperature vector, $\dot{q}$ heat generation, ρ density, c_p specific heat, and t time.

Equation (5.1) is applied to the layers that compound the PV panel, the batteries, the charge controller, the microinverter, and the frame.

Heat transfer in fluids

Heat transfer in fluids occurs in the air domain, where it is defined as

$$\nabla \cdot (k\nabla T) + \dot{q} = \rho c_p \frac{\partial T}{\partial t} + \rho c_p (u \cdot \nabla T), \tag{5.2}$$

where u is the velocity of the fluid in all directions (x,y,z). In equation (5.2), the work produced by the pressure when the density is temperature dependent is neglected.

Fluid dynamics

The equations for momentum balance and continuity are used to model the fluid behavior in the air domain, in order to obtain the velocity and pressure field. They are

$$\mu \nabla^2 u - \nabla p + F = \rho (u \cdot \nabla T) + \rho \frac{\partial u}{\partial t}, \tag{5.3}$$

$$\nabla \cdot u = 0, \tag{5.4}$$

where μ stands for viscosity, p for pressure in all directions, and F for fluid force. In the case of natural convection, the buoyant force produced by the fluid helps the heat dissipation. This force is calculated following equation (5.5), where a change in the density (ρ) of the fluid with respect to a reference point (ρ_{ref}) drives the phenomenon:

$$F = g(\rho - \rho_{\mathrm{ref}}). \tag{5.5}$$

5.3.3. Coupling of physics

Equations (5.2) and (5.3) are completely coupled since both equations include the velocity term u. Moreover, properties like density and viscosity of the air are a function of pressure and temperature. Therefore, these two variables connect the heat transfer and fluid dynamics physics in a deeper manner.

5.3.4. Heat generation

The heat generated is assumed uniform for a given volume (3D model) or surface (2D model). In particular, this condition is applied to the following domains: battery, silicon layer, and glass domain layer.

PV panel

The irradiance (G) affects the glass layer and the silicon layer. The incident light is partially reflected (R) at the glass surface (see Figure 5.1b); then a portion of the remaining irradiance is absorbed by the glass (A_{glass}). All the irradiance from the glass is transmitted (A_{cell}) to the Si layer, where it is completely converted into heat, except the portion that produces electricity (η_{PV}). It is assumed that the eva layer and the tedlar layer do not interact with the incident light; hence, the heat generated in these layers is omitted.

The contribution of the heat generated in the glass layer and Si layer is calculated using the following:

$$\dot{q}_{\text{glass}} = \frac{G(1-R)A_{\text{glass}}}{t_{\text{glass}}}, \tag{5.6}$$

$$\dot{q}_{\text{Si}} = \frac{G(1-R)(1-A_{\text{glass}})(1-\eta_{\text{PV}})}{t_{\text{Si}}}. \tag{5.7}$$

Batteries

As part of the losses in the batteries, the heat generation equation accounts for the reversible and irreversible heat generation resulting from the charging and discharging processes. This heat can be calculated by using the following expression:

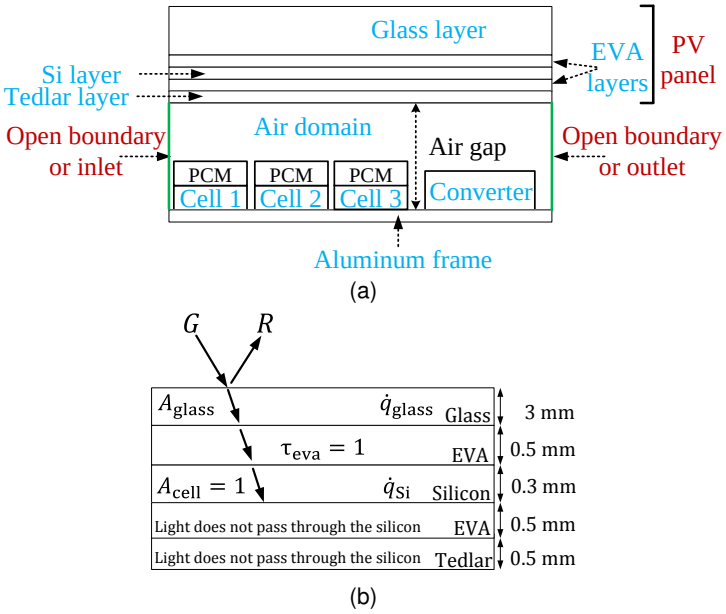

Figure 5.1: (a) 2D layout of the integration concept, and (b) light interaction within the PV panel layers.

$$\dot{q}_{\text{battery}} = \frac{I}{V_{\text{battery}}}\left(V - V_{\text{OC}} + T\frac{\partial V_{\text{OC}}}{\partial T}\right). \tag{5.8}$$

where I is the charging or discharging current. The voltage (V) curve, open circuit voltage (V_{OC}) curve, and entropy coefficient ($\frac{\partial V_{\text{OC}}}{\partial T}$) are used according to the data provided by the manufacturer [18].

Converters

For the heat generating terms of the converters, the general approach is described by equation (5.9), where the instantaneous efficiency ($\eta_{\text{converter}}$) is taken from a look-up table that correlates power input (P_{in}) and power output, while $V_{\text{converter}}$ is the total volume of the converter:

$$\dot{q}_{\text{converter}} = \frac{P_{\text{in}}}{V_{\text{converter}}}(1 - \eta_{\text{converter}}). \tag{5.9}$$

It is assumed that all the losses of the converters are dissipated as heat following the previous equation.

5.3.5. Boundary conditions

The predominance of either forced convection or natural convection results in different temperature values for the components. Therefore, different boundary conditions were applied to the FEM model to evaluate their influence.

Whereas for forced convection air enters (inlet) with a certain velocity at the left and leaves (outlet) at the right (Figure 5.1a), for natural convection right and left boundaries are considered open -the air can enter or leave the domain.

Convection

Convection is used to include the effect of the surrounding air on the surfaces exposed to it. The heat transferred via convection was applied at the top of glass layer, and the bottom and sides of aluminum frame as follows:

$$q_{\text{conv}} = h(T_{\text{s}} - T_{\text{amb}}), \tag{5.10}$$

where T_{s} is the temperature of the boundary, T_{amb} ambient temperature, and h convection coefficient.

Radiation

The heat in form of radiation coming out of the top of the PV panel and the bottom of the aluminum frame is associated with the temperature of the body (T_{s}) and the temperature of the surroundings (T_{amb}):

$$q_{\text{rad}} = \sigma\varepsilon(T_{\text{s}}^4 - T_{\text{amb}}^4). \tag{5.11}$$

5.3.6. Inputs

Three days with the highest global horizontal irradiation (Figure 5.2a), lowest wind velocity (Figure 5.2b), and maximum ambient temperature (Figure 5.2c) were chosen as inputs to the FEM model in sections 5.4.3 and 5.4.4. Although it is very uncommon that the warmest day, least windy day, and the day with the highest irradiation coincide on the same day, this extreme scenario is defined as the most severe condition that the integrated device must handle due to high risk of components overheating. The data was taken from the Dutch Meteorological Institute (KMNI) at the Cesar Observatory (51.971°N, 4.927°E) throughout the year 2014, with a time resolution of 10 min.

Intermediate inputs

The battery system is driven by a simple control, where battery charging is a priority. The battery is charged according to the current produced by the PV panel which continuously varies, although it never surpasses 0.5 C-rate. After the sun stops shining and the battery is full, it is discharged at 0.25 C-rate (see Figure 5.2d). The limits for charging are 90% state of charge (SOC) and 10% SOC when discharging, in order to protect the battery from overcharging or over-discharging, respectively. As can be seen in Figure 5.2e, the heat generated during the charging process is negative, because of the undergoing endothermic process. Nevertheless, the battery pack releases heat to the surroundings when discharging.

The heat created inside the converters follows the pattern dictated by the solar irradiation. It is assumed that volume of the DC/DC converter and microinverter are equal, but the moments at which the components act differ: the DC/DC converter is on during charging, while the microinverter is active when discharging.

5.4. Results

5.4.1. Directly attached (DA) or not?

To achieve a *PBIM* as compact as possible, attaching the components directly on the back side of the PV panel is the most integrated option. To evaluate this idea and compare it to the non-attached (NA) case, the steady state model incorporates the parameters in Table 5.1. The incoming irradiance (G) was defined as a high value of irradiation, while $\dot{q}_{\text{battery}}$ is the highest that can be generated at 1 C-rate when discharging. $\dot{q}_{\text{converter}}$ is calculated at the PV power production peak, whereas T_{amb} and h are considered appropriate in relation to the defined irradiance value. Moreover, forced convection is applied as shown in Figure 5.1a varying the wind speed from 1 ms^{-1} up to 9 ms^{-1}, in order to understand its influence on the average temperatures of the devices.

Table 5.1: Parameters used for the steady state simulation.

Parameters	Value	Parameters	Value
G	1050 Wm^{-2}	$\dot{q}_{\text{converter}}$	4500 Wm^{-3}
T_{amb}	35°C	h_{top}	6 $\text{Wm}^{-2}\text{K}^{-1}$
$\dot{q}_{\text{battery}}$	10000 Wm^{-3}	h_{bottom}	6 $\text{Wm}^{-2}\text{K}^{-1}$

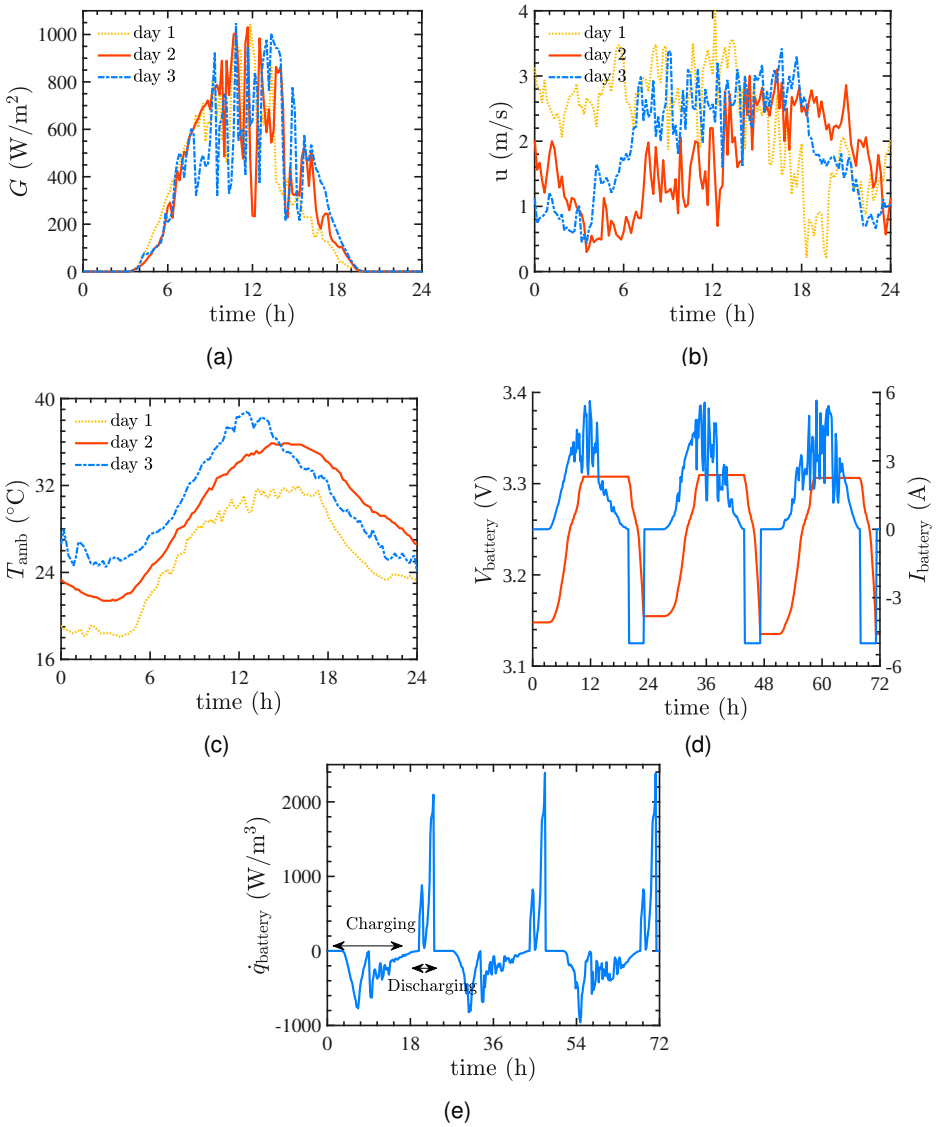

Figure 5.2: Inputs to the FEM model for three days with the (a) highest GHI, (b) lowest wind speed, (c) maximum ambient temperature, (d) cell voltage and current, and (e) heat generation in one cell.

The heat distribution in Figure 5.3 shows that, for both NA and DA, the highest temperature is reached in the PV panel domain, due to the massive heat generated in the cell layer compared to the other heat sources. As a result, the temperature of the battery pack and converter are similar to the temperature of the PV panel for the DA case (see Figure 5.3a and 5.3b).

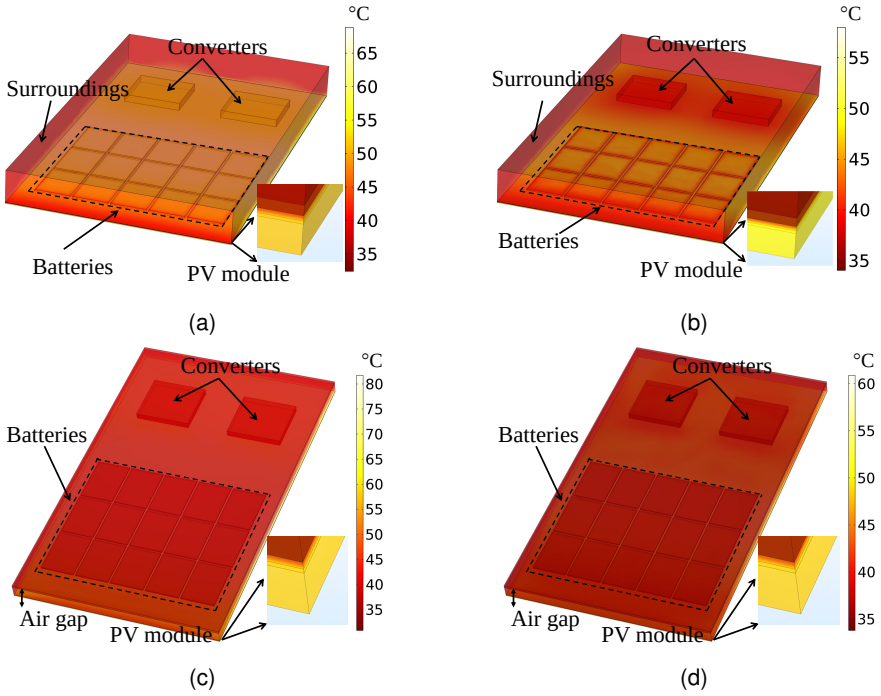

Figure 5.3: Temperature distribution obtained from the FEM model: (a) directly attached and air velocity of 1 ms^{-1}, (b) directly attached and air velocity of 8 ms^{-1}, (c) air gap (50 mm) and air velocity of 1 ms^{-1}, (d) air gap (50 mm) and air velocity of 8 ms^{-1}. Note: in all the figures, the PV panel is facing down.

An increase in wind speed reduces the temperature of the components (Figure 5.4a), while glass temperature is almost equal to the cell layer because of their proximity. In addition, the cooling effect of air is more pronounced on the converters than on the batteries, as the more extended area of the converter provides better heat dissipation.

By adding an air gap in between the PV panel and the components, the temperature of all components decreases considerably, since the air gap hinders the heat transfer from the PV panel to the other elements. Although increasing the wind speed helps remove heat from the components more efficiently when velocity increases, Figure 5.4b also shows that at some point a further increase in wind velocity does not reduce the temperature of batteries and converters.

In the NA case, battery pack temperature depends on air speed, but mainly on the ambient temperature if the air gap is kept constant. Because according to Figure 5.4c, the temperature of the battery increases with ambient temperature, 3°C in this case.

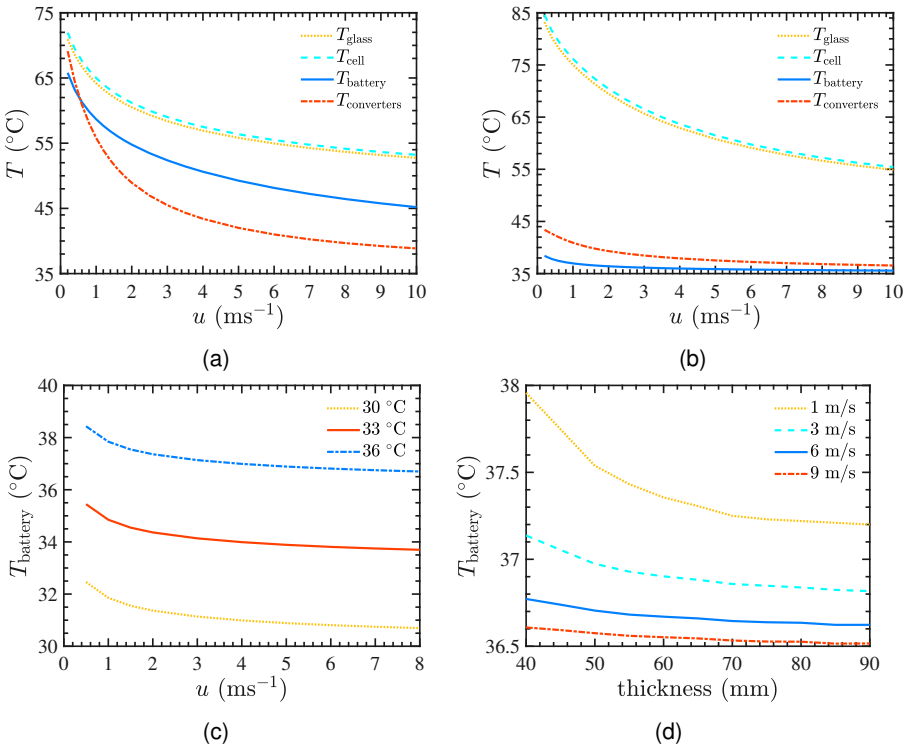

Figure 5.4: Temperature obtained from the FEM model: (a) components when directly attached, (b) components when not attached (air gap of 50 mm), (c) battery at different ambient temperatures (30°C, 33°C, and 36°C) for an air gap of 50 mm, and (d) battery for various air gaps and air velocities.

5.4.2. Air gap

The air gap is the distance between the PV panel and the frame (see Figure 5.1a), which is represented in the FEM model as the volume for the 3D model (or area for the 2D model) of the air domain. By increasing this domain, the temperature of the batteries drops as can be observed in Figure 5.4d. The diminution on battery temperature results from having more space between the battery pack and the PV panel — the main heat generation source. Also, in Figure 5.4d, it can be observed that low air velocities causes higher temperature compared to the case with an air velocity of 9 m/s, where the temperature value for all the air gaps is the minimum.

Taking as a reference the case with the lowest air speed (1 m/s) and highest battery temperature —which is closer to the expected ventilation condition in the *PBIM*— it can be seen in Figure 5.4d that the reduction on battery temperature is more pronounced at the beginning (40 mm) and further increments do not represent a considerable decline in battery temperature. After 70 mm, a raise in distance (air gap) does not significantly reduce the temperature of the battery, but it may rather augment the volume/weight ratio of the *PBIM*, which should be kept as low as possible. As a consequence, it suggested

that an air gap between 5–7 cm is enough to maintain the batteries operating at an appropriate temperature.

5.4.3. Natural and forced convection

In this section, the data described in Section 5.3.6 is employed by a transient model to incorporate the effect of the environmental conditions that the *PBIM* could face in an extreme scenario.

As expected, the temperature of PV cells rises with poor cooling conditions. With natural convection as a dominant phenomenon, the temperatures can increase 10°C more than in the case where forced convection is the primary cooling mechanism (see Figure 5.5a). In this figure, the benchmark dictates the minimum temperatures for a PV panel without any device attached.

Battery temperature does not differ significantly when either under forced convection or natural convection as the dominant mechanism, as Figure 5.5b suggests. However, a minor reduction is observed for the forced convection case.

Batteries operate within a safe range, because even under harsh conditions the

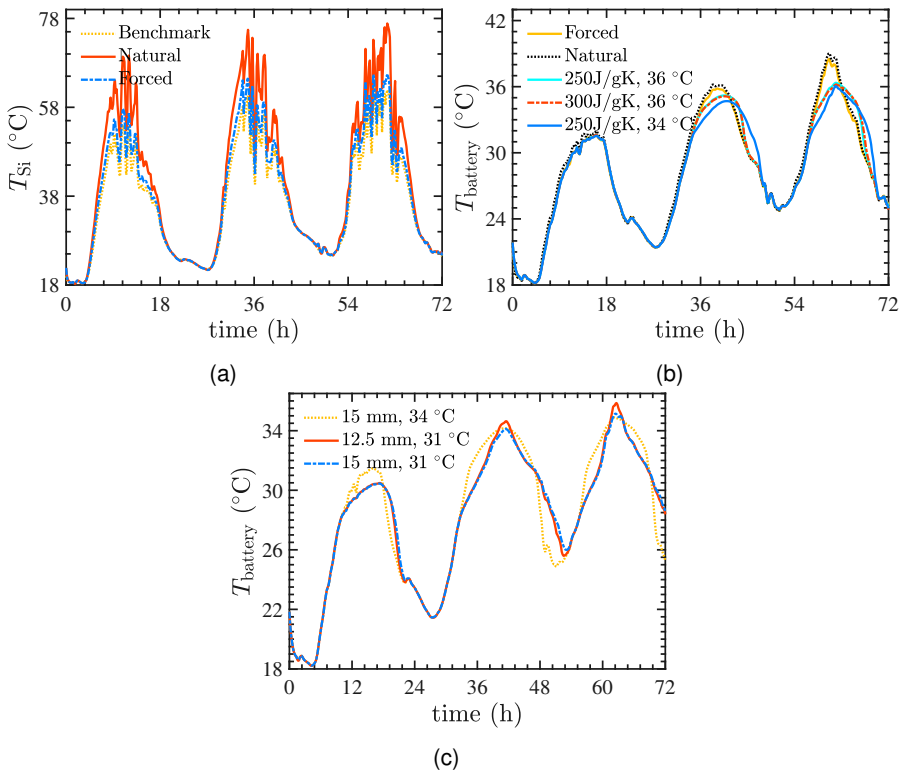

Figure 5.5: (a) Average Si layer temperature for natural and forced convection (50 mm air gap), (b) average battery temperature for forced convection, natural convection, and different PCM (5 mm thick), and (c) average battery temperature for various PCM thickness and PC temperatures.

battery temperature never surpasses 39°C (third day for natural convection conditions), which is under the defined maximum temperature of operation: 55°C ([18]). Due the air gap, the temperature of the batteries can be minimized till the minimum (ambient temperature).

According to Figures 5.5a and 5.5b, the temperature of the batteries and PV cell do not follow the same pattern. PV cell temperature responds mainly to irradiance and ambient temperature, while batteries respond to ambient temperature. The effect of ambient temperature on battery temperature is more important, even if the battery discharges at a relatively high C-rate (0.5 C), as the amount of heat produced by the battery is overshadowed by the heat coming from the surroundings. Of course, this applies as long as the batteries are neither overcharged nor over-discharged

5.4.4. Phase change materials

Even though it has been demonstrated that batteries do not surpass the upper temperature limit defined by the manufacturer, the operating temperature must be kept as low as possible to prevent accelerated battery aging and thermal runway [19, 20]. PCM are proposed as a passive cooling method, since forced convection is unable to diminish the temperature of the batteries significantly. PCM materials store thermal energy not allowing battery temperature to increase fast; they also maintain T_{battery} under a specific value as long as PCM does not saturate.

To study the effect of PCM over T_{battery} a layer of PCM is placed at the top of batteries (Figure 5.1a). The PCM used has a thickness of 5 mm, a density of 900 kg/m^3, a thermal conductivity of 5 $\text{Wm}^{-1}\text{K}^{-1}$, a phase change temperature range (ΔT) of 6 °C, and a heat capacity of 1.9 $\text{Jg}^{-1}\text{K}^{-1}$ when solid and 2.3 $\text{Jg}^{-1}\text{K}^{-1}$ when liquid. Only the latent heat (L), phase change temperature (T_{PC}), and thickness are modified to perform a parametric analysis later on.

As can be seen in Figure 5.5b, a PCM with a phase change (PC) temperature of 36°C and L of 250 Jg^{-1} shaves the third-day temperature peak by 3°C, and to a smaller extent the second-day peak. In case the latent heat increases from 250 Jg^{-1} to 300 Jg^{-1}, for a T_{PC} of 36°C, the temperature of the batteries does not drop because the phase changing process starts later. Also in Figure 5.5b, the results show that T_{battery} reduces for a T_{PC} of 34°C and L of 250 Jg^{-1}, where the second peak and third peak are shaved better. This is explained since the PC process starts at around 30°C and finishes near 36°C, the reduction of battery temperature intensifies because more heat it is absorbed than in the other cases.

To reduce T_{battery} even further, either PCM thickness or L might be increased, both for lower T_{PC}. However, a L of 250 Jg^{-1} is already high for the existing PCM technology. Hence, just the thickness varies as follows.

The effect of increasing the thickness for two phase change temperatures is illustrated in Figure 5.5c, indicating that a PCM with a T_{PC} of 31°C and 12.5 mm thick is able to shave all the three peaks, although as expected, 15 mm thick PCM has better results for the second and third peaks. However, a PCM with a T_{PC} of 34°C and a thickness of 15 mm is not capable of shaving the first peak, which indicates that this combination is not a candidate for the final design of the *PBIM*. Finally, a 15 mm PCM with a T_{PC} of 31°C is the overall best option. Due to its performance at elevated temperatures, but

also when temperatures are not extremely high; which is usually the case for the *PBIM* on a daily basis.

It is important to mention that although PCMs can help reducing battery temperature, it might result in a solution difficult to implement. When considering that the maximum reduction on battery temperature is 5°C under extreme conditions, which are not likely to occur several times during a year, the benefits of thermal management through PCM are limited. Therefore, the added cost of a PCM system might not compensate for the extra cost of adding PCMs, while the complexity of the system increases.

5.5. Validation of the FEM Model

A prototype was built and tested to validate the FEM model. The validation was carried out comparing the outcomes of the model and experimental measurements, using the same initial and boundary conditions. The testing set up, the characteristics of the prototype, and the results of the comparison are described as follows.

5.5.1. Testing set-up

A 30 W_p PV panel from Blue Solar was connected to a Genasun GV-5-Li-14.2V charge controller which performs maximum power point tracking. The charge controller imposes a constant current and constant voltage profile during the battery charging process. Moreover, four batteries with a capacity of 8 Ah and a nominal voltage of 3.2 V (WN08AH) were connected to the charge controller and a 10 Ω load (See Figure 5.6a). Before testing, two thermocouples were attached to the top and back side of a selected battery, while another thermocouple was placed at the upper part of the PV panel. All temperature measurements were taken with a time resolution of 5 min.

After connecting all the components and measuring devices, the prototype was placed under a small solar simulator (0.6 x 0.5 m) that produces a constant radiation of 900 Wm^{-2}, while the ambient temperature was around 25 °C during the test. Figure 5.6c and 5.6b show the spatial arrangement of the components and the prototype under testing, respectively.

At the beginning of the test, the batteries are partially charged (90% SOC), and as the test continues they are charged at a constant current of 1.65 A.

5.5.2. Results

After one hour of testing, the temperature of the batteries reached steady state condition, as can be observed in Figure 5.6d. The measured temperature at the bottom and top of batteries corresponds to the values predicted by the FEM model. The temperature of the PV panel increased up to 70°C, as expected in the FEM model and the IR image in Figure 5.6e. The thermal equilibrium for the PV panel is reached after 40 minutes, considerably lower than that for the batteries. This mismatch occurs, first, because the heat from the PV panel is conducted to the aluminum frame and then to the batteries, taking some time to be transferred. Secondly, because the air where the components were placed is heated up gradually, creating an equilibrium temperature more slowly compared to the PV panel. Future research must be done to understand the impact of elevated temperatures in the performance of the integrated module, in

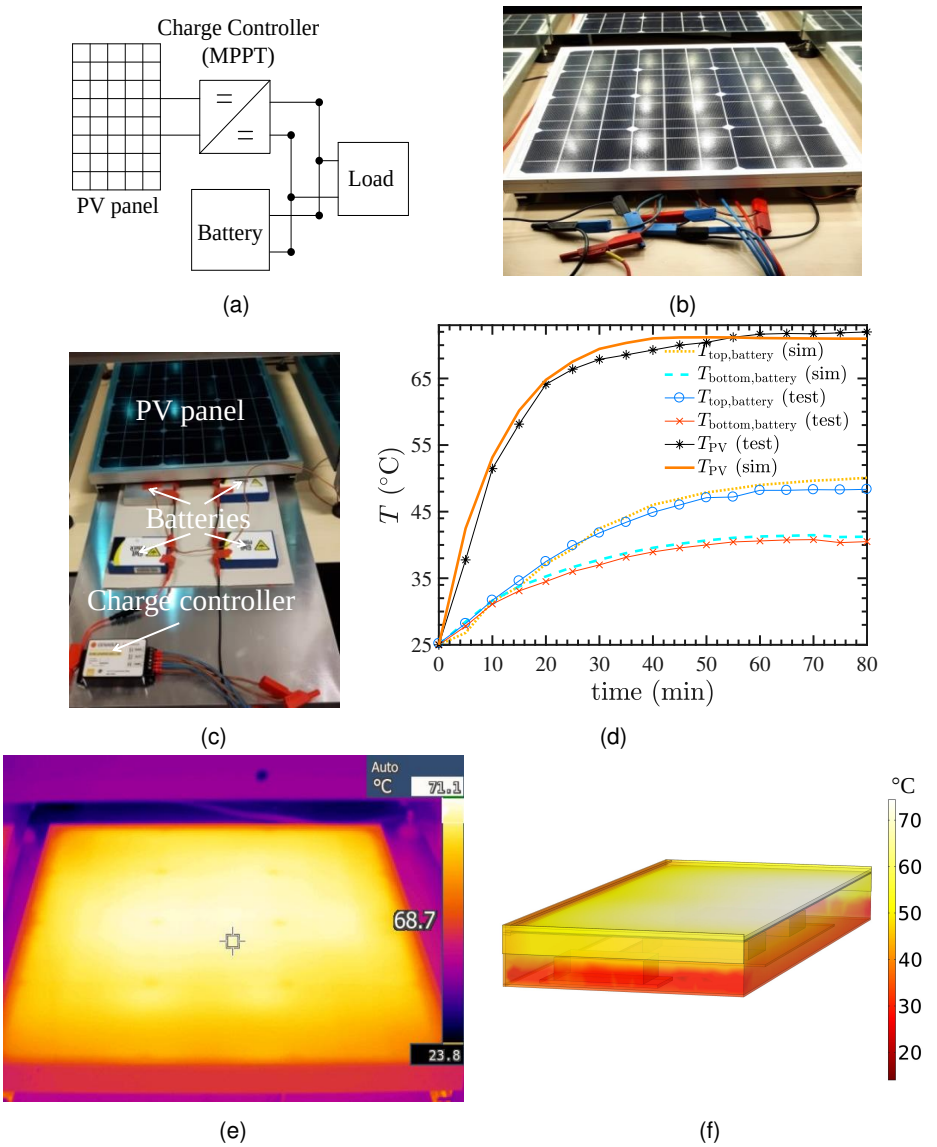

Figure 5.6: Characteristics of the prototype for FEM validation, (a) electric diagram of the prototype, (b) prototype under testing, (c) components of the prototype, (d) temperature of the components according to simulation (sim) and lab measurements (test), (e) temperature distribution at the top of the PV panel instants before finishing the test (IR image), and (f) simulation results of FEM model.

order to understand, for instance, how aging decreases battery lifetime and state of health.

5.6. Conclusion

A FEM model was developed and validated testing a prototype to study the thermal behavior of the *PV-Battery Integrated Module*. The model shows that directly attaching the components at the back of the solar panel results in extreme temperatures for the battery pack, suggesting the necessity of an air gap between them. The air gap help reducing the temperature of the components, impeding the heat generated at the PV panel from warming the batteries and converters. The optimal air gap is between 5-7 cm, in order to provide an appropriate packaging/cooling ratio. Even under severe conditions, maximum battery temperature never surpassed 39°C when including an air gap. This temperature is lower than the maximum temperature of operation defined by the manufacturer. However, because convection has a limited effect in decreasing the temperature of the components, phase change materials were proposed as a passive cooling method able to reduce the maximum battery temperature by 5°C. Phase change materials prove to be useful for shaving battery temperature peaks but it is perceived as difficult to implement in the integrated device in comparison to adding a simple air gap. In summary, the battery pack operates in a safe range, confirming the feasibility of the *PBIM* concept from the thermal analysis point of view, as a future solution for solar-battery systems. Moreover, this chapter helped defining the characteristics of a *PBIM* prototype, which will be studied in more detail in the next chapter 6.

Table 5.2: Subscripts used in the FEM model

Subscripts	***Description***
glass	property at glass layer
Si	property at Silicon layer
PV	PV panel
battery	property at batteries
OC	open circuit
converter	property at converter
in	input
s	surface
amb	ambient
rad	radiation
conv	convection
ref	at reference point

Table 5.3: Parameters used in the FEM model

Constants	*Description*	*Value*
P_{rated}	rated power of PV panel	265 W_p
T_{NOCT}	PV panel NOCT temperature	45°C
L_{PV}	PV panel length	1.65 m
W_{PV}	PV panel width	1 m
$V_{\text{OC,PV}}$	open circuit voltage PV panel	38.6 V
V_{mpp}	maximum power point voltage PV panel	31.4 V
I_{SC}	short circuit current PV panel	9.03 A
I_{mpp}	maximum power point current PV panel	8.44 A
V_{coeff}	voltage temperature coefficient PV panel	-0.31% K^{-1}
I_{coeff}	current temperature coefficient PV panel	0.06% K^{-1}
W_{PV}	weight PV panel	19 kg
C	battery capacity	19.5 Ah
T_{storage}	battery storage temperature	-40 to 60°C
V_{rated}	battery voltage rating	3.2 V
T_{op}	battery operation temperature	-40 to 60°C
L_{battery}	battery length	22.7 cm
W_{battery}	battery width	16 cm
t_{battery}	battery thickness	0.725 cm
$L_{\text{converter}}$	converter length	24.6 cm
$W_{\text{converter}}$	converter width	26.6 cm
$t_{\text{converter}}$	converter thickness	2.7 cm
t_{frame}	frame thickness	2 mm
k_{glass}	thermal conductivity of glass	1.38 $\text{Wm}^{-1}\text{K}^{-1}$
k_{Si}	thermal conductivity of Si	130 $\text{Wm}^{-1}\text{K}^{-1}$
k_{eva}	thermal conductivity of eva	0.38 $\text{Wm}^{-1}\text{K}^{-1}$
k_{tedlar}	thermal conductivity of tedlar	0.15 $\text{Wm}^{-1}\text{K}^{-1}$
k_{battery}	thermal conductivity of battery	0.81 $\text{Wm}^{-1}\text{K}^{-1}$
k_{frame}	thermal conductivity of frame	238 $\text{Wm}^{-1}\text{K}^{-1}$
$c_{\text{p,glass}}$	specific heat of glass	0.7 $\text{Jg}^{-1}\text{K}^{-1}$
$c_{\text{p,Si}}$	specific heat of Si	0.7 $\text{Jg}^{-1}K^{-1}$
$c_{\text{p,eva}}$	specific heat of eva	1.9 $\text{Jg}^{-1}\text{K}^{-1}$
$c_{\text{p,tedlar}}$	specific heat of tedlar	1.1 $\text{Jg}^{-1}\text{K}^{-1}$
$c_{\text{p,battery}}$	specific heat of battery	1.17 $\text{Jg}^{-1}\text{K}^{-1}$
$c_{\text{p,frame}}$	specific heat of frame	0.9 $\text{Jg}^{-1}\text{K}^{-1}$
ρ_{glass}	density of glass	2203 kg m^{-3}
ρ_{Si}	density of Si	2329 kg m^{-3}
ρ_{eva}	density of eva	930 kg m^{-3}
ρ_{tedlar}	density of tedlar	1300 kg m^{-3}
ρ_{battery}	density of battery	1965 kg m^{-3}
ρ_{frame}	density of frame	2700 kg m^{-3}
$\varepsilon_{\text{glass}}$	emissivity of glass	0.96
$\varepsilon_{\text{frame}}$	emissivity of frame	0.77
$\varepsilon_{\text{tedlar}}$	emissivity of tedlar	0.84
η_{PV}	efficiency of PV panel	16.19%
g	acceleration of gravity	9.81 ms^{-2}
σ	Stefan-Boltzmann constant	5.67x10-8 $\text{Wm}^{-2}\text{K}^{-4}$
R	reflectivity at glass layer	7%
A	absorptivity	3%

References

[1] V. Vega-Garita, L. Ramirez-Elizondo, and P. Bauer, *Physical integration of a photovoltaic-battery system: A thermal analysis,* Applied Energy **208**, 446 (2017).

[2] R. H. Wills, S. Krauthamer, A. Bulawka, and J. P. Posbic, *The AC Photovoltaic Module Concept,* Proceedings of the 32nd Intersociety Energy Conversion Engineering Conference (IECEC) , 1562 (1997).

[3] M. Ačanski, J. Popović-Gerber, and B. Ferreira, *Thermal modeling of the module integrated DC-DC converter for thin-film PV modules,* Proceedings of EPE-PEMC 2010 - 14th International Power Electronics and Motion Control Conference , 160 (2010).

[4] J. F. Reynaud, C. Alonso, P. Aloisi, C. Cabal, B. Estibals, G. Rigobert, G. Sarre, H. Rouault, D. Mourzagh, F. Mattera, and S. Genies, *Multifunctional module lithium-ion storage and photovoltaic conversion of solar energy,* in *Conference Record of the IEEE Photovoltaic Specialists Conference* (2008) pp. 1–5.

[5] J. F. Reynaud, O. Gantet, P. Aloïsi, B. Estibals, and C. Alonso, *New adaptive supervision unit to manage photovoltaic batteries,* IECON Proceedings (Industrial Electronics Conference) , 664 (2009).

[6] J. F. Reynaud, O. Gantet, P. Aloïsi, B. Estibals, and C. Alonso, *A novel distributed photovoltaic power architecture using advanced Li-ion batteries,* Proceedings of EPE-PEMC 2010 - 14th International Power Electronics and Motion Control Conference , 6 (2010).

[7] W. Grzesiak, P. Mackow, T. Maj, A. Polak, E. Klugmann-Radziemska, S. Zawora, K. Drabczyk, S. Gulkowski, and P. Grzesiak, *Innovative system for energy collection and management integrated within a photovoltaic module,* Solar Energy **132**, 442 (2016).

[8] F. Sarhaddi, S. Farahat, H. Ajam, a. Behzadmehr, and M. Mahdavi Adeli, *An improved thermal and electrical model for a solar photovoltaic thermal (PV/T) air collector,* Applied Energy **87**, 2328 (2010).

[9] G. N. Tiwari, R. K. Mishra, and S. C. Solanki, *Photovoltaic modules and their applications: A review on thermal modelling,* Applied Energy **88**, 2287 (2011).

[10] Q. Wang, B. Jiang, B. Li, and Y. Yan, *A critical review of thermal management models and solutions of lithium-ion batteries for the development of pure electric vehicles,* Renewable and Sustainable Energy Reviews **64**, 106 (2016).

[11] M. Monu, D. Ibrahim, and M. a. Rosen, *Review on use of phase change materials in battery thermal management for electric and hybrid electric vehicles,* International Journal of energy research **40**, 1011 (2016), arXiv:arXiv:1011.1669v3 .

[12] Z. Ling, Z. Zhang, G. Shi, X. Fang, L. Wang, X. Gao, Y. Fang, T. Xu, S. Wang, and X. Liu, *Review on thermal management systems using phase change materials for electronic components, Li-ion batteries and photovoltaic modules,* Renewable and Sustainable Energy Reviews **31**, 427 (2014).

[13] N. Javani, I. Dincer, G. F. Naterer, and B. S. Yilbas, *Heat transfer and thermal management with PCMs in a Li-ion battery cell for electric vehicles,* International Journal of Heat and Mass Transfer **72**, 690 (2014).

[14] Z. Ling, J. Chen, X. Fang, Z. Zhang, T. Xu, X. Gao, and S. Wang, *Experimental and numerical investigation of the application of phase change materials in a simulative power batteries thermal management system,* Applied Energy **121**, 104 (2014).

[15] H. Wang, F. Wang, Z. Li, Y. Tang, B. Yu, and W. Yuan, *Experimental investigation on the thermal performance of a heat sink filled with porous metal fiber sintered felt/paraffin composite phase change material,* Applied Energy **176**, 221 (2016).

[16] Z. G. Qu, W. Q. Li, and W. Q. Tao, *Numerical model of the passive thermal management system for high-power lithium ion battery by using porous metal foam saturated with phase change material,* International Journal of Hydrogen Energy **39**, 3904 (2014).

[17] N. Shani, *Architecture of Integrated PV-Battery Module: modeling, simulation, and comparison,* (2016).

[18] A123 Systems, *Battery Pack Design , Validation , and Assembly Guide using A123 Systems AMP20M1HD-A Nanophosphate Cells,* , 1 (2014).

[19] M. R. Palacin and A. de Guibert, *Why do batteries fail?* Science **351**, 1253292 (2016).

[20] X. Feng, J. Sun, M. Ouyang, X. He, L. Lu, X. Han, M. Fang, and H. Peng, *Characterization of large format lithium ion battery exposed to extremely high temperature,* Journal of Power Sources **272**, 457 (2014).

6

Prototype testing and battery selection

Previously, in chapter 5 a thermal model was developed to understand the conditions in which the components of the *PBIM* operate, and an air gap between the PV panel and battery pack was found to be useful to decrease the temperature of the components. This information was used to design a prototype that is part of the framework define in this chapter to select a suitable battery for the *PBIM*. The prototype was tested and the electrical and thermal behavior are part of chapter 6. The testing was elaborated to reproduce a worst case scenario resulting in a maximum temperature of 45°C for the battery pack, while the electrical performance of the prototype was measured. A temperature of 45°C was set, therefore, as the maximum temperature that the battery must handle, and it is utilized as the upper limit in the battery aging test in the second part of the chapter. The testing methodology not only reproduces the high temperature expected in the *PBIM* but also includes the charging and discharging profiles expected in a typical PV-battery system that undergoes charging and discharging processes per day. Among the different battery technologies, several battery candidates were evaluated by an integrated model that coupled the thermal behavior and the degradation of the batteries, concluding that Li-ion batteries are more appropriate. Consequently, $LiFePO_4$ and $LiCoO_2$ batteries were cycled at ambient temperature (22–26°C) and at high temperature (45°C) using three different current profiles. According to the cycling test, the $LiFePO_4$ cells show lower degradation rates than the $LiCoO_2$ cells, and as a result the $LiFePO_4$ is suggested as the most suitable technology for the integration of a solar panel and a battery pack in the same device.

This chapter is based on V. Vega-Garita, S. Garg, N. Narayan, L. Ramirez-Elizondo, and P. Bauer. *Testing a PV-Battery Integrated Module Prototype*, World Conference on Photovoltaic Energy Conversion 2018, (2018) [1]. Also, based on V. Vega-Garita, A. Hanif, L. Ramirez-Elizondo, and P. Bauer. *Selecting a Suitable Battery for the PV-battery Integrated Module*, Journal of Power Sources (2019), *under review* [2].

6.1. Introduction

With the final aim of selecting a suitable battery technology for the *PV-battery Integrated Module*, this chapter proposes a framework that is divided into two: the testing of a prototype of the *PBIM* (that serve as an input for the aging test) and an extensive battery aging test. In the first part, also Section 6.2, the steps followed towards the testing of the prototype are introduced. Firstly, the basic system architecture is described in Section 6.2.1, later the method designed for the testing is presented in Section 6.2.2 together with the system selected components in Section 6.2.3. Secondly, the results and analysis of the data produced by the prototype testing can be found in Section 6.3.

For the second part of the chapter, the methodology for selecting the battery technology is explained in Section 6.4, where the integrated model employed (Section 6.4.1) and the proposed method for designing the testing are presented (Section 6.4.2). As a continuation, the equipment used and the description of the experimental set-up is shown in Section 6.5. Moreover, the results of the aging testing along with the analysis of the different stress factors — temperature, current profile, and battery size — it is discussed in Section 6.6.

Before delving into the selection of suitable cells to be part of the *PBIM*'s battery pack, a brief review of the cells available in the market is carried out to help define the technologies that will be used for the prototype testing and aging test in Section 6.1.1. Later, the mechanisms behind battery capacity fading in Li-ion electrochemical cells are reviewed in Section 6.1.2.

6.1.1. Battery candidates

The general features of the most widely available batteries are shown in Table 6.1. There, the electrochemical cells are categorized based on metrics such as energy and power density, cycle life, cost, efficiency, and self-discharge.

Lead-acid (LA) batteries are considered a mature technology with low self-discharge and relatively low capital cost, which are their most prominent benefits when compared to other cells. However, LA batteries suffer from low cycle life as well as low energy and power density; therefore, these batteries are bulky and heavy and not suitable for the *PBIM*, where a high volumetric energy capacity is required. Moreover, they are made of toxic and not environmentally friendly elements [3].

Nickel-cadmium (NiCd) batteries are characterized by higher energy and power density, and better cycle life than lead-acid batteries [4]. These batteries also present memory effect [5] restricting the battery capacity according to its usage, and high values of self-discharge. Moreover, NiCd batteries are composed of the extremely toxic Cadmium adding to their disadvantages [6].

Nickel-metal hydride (NiMH) batteries are considered an improvement over the NiCd batteries, they are safer and less susceptible to memory effect issues. Additionally, they have a higher energy and power density than NiCd. Despite these advantages, the use of rare metals has resulted in an expensive alternative [5]. Also, NiMH still present problems previously experienced in the NiCd cells such as high self-discharge and low coulombic efficiencies [9].

According to Table 6.1, sodium-sulfur (NaS) and vanadium redox batteries (VRB) excel in terms of power density (NaS) and cycle life (VRB); however none of these

Table 6.1: Summary of available battery technologies. Based on [7][8].

Type	LA	NiCd	NiMH	Li-ion	NaS	VRB
Energy density (Wh kg^{-1})	25-50	50-60	60-120	75-200	150-240	10-30
Power density (W kg^{-1})	75-300	~200	250-1,000	500-2,000	150-230	80-150
Cycle life (100% DOD)	200-1,000	>1,500	180-2,000	1000-10,000	2,500-4,000	>12,000
Capital cost ($/kWh)	100-300	300-600	900-3500	300-2500	300-500	150-1,000
Round-trip efficiency	75-85	70-75	65-80	85-97	75-90	75-90
Self discharge	Low	High	High	Medium	–	Negligible

technologies are feasible for a concept as the *PBIM* for different reasons. In the case of the NaS, they are not suitable because the temperature of operation must be in the range of 300 to 350 °C, much higher than the expected in the integrated module [10]. When considering the VRB, this concept is discarded as they require the use of pumps, sensors, monitoring systems, and large vessels [11].

Therefore, Li-ion appears as a viable option taking into account its higher energy density than lead-acid, NiCd, and NiMH batteries, as well as higher efficiencies. Additionally, the problems related to memory effect and toxic element are avoided by using Li-ion cells. However, Li-ion cells are more normally more expensive than LA and NiCd and prone to self-discharging.

Among the Li-based cells, lithium-sulfur (Li-S) and solid electrolyte Li-ion batteries have not been considered, although promising, because of the early stage development and prohibitive prices. Specifically, Li-S could be able to store more energy than typical Li-ion cells, but the cells have not been able to show appropriate cycle life, and the cost remains quite high even compared to Li-ion [12]. Another alternative is Li-ion solid-state cells with a polymer electrolyte, which are considered safer than conventional Li-ion cells as they do not use volatile and flammable liquid electrolytes [13]. However, this technology is not mature yet, and it is associated with low power density, high ionic resistance at room temperature, and high manufacturing cost [14].

Comparison of Li-ion cells

The most widely employed material for the cathodes is lithium cobalt oxide (LCO) [15], or $LiCoO_2$, with advantages in terms of price, specific capacity, low self-discharge, good cycling performance and high discharge voltage [16] [17]. However, it has disadvantages such as accelerated aging at high currents [18], and low thermal stability when operating in temperatures between 100 and 150 °C [19].

The lithium nickel oxide cell (LNO), or $LiNiO_2$, has the same crystal structure and the theoretical specific capacity with the LCO. However, LNO batteries are even more

thermally unstable [18]. However, partial substitution of Co with Ni was found to be effective to reduce the cationic disorder [20]. The thermal stability can be improved by Mg doping and also adding a small amount of Al [21]. The structure becomes $LiNi_xCo_yAl_{(1-x-y)}O_2$ (NCA), or lithium nickel cobalt aluminum oxide, it is widely used commercially; however, elevated temperatures of operation (40-70 °C) can cause fast capacity decrease rates. [18].

Lithium manganese oxide ($LiMnO_2$) cells are potentially an interesting solution as they employ Mn instead of Co and Ni, lowering costs and avoiding the use of toxic materials [18]. Nonetheless, in Lithium manganese oxide (LMO) cells, the change in structure during the lithium-ion extraction has a negative impact on cycle life, and Mn tends to dissolve into electrolyte when the battery is not cycled [22]. The problem has been tackled by adding Co increasing the stability of the structure [23], and creating a new type of cell, the $LiNi_xCo_yMn_zO_2$ NMC. This kind of cells has a similar nominal voltage as the LCO, but it benefits from the less amount of Co used compared to LCO. The NMC cells also show appropriate cycle stability at 50 °C, although one of the significant issues of NMC is the unique voltage profile, which does not present the expected almost flat region found in cells such as $LiFePO_4$ (LFP).

Lithium iron phosphate batteries are considered as one of the more mature and stable Li-ion technologies [15], showing an excellent thermal stability and cycle life, good power capability, and is regarded as the safest lithium-ion type concerning thermal runaway risk. Despite all of those advantages, LFP cells are relatively lower in energy due to the low average voltage (3.2 - 3.4 V) [18].

From all of the comparisons above and the particular conditions of the *PBIM*, LCO and LFP are chosen as the battery candidates. While NMC shows relevant characteristics, its high price and the instability of the voltage discards it. LCO and LFP provide a right balance between the requirements. While LCO has low thermal stability in a significantly high temperature, around 100–150 °C, the *PBIM* is not operated in that temperature. Moreover, since the cell is used for a PV system, the discharge rate is relatively low (less than 1C). Therefore, the capacity fade in higher current rates will not affect the *PBIM*. For LFP, the most significant disadvantage is the low average voltage which results in low energy. However, this cell still has a superior energy density compared to most of the most popular cathode materials [17].

Moreover, for the *PBIM*, the form factor (geometry of the cell) is also relevant as prismatic and pouch cells can help to achieve higher capacity per unit of volume than cylindrical cells. Therefore, cells with these form factors (pouch and prismatic) were chosen in this chapter. Having identify LCO and LFP cells as potential battery technologies, the next section describes the causes behind battery aging and the influence of parameter such as current (related to C-rate), temperature, region of operation, and calendar aging.

6.1.2. Aging in Li-ion cells

The aging in electrochemical cells results in capacity fading or diminution of lifetime, which at the end is referred as a loss of available power or energy. The reduction of power in a battery is caused by an increase in the internal impedance, which then reduces the operating voltage of a cell. While the loss of the energy is a result of a

change of the active material to inactive material [24], degradation or aging process includes a decrease on the battery's capacity and an increase of the battery resistance leading to a battery failure. This process can be created by the conditions at which the battery is operated. Unfortunately, the aging process of a lithium-ion battery is complex, since the cause of aging can be a result from various interdependent mechanisms that cannot be studied separately [25].

Aging mechanisms can be divided into two categories, degradation produced by chemical reactions, and degradation caused by mechanical stress. Chemical degradation mechanisms consist of reduction and decomposition of the electrolyte, formation of solid-electrolyte interphase, binder decomposition, gas evolution, lithium-ion loss, and solvent co-intercalation [26]. Mechanical degradation of the battery mainly involves volume changes and stresses that occur in the active materials of the battery [27]. These volume changes and stresses can result in cracks, loss of contacts between active materials, and isolation [27][28]. These mechanisms can happen in different parts of a battery cell, the subsections below will compare different degradation modes in anode, cathode, and separator with various conditions that elevate the battery aging.

C-rate

High discharge and charge currents could increase capacity fading rates. One possible cause is related to the change on carbon structure at high discharge current rates, leading to an electrolyte or salt reduction on the carbon surface due to the instability of the electrolyte to carbon. This reaction will produce gas and decomposition which will ultimately thicken the SEI film on the carbon electrode. Furthermore, during a high current rate, the internal battery temperature augments, causing an increase in electrolyte reduction rate which produces gas increasing pressure, and producing damages on the surface film [29].

Temperature

According to the Arrhenius law, the chemical reaction rate is proportional to the temperature. Therefore, an increase in temperature results in an exponential rise in electrochemical reaction rates. According to [27], a 10°C increment in temperature could double the degradation rate of a cell. At high temperature the protective solid electrolyte interphase (SEI), formed at the first cells cycles, degrades faster, provoking the dissolution of SEI and propitiating the formation of more stable inorganic products such as lithium salts like lithium fluoride or lithium carbonate [25]. These new compounds are not just harder while making more difficult the Li-ion diffusion, but contribute to decrease the amount of active Li [30]. Hence, the capacity loss of the cell is the consequence.

Region of operation

The battery internal resistance increases when the cells is near to be completely full or empty, which correlates to high SOCs and low SOCs, respectively. Therefore, cells that undergo processes in which the SOC varies significantly end up working in regions with high internal resistance. High internal resistance leads to a rise in battery temperature, which ultimately causes a faster capacity degradation rate.

Calendar aging
This type of aging is not related to the aging due to the activity of the battery, instead it has to do with the periods of battery inactivity. For instance, if the batteries are stored at high temperatures, that can help to accelerate the degradation of the battery [31]. Also, when cells are stored high SOC levels, anode remains fully lithiated which result in an unstable electrode that could interact with the solvent components reducing the amount of electrode available [32].

6.1.3. Contributions
In summary, chapter 6 contributes towards

- measuring the thermal and electrical behavior of the *PBIM* under severe temperature conditions (Sections 6.3.1, 6.3.2, and 6.3.3),
- comparing the thermal and electrical response of the *PBIM* to a system with the components detached from the PV panel (Section 6.3.4),
- assessing different electrochemical cell technologies using an integrated model and suggest the most appropriate battery candidates (Section 6.4.1),
- proposing a testing application-based methodology that reproduces the operational conditions of the *PBIM* (Section 6.4.2), and
- selecting a suitable battery technology for the *PBIM* by performing an aging test at room temperature (22–26°C) and at 45°C (Section 6.6.3).

6.2. Experiment set-up for testing the prototype
As illustrated in Figure 6.1, the constructed prototype consists of a PV panel, four prismatic $LiFePO_4$ cells, and a charge controller (CC). Between the PV panel and the bottom metallic sheet that hold the batteries and CC, there is a air gap of 6 cm — a value found to be optimum in Section 5.4.2 to keep the batteries operating at the lowest possible temperature. The metallic frame holds the balance of system components and provides appropriate ventilation (Figure 6.1a). The frame is also attached to the aluminum frame of the PV panel (Figure 6.1b).

6.2.1. System architecture
A simple system architecture is shown in Figure 6.2a, in which the PV panel is connected to a CC that controls the battery charging process imposing a constant current and constant voltage pattern. The CC also performs maximum power point tracking (MPPT), while the battery pack is directly connected to a DC load which defines the discharging process.

6.2.2. Testing methodology
The prototype was tested indoors using a solar simulator to reproduce an environment with both high irradiation and ambient temperature. The purpose of these conditions is to evaluate the prototype under severe conditions and study the general performance

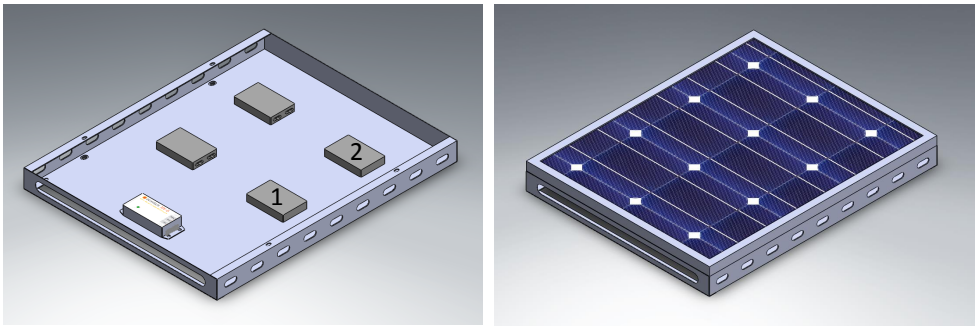

(a) (b)

Figure 6.1: (a) Frame and balance of system components, where 1 and 2 indicate the batteries studied during the testing; and (b) complete prototype.

of the system, while also for assessing the stability and safety of the prototype simultaneously

The testing follows three stages, as depicted in Figure 6.2b and summarized as follows:

- Stage a: The solar panel is irradiated, and the batteries are charged while the load is not supplied.
- Stage b: The solar simulator and DC load are switched off (idle period).
- Stage c: The battery is discharged at a power set by the load.

At the beginning (stage a), the solar simulator is turned on, and the irradiation is kept constant while charging the battery pack for 30 minutes. After which (stage b), the simulator is switched off. Then, the DC load is fed by discharging batteries for 5 minutes, at a constant power rating of 40 W (stage c).

As Figure 6.2c shows, the prototype was placed under a large area solar simulator at a distance of 1 m. The solar simulator is able to generate irradiance of 1050-1150

Table 6.2: PV panel and battery characteristics

PV panel		***Battery***	
Parameter	Value	Parameter	Value
$P_{\max}$	50 W_p	V_{nominal}	3.2 V
V_{mpp}	18 V	Capacity	8 Ah
I_{mpp}	2.78 A	V_{range}	2.6–3.65 V (80% DOD)
V_{OC}	22.2 V	Life cycle	2000 (80% DOD)
I_{SC}	3.09 A	T_{range}	-20 – 60 °C
η_{PV}	13.82%	Dimensions	1.8 x 6.8 x 11.3 cm^3
A_{PV}	0.54 x 0.67 m^2	Weight	258 g

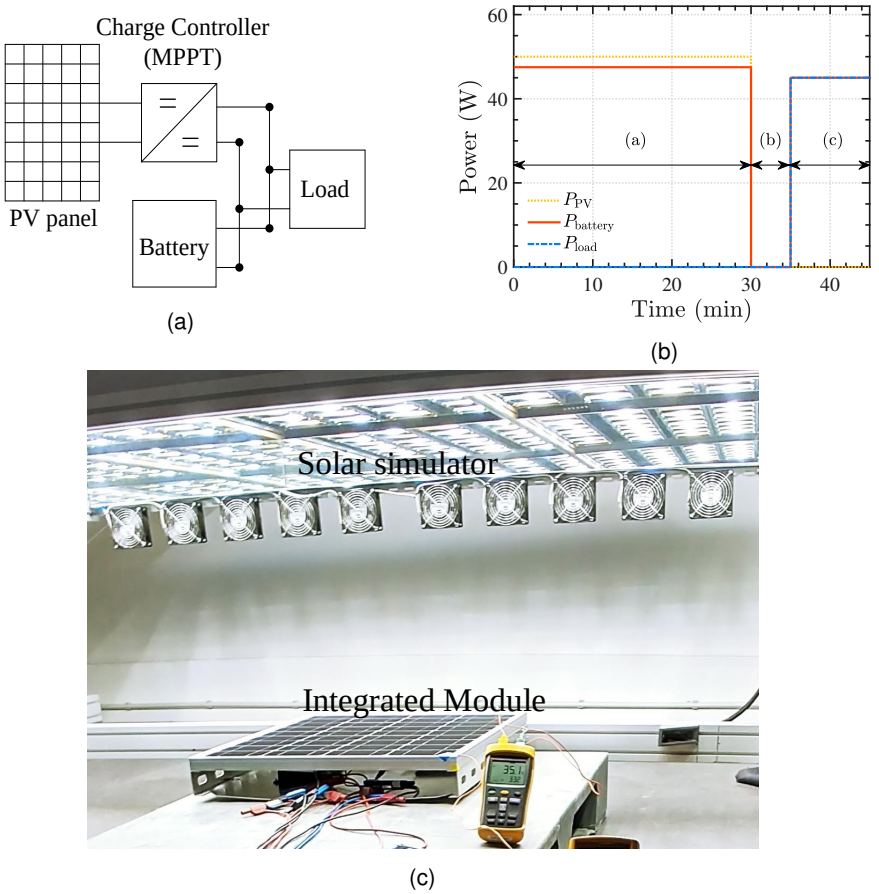

Figure 6.2: Characteristics of the prototype testing, (a) architecture of prototype, (b) testing procedure, and (c) testing set-up.

W/m^2 (Eternal Sun, class AAA). The dynamic irradiance values during the tests were recorded using a pyranometer (Hukseflux). From the prototype, all the connections to measure currents, voltages, and temperatures were made.

The power produced by the solar panel, as well as the power stored or released by the battery to the load were measured every 20 seconds during the testing using a data acquisition unit Agilent 34970A. The temperature probes were located at the top of the two selected batteries presented in Figure 6.1a (called 1 and 2), and also on the CC, while their temperatures were monitored with a time step of 1 min. Moreover, the top surface of the PV panel was measured with an IR thermometer (Fluke 568).

6.2.3. Components

The designed prototype consists of a polycrystalline Silicon panel from Blue Solar, a Genasun GV-5-Li-14.2V charge controller, and four battery packs of $LiFePO_4$ cells con-

nected in series. The characteristics of the PV panel and battery pack are summarized in Table 6.2.

6.2.4. Efficiency

The electrical performance of the *PBIM* and conventional system (components not attached to the PV panel) is evaluated by calculating the efficiency of the solar panel (η_{PV}) and the efficiency related to the DC/DC conversion stage performed by the CC during the charging process ($\eta_{\mathrm{CC_{charging}}}$). In the case of the solar panel, it is estimated using the equation below:

$$\eta_{\mathrm{PV}} = \frac{P_{\mathrm{PV}}}{G_{\mathrm{SS}} \mathrm{x} A_{\mathrm{PV}}} \times 100 \quad [\%], \tag{6.1}$$

where the P_{PV} is the power produced by the solar panel, G_{SS} is the irradiance of the solar simulator, and A_{PV} is the area of the panel. To estimate the efficiency of the conversion stage implemented in the CC, the ratio between the PV power (P_{PV}) and power supply to the battery (P_{battery}) is calculated as follows:

$$\eta_{\mathrm{CC_{charging}}} = \frac{P_{\mathrm{battery}}}{P_{\mathrm{PV}}} \times 100 \quad [\%]. \tag{6.2}$$

6.3. Prototype testing results

6.3.1. Power conversion and PV panel efficiency

The individual current and voltage readings from the battery pack and PV panel were logged and used as inputs in Equation 6.2 to estimate the dynamically changing efficiency of CC DC/DC conversion stage. CC's efficiency is a function of battery charging power, which depends on PV power. As shown in Figure 6.3a, the efficiency varies between 95% and 96.5%. This variation does not seem to be related to any particular

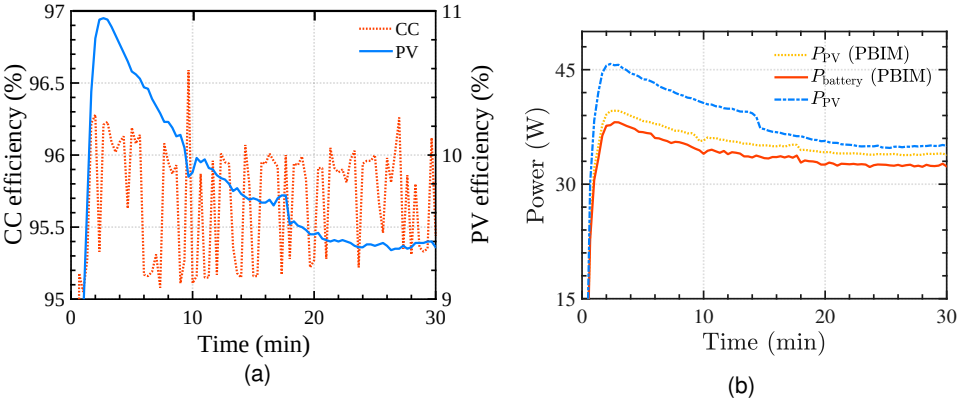

Figure 6.3: Efficiency and change of PV power, (a) charging efficiency (30 s sampling interval), and (b) PV and battery power for the *PBIM* and a conventional system (batteries and CC not attached to the PV panel).

physical phenomenon apart from the slight shifting in irradiation produced by the solar simulator, which causes the MPPT algorithm to alter its operating point occasionally. These fluctuations also have a limited effect on the PV panel temperature and performance trends.

For the period studied, the average efficiency is 95.7%. This percentage is an appropriate value for a converter operating at partial load values, considering that the rated PV peak power is 65 W. The efficiency of the converter is reported only for the period in which solar power is produced, leaving out the section where the battery is directly supplying the load. The effect of high temperature on CC performance is not considered in this study, although its top surface temperature was measured along the testing, showing a similar temperature pattern as batteries in Figure 6.4b.

The solar panel efficiency is highly influenced by the panel temperature, and as the panel gets warmer its value drops almost 1/3 of the rated efficiency as compared to the beginning of the test (see Figure 6.3a). This reduction in efficiency has implications on the power delivered, as it will be discussed in the next section.

6.3.2. PV power and temperature

Initially, according to Figure 6.3b, the PV and battery power increased rapidly due to the sudden increase in irradiance. The PV panel power output dropped to 40 W after a few minutes, below the rated 50 W_p set by the manufacturer at standard test conditions (STC). The main reason behind this result is that even when the solar simulator can illuminate the PV panel with a high-quality AM 1.5 spectrum, keeping the temperature of the solar panel at 25°C is not possible in real-time applications. As a consequence, reduced heat dissipation of the PV panel deteriorates its efficiency and consequently its power generation.

As the test continued, PV power diminished as the temperature of the solar panel rose due to the reduction of maximum power point voltage (V_{mpp}), leading to a decreasing trend in the PV and battery charging power, besides the slight rise expected with

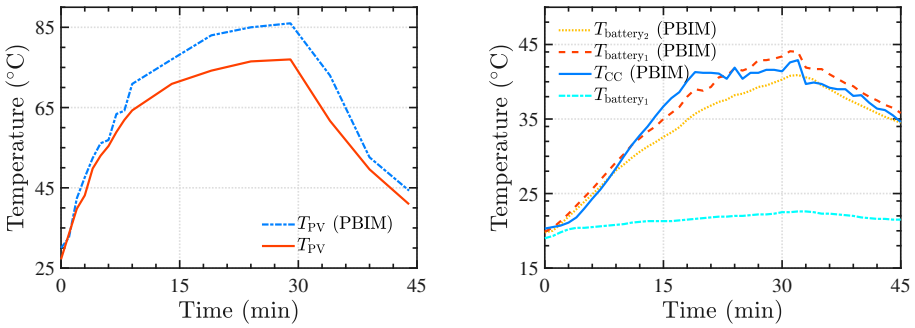

Figure 6.4: PV and battery temperature change with time. (a) Solar panel temperature, and (b) temperature of batteries and charge controller (CC). Both figures compare the *PBIM* and a conventional system (batteries and CC not attached to the PV panel).

the I_{mpp}. The decrease in V_{mpp} is associated with the reduction of the Si band gap, and a higher intrinsic carrier concentration in comparison to that at lower temperatures [33].

The temperature of the solar panel was 30°C when initiating the test, but after only 7 minutes, the temperature of the panel reached 63°C. The temperature increments proceeded, and hit a maximum of 86°C at the 25-minute mark, maintaining the values until the solar simulator was turned off. The abrupt increase in solar panel temperature corresponded with the behavior observed in Figure 6.3b, where there was a drop of around 6 W between the highest value of PV power and the lowest measurement, representing a reduction of 16%.

6.3.3. Battery temperature

Besides the thermal effects on the PV panel, the battery pack must be studied, and particular attention must be paid to ensure its safe operation. As expected, the temperature of the electrochemical cells increased with time. When starting the test, the electrochemical cells shared a common temperature close to 20°C. As the test advanced, the temperature between them differed slightly but followed the same pattern as shown in Figure 6.4b. The differences in temperature among the electrochemical cells corresponded to the different placing of the cells. While cell 1 is located in the center of the metallic casing (Figure 6.1a), cell 2 is closer to the casing end. Therefore, cell 1 accepts more easily the heat from the PV panel than cell 2. As soon as the irradiation is eliminated, cell 1 and 2 cool down at a similar rate.

The information provided by this test must be taken into account when designing the battery pack balance system, to account for small changes in voltage due to the not completely uniform heat distribution throughout the cells. Regarding absolute temperature values, it is important to mention that even in an unlikely event where the irradiance remain constant for almost 30 minutes, the batteries never surpass 45°C. This proves that the air gap between the PV panel and the cells protect the components from extreme overheating.

6.3.4. *PBIM* vs. a conventional system

Higher temperatures are expected in a fully integrated system in contrast to a conventional system, which is confirmed by Figures 6.4a and 6.4b.

Since the PV panel in the *PBIM* does not efficiently dissipate the heat produced at the solar cell level, while comparing with a regular solar panel with no components attached [34] [35], the temperature of the panel is higher, and therefore, the reduction on power more pronounced. On average, the solar panel temperature of the prototype was 9.34% higher, representing a 4.3% (1.3 W) diminution of PV power when compared to the benchmark (Figure 6.3b).

The same happened when the batteries were integrated in the *PBIM*; when the batteries were separated from the solar panel, they operated at an almost constant temperature of 22°C. Also, the maximum difference between the battery in the *PBIM* and a conventional system was 23°C.

Given elevated temperatures, the components of the *PBIM* are expected to degrade faster than a standard system. Therefore, it is essential to focus on this issue, as introduced in the next section for the batteries.

6.4. Methodology for battery selection

The procedure followed to select a battery technology is summarized in Figure 6.5, where the process started by comparing the various technologies and filtering out the technologies that are not feasible in terms of suggested temperature of operation, complexity of implementation, form factor, and cost. This step was thoroughly carried out in Section 6.1.1 of this chapter, resulting in Li-ion cells as the technology that shows better features.

Secondly, an integrated model, explained in more detail in the next section, is developed with two main objectives in mind: evaluate battery technology candidates and help in the design of the testing experiment. The battery candidates will be evaluated employing a common tailor-made model that replicates the conditions of a PV-battery system. For the testing design, the model is useful as it will help defining the current profiles applied in the degradation testing and estimates the expected aging with previous models developed in this thesis for the *PBIM*. Thirdly, the test not only includes the influence of the charging and discharging profiles of a typical off-grid system but also takes into account the information provided by the prototype testing, which is used to set the maximum temperature of the degradation test.

Finally, once the cycling testing is set, the selected technology is extensively tested to quantify the effect of temperature and different current profiles on battery degradation. For comparison purposes, two sets of experiments are carried out simultaneously, one tries to follow the severe conditions defined by the prototype testing, and the second is controlled to reproduce the relatively low temperature of a typical solar system with the battery at a relatively constant temperature close to ambient. Based on these results, a battery technology is suggested to be more appropriate for the characteristics of the *PBIM*.

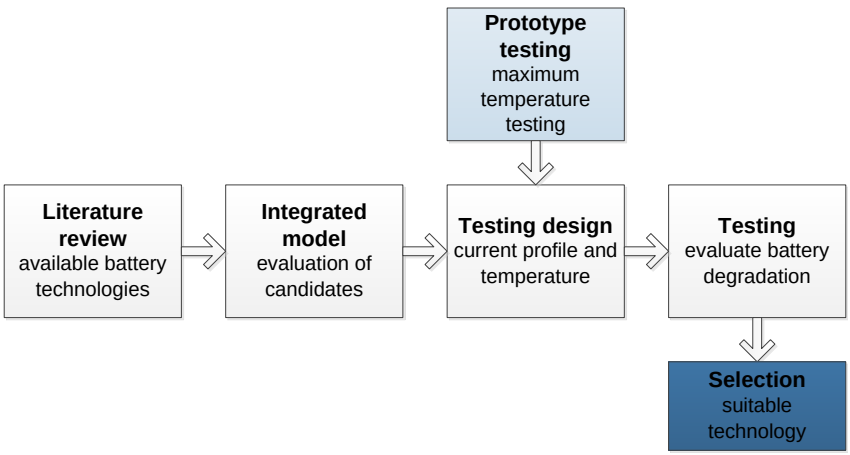

Figure 6.5: Methodology for selecting a suitable battery technology for the *PBIM*.

6.4.1. Integrated model

The integrated model is similar to the model described in detail in chapter 3, particularly in Section 3.3. The same solar irradiation data and load (tier 3) are taken as inputs for the integrated model, as can be appreciated in Figure 3.7. Here, the dynamic change on battery voltage is also modeled using the previously published model by Tremblay [36], considering the voltage and the required power from or to the battery, the battery current is calculated, and the heat generated by the battery can be estimated. This model is also modified to include the effect of temperature on battery parameters.

The temperature of the battery, as well as the PV temperature, is calculated using a 1-D thermal resistance model of the *PBIM* that allows the precise calculation of the PV production. This 1-D thermal model was explained in Section 3.3.3 of chapter 3. Lastly, the temperature and energy processed by the battery are incorporated into a generic model that uses the relationship between cycles, depth of discharge (1-SOC), and temperature usually reported by battery manufacturers. This model is based on a zero crossings method that considers the degradation due to battery cycling every period of activity [37]. After including the effects of previously described, the new capacity of the battery is determined and is feedback to the dynamic battery model; in this manner, the usable capacity of the battery continue decreasing as the simulation time advances.

By utilizing the integrated model, three battery technologies, namely lead-acid, NiCd, and $LiFePO_4$, were studied; their main features can be observed in Table 6.3. Although the batteries in Table 6.3 are not necessarily suitable for the *PBIM*, they serve for the purpose of comparing the chosen battery technologies.

After performing a simulation for one year, the state of health for every battery is depicted in Figure 6.6. For all the cases, the battery is battery size is 660 Wh (also referred as 10 batteries) and a PV rating 320 W_p. It can be observed that the lead-acid battery presents the lowest SOH followed by the NiCd which also degraded faster than the Li-ion battery. As a result, the focus of this chapter will be on Li-ion batteries as they can last longer than other technologies in PV-battery systems.

Once Li-ion is chosen, the battery capacity is increased in steps of 66 Wh (1 battery), from 66 to 660 Wh (10 batteries) to understand its effect on current profiles. As expected, less number of batteries connected in series, results in high instantaneous current values, as for the same power the voltage is lower, compared to bigger battery packs. This can be observed in Figure 6.7, where the yellow dashed line for 1 battery reaches values beyond 20 A, while for the other battery sizes the current never surpasses -15 A. The extension of the battery idle period also varies as a function of battery size, smaller battery sizes causes more extended inactivity periods.

6.4.2. Testing design

For the current profiles used in the testing, a cycle is considered as a complete charging discharging process; the charging happens in the day and the discharging starts in the afternoon and extends to the night. During these two processes, the battery is completely charged and fully discharged later, and the energy charged and discharged is identical. In terms of SOC, it is established that the battery SOC should never drop below 10% or be charged above 90%. This is defined to prevent overdischarging and

Table 6.3: Specifications of the three different battery types used as imputs for the integrated model.

Technology	**Brand**	**Capacity** (Ah)	**Voltage** (V)
$LiFePO_4$	ValenceU1-12XP	10	3.2
Lead-acid (Sealed)	Enersys Cyclon D Single Cell	2.5	2.3
NiCd	Saft Nickel-Cadmium VRE D	5.5	1.2

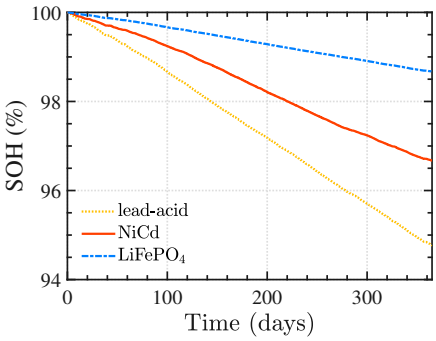

Figure 6.6: Simulation of the state of health of three battery technologies (lead-acid, NiCd, and Li-ion) for 365 days.

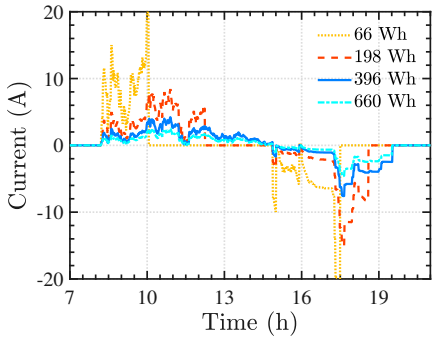

Figure 6.7: Four current profiles for different battery sizes: 66, 198, 396, and 660 Wh.

overcharging.

Another important feature of the testing is that the periods of inactivity are eliminated with the objective of shortening the duration of each cycle, and therefore, be able to realize more than one cycle per natural day. The final profiles used in the testing are plotted in Figure 6.8. Two profiles, 66 Wh and 198 Wh, were chosen as they represent the cases in which the battery pack experience the two highest current values for the chosen sizes. Here, it is important to point out that the energy processed by the battery in both cases (profiles) is the same, they just differ on the current values and on the cycle duration. The purpose is, therefore, to study if dissimilar profiles result in different

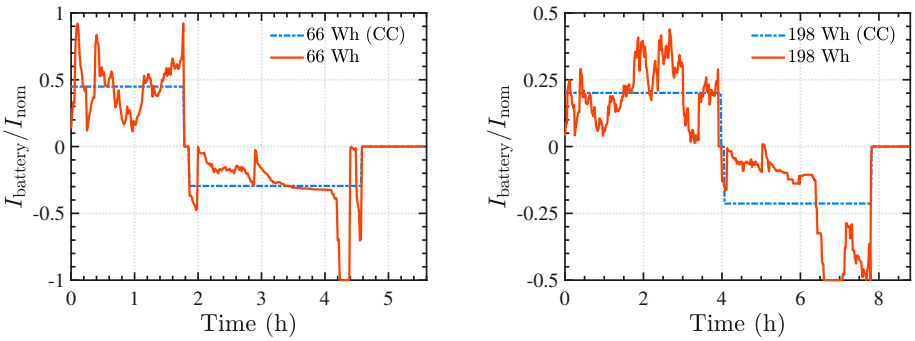

(a) For a battery size of 66 Wh (D66), the dashed blue line corresponds to the CC profile and the red line to the dynamic profile.

(b) For a battery size of 198 Wh (D198), the dashed blue line corresponds to the CC profile and the red line to the dynamic profile.

Figure 6.8: Current profile for (a) 66 Wh battery size and (b) 198 Wh battery size.

degradation rates. In Figures 6.8a and 6.8b, a red dashed line can be noted; this line depicts the constant current (CC) equivalent profile associated to every battery size. The CC profiles are also added to investigate whether they speed up or reduce the battery aging rate in comparison to the dynamically changing profiles —they also cycle the same energy. In total, the 66 Wh profiles take 5.5 hours to be executed, while the 198 Wh profile lasts for 10.83 hours including the 5 minutes resting time between charging and discharging in both profiles to allow a brief voltage relaxation.

Battery temperature is recognized to have a significant influence on degradation. Therefore, two temperature extremes were defined in order to delimit the region in which the *PBIM* is expected to work on. Consequently, as stated in Section 6.3.3, the upper limit reached by the batteries in poor cooling conditions and high irradiation was 45°C. Therefore, based on the prototype testing, the batteries will be tested at 45°C using the previously commented profiles. Conversely, the cycling testing will be carried out at an ambient temperature varying between 22 to 26°C. This temperature range corresponds to the expected thermal response of a standard PV-battery system with the batteries placed indoors. In Section 6.3.4, similar temperatures were measured.

With the objective of measuring the actual battery capacity after every cycling test, the procedure used consist of three main phases, a charging step composed of a CC and constant voltage (CV), a resting period of 1 hour, and a discharging period with a CC-CV profile, as described in Figure 6.9.

After describing the formulation of the battery degradation test, the general procedure for the testing can be summarized as follows:

- **Cycling**: profiles that represented a battery size of 66 and 198 Wh are repeated around 30 times and 20, respectively.

- **Capacity measurement**: the discharged capacity is measured and compared to the previous values at 25°C.

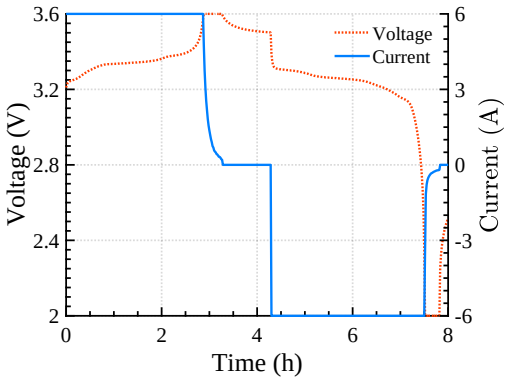

Figure 6.9: Constant current and constant voltage profile for measuring battery capacity.

- **Charge to 10% SOC**: because the battery was completely discharged in the previous step, the battery must be charge till 10% so the cycling test can be resumed.

6.5. Battery testing set-up

According to Section 6.1.1, $LiFePO_4$ (LFP) and a $LiCoO_2$ (LCO) were selected to undergo the cycling test. In Table 6.4, the characteristics of the LFP and LCO batteries are presented; this information is fundamental for both the cycling current profiles and the capacity the measurement steps. Based on the nominal current, the magnitude of the current for all the time steps is determined accordingly. For instance, 18.44 A is the maximum current imposed to the LFP and 2.58 for the LCO —for a battery size of 66 Wh. The end-of-discharge voltage and maximum voltage are set as the upper and lower values for the capacity measurement step; at these voltages, the transitions from CC to CV are defined for the charging and discharging processes. Moreover, because the batteries are fully discharged after the capacity measurement, 10% of the capacity is charged at the nominal battery current given by the manufacturer. Here, it is important to clarify that the 10% SOC is updated after every capacity measurement to account for the battery degradation suffered.

As an overview, Table 6.5 introduces the general arrangement of the testing. Eight LFP batteries (from LFP 1 to LFP 8) are tested at two reference temperatures (45°C and 22-26°C) and following four different current profiles, namely, dynamic 66Wh, 66Wh at CC, dynamic 198Wh, and 198Wh at CC.

A dynamic profile, as the name suggests, it is characterised by a constantly changing value of the current, while in a CC profile the value of the current is fixed for a predefined period. As an overview, Table 6.5 introduces the general arrangement of the testing. Eight LFP batteries (from LFP #1 to LFP #8) are tested at two reference temperatures, 45°C and 22–26°C (room temperature), and following four different current profiles, namely, dynamic 66 Wh (D66), 66 Wh at CC (CC66), dynamic 198 Wh

(D198), and 198 Wh at CC (CC198).

For the four LCO cells, they were examined using two current profiles, dynamic 66 Wh and dynamic 198 Wh, for two temperatures, 45°C and 22–26°C, due to limitations in the number of channels available. The initial capacity of the cells is reported in Table 6.5, showing a slight difference among them.

Table 6.4: Technical specifications of A123systems AMP20M1HD-A cell [38] and Renata ICP606168PRT cell [39].

Specifications	**$LiFePO_4$**	**$LiCoO_2$**
Nominal capacity	20 Ah	2.8
Nominal current	6 A	0.56
Nominal voltage	3.3 V	3.7
End-of-discharge voltage	2.0 V	3
Maximum voltage	3.6 V	4.2

Table 6.5: Initial capacities for the selected cells. RT: room temperature (22–26°C)

Channel	**Battery**	**Profile**	**Temperature** (°C)	**Initial capacity** (Ah)
1,2	LFP #1	D66	45	20.06
3	LFP #2	CC66	45	20.02
4	LFP #3	D198	45	19.90
5	LFP #4	CC198	45	20.05
6,7	LFP #5	D66	RT	20.10
8	LFP #6	CC66	RT	20.28
9	LFP #7	D198	RT	19.83
10	LFP #8	CC198	RT	20.39
11	LCO #1	D66	45	2.73
12	LCO #2	D198	45	2.78
13	LCO #3	D66	RT	2.71
14	LCO #4	D198	RT	2.75

6.5.1. Equipment

The general testing set-up is shown in Figure 6.10a, where the climate chamber in charge of keeping the temperature at 45°C, the battery tester, and the chamber that maintains the batteries at room temperature can be seen. The climate chamber (Memmert, Climatic test chamber CTC 256) was able to sustain the temperature of the chamber within ± 2°C from the set point.

Each cell had a K-type thermocouple attached to it to monitor its thermal behavior throughout the testing, as well as the voltage was continuously measured (Figures 6.10b and 6.10c), the information was retrieved and saved by the battery tester every 1 minute.

The battery tester (Arbin, model LBT22043) has 16 channels and the maximum absolute current that can be drawn from a single channel is 10 A (Table 6.5). For

these reasons, channels 1&2 and 6&7 are connected in parallel so they can provide current beyond 10 A as requested by 66 Wh profile for the LFP cell (refer to Table 6.5). Finally, the batteries placed inside the climate chamber present slight differences in temperature due to the not completely uniform temperature distribution inside the climate chamber; however, the difference between them was never more than 1.5°C.

6.6. Battery degradation results

In this section, the effect of temperature and the different current profiles over battery degradation are analyzed for the $LiFePO_4$ and $LiCoO_2$ cells. Also, a comparison between these two technologies is carried out to select the most suitable one. Here, it is important to point out that for the 66 Wh profile, more cycles were performed because it lasts shorter than the 198 Wh profile; however, when analyzing the results between current profiles, the values are interpolated to perform a fair comparison.

6.6.1. Lithium iron phosphate cells

Temperature effect

As anticipated, the batteries tested at 45°C presented lower SOH values compared to the batteries maintained at room temperature for the same current profiles (Figures 6.11a and Figure 6.11b). Although in general high temperatures cause an immediate increase in the ability of the battery to store and release energy, the capacity of the battery tends to decrease faster in the long term relative to batteries exposed to colder conditions. Because the chemical activity is incentivized by warm conditions, the electrochemical reactions increase their rates favoring the intercalation process but also provoking a faster consumption of active lithium by means of undesired side reactions.

In Figure 6.11a, it can be seen that the degradation is more pronounced as the batteries are more cycled for both the constant current profile and the dynamic profiles. To quantify this change, Table 6.7 summarizes the results for the LFP cells cycled with a 66 Wh profiles. The difference between the cells cycled at 25°C and 45°C in SOH was 0.77%, 1.68%, and 1.84% for the cycles 100, 190, and 250, respectively showing an increasing trend. Similarly, for the CC profile, the LFP cells degraded 1.64% less at 25°C than at 45°C in the cycle number 250. In Figure 6.11b and Table 6.8, the same behavior is observed for the 198 Wh profile.

Table 6.6: Technical specifications of the battery tester Arbin, model LBT22043.

Specifications	Value
Number of test channels	16 channels
Voltage ranges	0 – 25 V
Current ranges	-10 – 10 A
Temperature ranges	0 – 100°C
Operating modes	CC, CV, and CC-CV

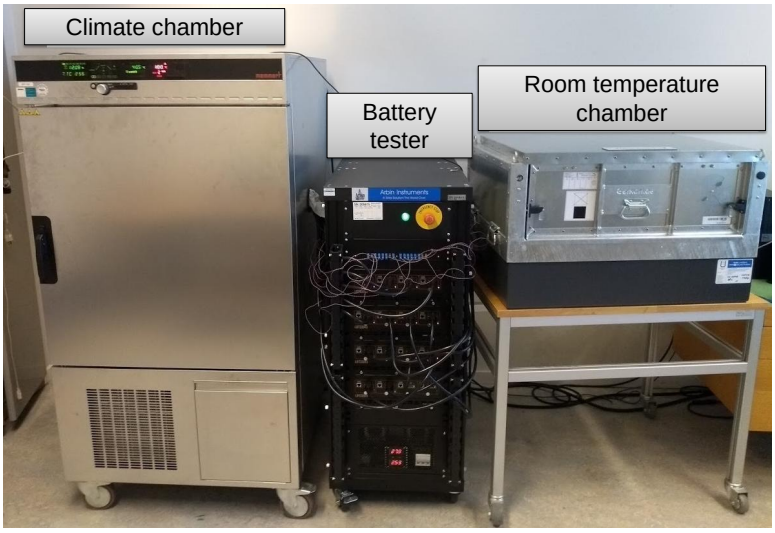

(a) General set-up

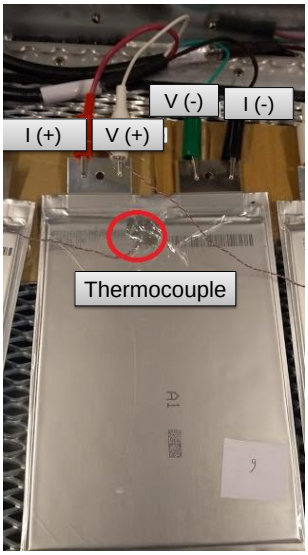

(b) LFP

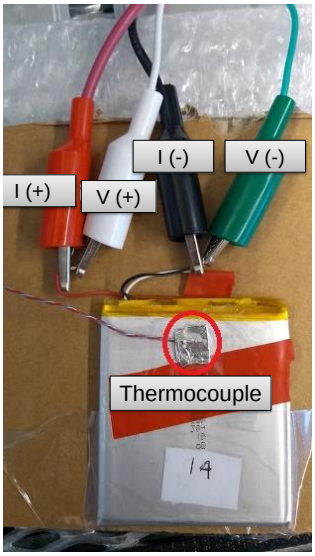

(c) LCO

Figure 6.10: Battery testing set-u, (a) general set-up consisting of a climate chamber, a battery tester, and chamber at room temperature. (b) Interconnection and location of thermocouple for a chose LFP cell. (c) Interconnection and location of thermocouple for a chosen LCO cell.

Constant current (CC) vs. dynamic profile

In this section, the consequences of imposing a CC and dynamic current profiles with the same energy content, 66 Wh or 198 Wh, are analyzed for the same temperatures

Table 6.7: Difference in SOH (ΔSOH) between cells tested at RT and 45°C for LFP cells after 100, 190 and 250 cycles. The cells are cycled with a constant current profile (CC66) and a dynamic profiles (D66) for a battery size of 66 Wh.

cycles	SOH (%) 45°C	SOH (%) 25°C	Δ SOH (%)	SOH (%) 45°C (CC)	SOH (%) 25°C (CC)	Δ SOH (%)
100	98.59	99.35	0.77	98.79	99.35	0.56
190	97.18	98.86	1.68	98.08	98.88	0.79
250	96.51	98.35	1.84	97.06	98.70	1.64

Table 6.8: Difference in state health (ΔSOH) between cells tested at RT and 45°C for LFP cells after 46, 102 and 160 cycles. The cells are cycled with a constant current profile (CC198) and a dynamic profiles (D198) for a battery size of 198 Wh.

cycles	SOH (%) 45°C	SOH (%) 25°C	Δ SOH (%)	SOH (%) 45°C (CC)	SOH (%) 25°C (CC)	Δ SOH (%)
46	99.67	99.86	0.18	98.92	99.78	0.86
102	98.41	99.10	0.68	97.84	99.24	1.41
160	97.56	98.70	1.14	97.20	98.85	1.65

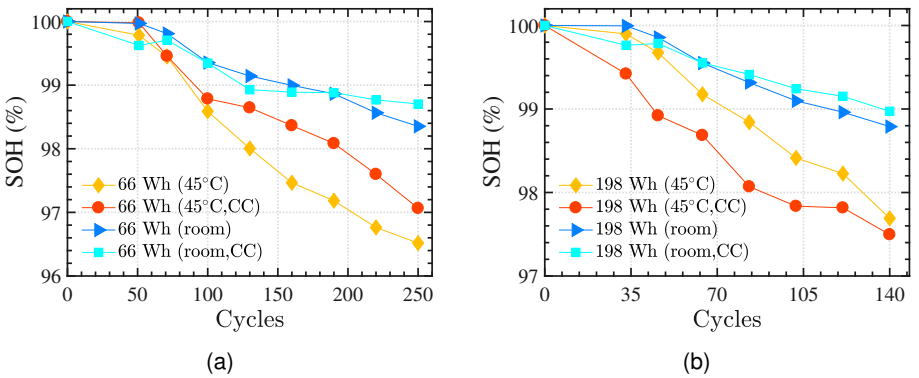

(a) (b)

Figure 6.11: SOH variation for (a) LFP cells cycled with a dynamic 66 Wh profile (D66) at room temperature and 45°C, and (b) LFP cells cycled with a dynamic 198 Wh profile (D198) at room temperature and 45°C.

using Tables 6.7 and 6.7.

For the 66 Wh dynamic profiles at 45°C, it can be observed that the SOH is always higher in the case of the CC profile (Table 6.7). For instance, at the cycle 250, the difference in terms of SOH varies from 0.2 to 0.9 % for all the cycles (0–250). For the 66Wh profile, now at room temperature, the CC profile sometimes results in higher SOHs while for other cycles is lower, as depicted in Figure 6.11a, but the differences are always within $\pm$0.35%. Therefore, it can be said that the CC profile at 45°C presents lower degradation than the dynamic profile, but at 25°C no representative trend is ob-

Table 6.9: Difference in SOH (ΔSOH) for cells tested using profiles representing the battery sizes of 66 Wh and 198 Wh for LFP cells after 51, 100 and 160 cycles. The cells were tested at 45°C and room temperature. Note: the values for 198 Wh were linearly interpolated to make a fair comparison between battery sizes. For cycle 51: 46–64, and for cycle 100: 83–102.

cycles	SOH (%) 45°C, 66 Wh	SOH (%) 45°C, 198 Wh	Δ SOH (%)	SOH (%) 25°C, 66 Wh	SOH (%) 25°C, 198 Wh	Δ SOH (%)
51	99.78	99.54	0.25	99.97	99.77	0.20
100	98.59	98.46	0.13	99.35	99.12	0.23
160	97.47	96.56	-0.09	99.00	98.70	0.3

served.

When having a look at the 198 Wh battery size (Figure 6.11b and Table 6.8), two main conclusions can be drawn: the CC profile presents the lower SOH for 45°C, and for room temperature, a slight positive effect of CC can be seen.

If a general observation were to be made about the positive or negative effect of imposing a CC profile over the LFP cells, more extensive testing must be performed to elucidate the causes of the contradictory information observed for the 66 Wh and 198 Wh cases.

Comparing profiles with different battery sizes for LFP: 66 Wh vs. 198 Wh

This section explores the relationship between the current profiles defined for the 66 and 198 Wh battery sizes not considering the influence of temperature. By using Table 6.9, the profiles can be studied based on the difference of SOH after 51, 100, and 160 cycles. By keeping the temperature value at 45°C and contrasting the SOHs for the 66 and 198 Wh dynamic profles, there is no a clear indication about the effect of the profiles on battery degradation as the dissimilarity between them is not more than 0.25% for any cycle. Similarly, at 25°C, the SOH remains slightly higher in favor of the 66 Wh profile with a maximum difference of 0.3%. Thus, it is concluded that the effect of the momentously higher currents experienced in the 66 Wh profile compared to the longer cycles are not more harmful than the more extended profiles defined for the 198 Wh current profiles.

Which parameter plays a more prominent role for the LFP cells?

From Section 6.6.1, differences till 1.84% on SOH were found for batteries exposed to 45°C while using a CC compared to a dynamic profiles does not show a definitive negative impact on battery aging. Moreover, the different current profiles corresponding to battery sizes of 66 Wh and 198 Wh seem not to cause a significant adverse impact on battery aging. Therefore, the negative influence of high temperature is the primary cause behind the accelerated degradation for the LFP cells tested.

6.6.2. Lithium cobalt oxide cells

For the LCO cells, just the impact of two temperatures and two different current profiles — dynamic 66 Wh and dynamic 198 Wh — were investigated. The relationship between capacity fading and cycling are illustrated by Figures 6.12a and 6.12b. A general feature can be observed for all the LCO cells, they presented a sharp drop in capacity at the beginning of the test, but as the cycling continued the capacity degradation rate decreased irrespectively of the current profile or testing temperature.

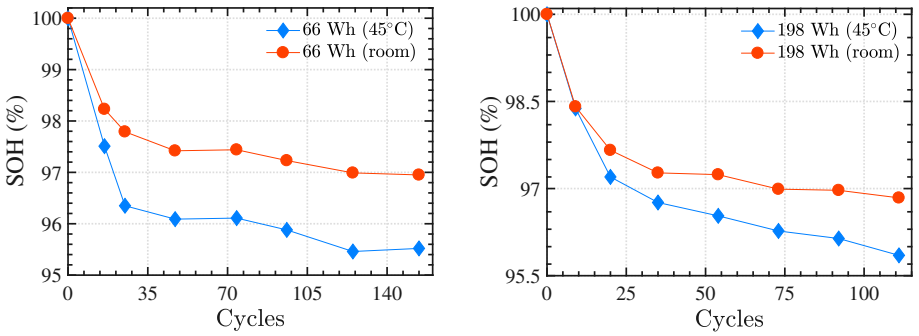

(a) (b)

Figure 6.12: SOH variation for (a) LCO cells cycled with a dynamic 66 Wh profile (D66) at room temperature and 45°C, and (b) LCO cells cycled with a dynamic 198 Wh profile (D198) at room temperature and 45°C.

Table 6.10: Difference in SOH (ΔSOH) between cells tested at 25 and 45°C for LCO cells after 25, 74, and 125 cycles. The cells are cycled with a dynamic 66 Wh and a dynamic 198 Wh profile.

cycles	SOH (%) 45°C, 66 Wh	SOH (%) 25°C, 66 Wh	Δ SOH (%)	SOH (%) 45°C, 198 Wh	SOH (%) 25°C, 198 Wh	Δ SOH (%)
25	96.35	97.79	1.44	97.34	97.53	0.19
74	96.11	97.44	1.33	96.27	96.99	0.72
125	95.46	96.99	1.53	95.71	96.95	1.23

Comparing profiles with different battery sizes for LCO: 66 Wh vs. 198 Wh

Table 6.10 introduces the SOH for the D198 and D66 profiles along with the temperatures at which the experiments were performed. If the temperature is kept at 45°C, and the D66 profile is compared to the D198 profile, it can be found that the D198 results in almost a difference of 1% SOH with respect to the D66. Although as the cycling continues the difference between them reduces to only 0.25% SOH after 125 cycles. When the testing is completed at room temperature, the measurements show a no representative difference of 0.04% more SOH for the 66 Wh profile related to the 198 Wh

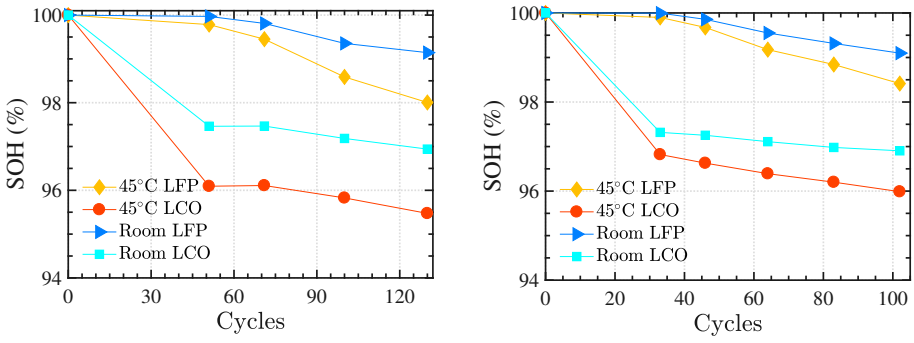

(a) 66 Wh (b) 198 Wh

Figure 6.13: Comparison of LFP and LCO for the (a) 66 Wh (D66) and (b) 198 Wh (D198) current profiles.

profile. Hence, similarly to the conclusion reached in Section 6.6.1, the 66 Wh and 198 Wh current profiles do not have distinguishable effect on aging of the cells.

Temperature effect

The same behavior, observed for the LFP cells, where cycling the battery at 45°C caused a more accelerated degradation than batteries exposed to room temperature, also applies to the LCO cells. Based on Table 6.10, the capacity of the LCO cells faded by 1.53% and 1.23% of SOH for the D66 and D198 profiles, respectively. Furthermore, as the cycling advanced, there is a tendency to increase more the differences on SOH for the two temperature levels (refer to Figures 6.12a and 6.12b).

6.6.3. Selecting a battery technology

As stated previously, the LFP and LCO were the chosen Li-ion cells to be tested in order to select one out of the two as the candidate for the *PBIM*. According to the aging test that both technologies underwent, the LFP cells present lower values of degradation, or higher SOHs, under the same testing conditions, for identically normalized current profiles and reference temperatures. Figure 6.13 shows the SOH change as a function of the number of cycles for the 66 Wh and 198 Wh profiles. In the case of the 66 Wh profile for 45°C, there is a difference on SOH of 2.53% at the last cycle (130) in favor of the LFP cells. Similarly, for the 198 Wh profile, the LFP outperforms the LCO by 2.43% at 45°C. When analyzing the data obtained at room temperature, the reduction on SOH values are not as pronounced as for the 45°C; however, the same tendency remains, LFP aged slower. Therefore, LFP is selected as the battery technology to be used in the *PBIM* based on the capacity fading results.

6.6.4. Expected battery aging for *PBIM*

Assuming that the *PBIM* will operate for battery sizes that entail lower C-rates that the expected in the 66 Wh profile, the 198 Wh dynamic profile is chosen in this section to indicate the predicted aging for the *PBIM* considering its region of operation, while an estimation of the battery lifetime is calculated for this profile (198 Wh).

As presented in Figure 6.14, the *PBIM* is expected to operate between the limits defined by the upper boundary (45°C) and the lower limit (room temperature). Because the maximum operating point determined by testing the *PBIM* prototype was 45°C in severe conditions, this condition is not likely to occur frequently. On the other hand, having the batteries operating as they were placed indoors is considered optimistic. As a consequence, the degradation of the batteries packed inside the *PBIM* is likely to occur between the boundaries proposed in Figure 6.14.

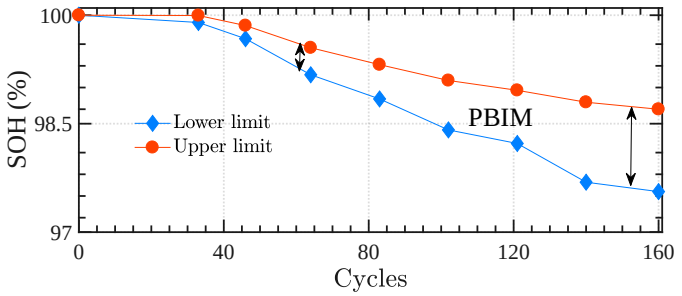

Figure 6.14: Expected range of operation for the battery pack inside the *PBIM*.

6

6.7. Conclusion

In this chapter, a framework to select a suitable battery technology for the *PBIM* is presented. Firstly, a prototype of the *PBIM* concept was tested under harsh conditions in order to use this information as an input for designing a battery aging test, which guided the selection of the battery technology among the previously identified options based on literature. By using the prototype, the electrical performance and thermal behavior were studied by measuring the power generated by the solar panel and stored in the battery pack. On average, the measured power conversion efficiency of the charge controller was 95.7%. Also, the power produced by the solar panel showed a steadily reducing trend as a result of the temperature increase. Regarding the thermal response, as expected, the temperature of all the components of the *PBIM* were warmer than in a conventional system (with not attached batteries and charge controller to the PV panel), and the batteries reached a maximum temperature of 45°C. This temperature was defined as the upper limit for the operation of the *PBIM* and used for the aging testing. The testing was also designed based on an integrated model that provides information about the typical current profiles expected for the *PBIM*. These current profiles were applied to two selected Li-ion cells, viz. $LiFePO_4$ and $LiCoO_2$, after a careful analysis of the available cells in the market. From the cycling testing results, it was found that the effect of high temperature is more significant than the influences of the applied current profiles on both types of cells. Finally, between these two Li-ion chemistries, the $LiFePO_4$ present lower capacity fading rates, and as a consequence, it is suggested as the most suitable for the *PBIM*.

References

[1] V. Vega-Garita, S. Garg, N. Narayan, L. Ramirez-Elizondo, and P. Bauer, *Testing a pv-battery integrated module prototype,* in *2018 IEEE 7th World Conference on Photovoltaic Energy Conversion (WCPEC)* (2018) pp. 1244–1248.

[2] V. Vega-Garita, A. Hanif, N. Nishant, L. Ramirez-Elizondo, and P. Bauer, *Selecting a battery technology for the Photovoltaic Battery Integrated Module,* Power Sources (2019).

[3] F. Zhang, W. Li, Z. Xu, M. Ye, W. Guo, H. Xu, and X. Liu, *Transparent conducting oxide- and Pt-free flexible photo-rechargeable electric energy storage systems,* RSC Advances **7**, 52988 (2017).

[4] M. Freitas, T. Penha, and S. Sirtoli, *Chemical and electrochemical recycling of the negative electrodes from spent NiCd batteries, Journal of Power Sources*, **163**, 1114 (2007).

[5] P. Bernard and M. Lippert, *NickelCadmium and NickelMetal Hydride Battery Energy Storage, Electrochemical Energy Storage for Renewable Sources and Grid Balancing*, , 223 (2015).

[6] C. Nogueira and F. Margarido, *Chemical and physical characterization of electrode materials of spent sealed NiCd batteries,* Waste Management **27**, 1570 (2007).

[7] X. Hu, C. Zou, C. Zhang, and Y. Li, *Technological developments in batteries: A survey of principal roles, types, and management needs,* IEEE Power and Energy Magazine **15**, 20 (2017).

[8] N. Omar, Y. Firouz, M. Monem, A. Samba, H. Gualous, T. Coosemans, P. V. den Bossche, and J. V. Mierlo, *Analysis of nickel-based battery technologies for hybrid and electric vehicles,* in *Reference Module in Chemistry, Molecular Sciences and Chemical Engineering* (Elsevier, 2014).

[9] X. Hu, C. Zou, C. Zhang, and Y. Li, *Technological Developments in Batteries: A Survey of Principal Roles, Types, and Management Needs,* IEEE Power and Energy Magazine (2017), 10.1109/MPE.2017.2708812.

[10] A. Poullikkas, *A comparative overview of large-scale battery systems for electricity storage,* Renewable and Sustainable Energy Reviews **27**, 778 (2013).

[11] M. Skyllas-Kazacos and J. F. Mccann, *Vanadium redox flow batteries (VRBs) for medium- and large-scale energy storage,* Advances in Batteries for Medium and Large-Scale Energy Storage , 329 (2015).

[12] M. Wild, L. O'Neill, T. Zhang, R. Purkayastha, G. Minton, M. Marinescu, and G. J. Offer, *Lithium sulfur batteries, a mechanistic review,* Energy Environ. Sci. (2015), 10.1039/C5EE01388G.

[13] L. Yue, J. Ma, J. Zhang, J. Zhao, S. Dong, Z. Liu, G. Cui, and L. Chen, *All solid-state polymer electrolytes for high-performance lithium ion batteries,* Energy Storage Materials **5**, 139 (2016).

[14] B. J. Kim, D. H. Kim, Y.-Y. Lee, H.-W. Shin, G. S. Han, J. S. Hong, K. Mahmood, T. K. Ahn, Y.-C. Joo, K. S. Hong, N.-G. Park, S. Lee, and H. S. Jung, *Highly efficient and bending durable perovskite solar cells: toward a wearable power source,* Energy Environ. Sci. **8**, 916 (2015).

[15] J. W. Fergus, *Recent developments in cathode materials for lithium ion batteries,* Journal of Power Sources (2010), 10.1016/j.jpowsour.2009.08.089.

[16] A. Du Pasquier, I. Plitz, S. Menocal, and G. Amatucci, *A comparative study of Li-ion battery, supercapacitor and nonaqueous asymmetric hybrid devices for automotive applications,* Journal of Power Sources (2003), 10.1016/S0378-7753(02)00718-8.

[17] G. Berckmans, M. Messagie, J. Smekens, N. Omar, L. Vanhaverbeke, and J. Van Mierlo, *Cost projection of state of the art lithium-ion batteries for electric vehicles up to 2030,* Energies **10** (2017), 10.3390/en10091314.

[18] N. Nitta, F. Wu, J. T. Lee, and G. Yushin, *Li-ion battery materials: Present and future,* Materials Today **18**, 252 (2015), arXiv:arXiv:1011.1669v3 .

[19] D. Doughty and E. P. Roth, *A general discussion of Li-ion battery safety,* (2012).

[20] P. Kalyani and N. Kalaiselvi, *Science and Technology of Advanced Materials Various aspects of LiNiO 2 chemistry: A review Various aspects of LiNiO 2 chemistry: A review,* (2017), 10.1016/.

[21] C. H. Chen, J. Liu, M. E. Stoll, G. Henriksen, D. R. Vissers, and K. Amine, *Aluminum-doped lithium nickel cobalt oxide electrodes for high-power lithium-ion batteries,* Journal of Power Sources (2004), 10.1016/j.jpowsour.2003.10.009.

[22] L. Yunjian, L. Xinhai, G. Huajun, W. Zhixing, H. Qiyang, P. Wenjie, and Y. Yong, *Electrochemical performance and capacity fading reason of LiMn2O4/graphite batteries stored at room temperature,* Journal of Power Sources **189**, 721 (2009).

[23] N. Yabuuchi and T. Ohzuku, *Novel lithium insertion material of LiCo1/3Ni1/3Mn1/3O2 for advanced lithium-ion batteries,* in *Journal of Power Sources* (2003).

[24] T. M. Bandhauer, S. Garimella, and T. F. Fuller, *A Critical Review of Thermal Issues in Lithium-Ion Batteries,* Journal of The Electrochemical Society **158**, R1 (2011).

[25] J. Vetter, P. Novák, M. R. Wagner, C. Veit, K. C. Möller, J. O. Besenhard, M. Winter, M. Wohlfahrt-Mehrens, C. Vogler, and A. Hammouche, *Ageing mechanisms in lithium-ion batteries,* Journal of Power Sources **147**, 269 (2005).

[26] D. E. Demirocak and B. Bhushan, *Probing the aging effects on nanomechanical properties of a LiFePO4 cathode in a large format prismatic cell,* Journal of Power Sources **280**, 256 (2015).

[27] M. M. Kabir and D. E. Demirocak, *Degradation mechanisms in Li-ion batteries: a state-of-the-art review,* International Journal of Energy Research (2017), 10.1002/er.3762.

[28] A. Mukhopadhyay and B. W. Sheldon, *Deformation and stress in electrode materials for li-ion batteries,* Progress in Materials Science **63**, 58 (2014).

[29] G. Ning, B. Haran, and B. N. Popov, *Capacity fade study of lithium-ion batteries cycled at high discharge rates,* Journal of Power Sources **117**, 160 (2003).

[30] R. Yazami and Y. F. Reynier, *Mechanism of self-discharge in graphitelithium anode,* Electrochimica Acta **47**, 1217 (2002).

[31] P. Keil, S. F. Schuster, J. Wilhelm, J. Travi, A. Hauser, R. C. Karl, and A. Jossen, *Calendar Aging of Lithium-Ion Batteries,* Journal of The Electrochemical Society **163**, A1872 (2016).

[32] S. Grolleau, A. Delaille, H. Gualous, P. Gyan, R. Revel, J. Bernard, E. Redondo-Iglesias, and J. Peter, *Calendar aging of commercial graphite/LiFePO4cell - Predicting capacity fade under time dependent storage conditions,* Journal of Power Sources **255**, 450 (2014).

[33] O. Isabella, A. Smets, K. Jäger, M. Zeman, and R. van Swaaij, *Solar energy: The physics and engineering of photovoltaic conversion, technologies and systems,* UIT Cambridge Limited (2016).

[34] V. Vega-Garita, L. Ramirez-Elizondo, and P. Bauer, *Physical integration of a photovoltaic-battery system: A thermal analysis,* Applied Energy **208**, 446 (2017).

[35] M. Hammami, S. Torretti, F. Grimaccia, and G. Grandi, *Thermal and Performance Analysis of a Photovoltaic Module with an Integrated Energy Storage System,* Applied Sciences **7**, 1107 (2017).

[36] O. Tremblay, L. Dessaint, and A. Dekkiche, *A generic battery model for the dynamic simulation of hybrid electric vehicles,* in *2007 IEEE Vehicle Power and Propulsion Conference* (2007) pp. 284–289.

[37] N. Narayan, T. Papakosta, V. Vega-Garita, Z. Qin, J. Popovic-Gerber, P. Bauer, and M. Zeman, *Estimating battery lifetimes in solar home system design using a practical modelling methodology,* Applied Energy **228**, 1629 (2018).

[38] A123 Systems, *Battery Pack Design , Validation , and Assembly Guide using A123 Systems AMP20M1HD-A Nanophosphate Cells,* , 1 (2014).

[39] Renata SA Switzerland, *Renata ICP606168PRT Engineering Specification,* (2013).

7

Conclusions

In this chapter, the general conclusions of the research performed in this thesis are presented. Moreover, the research questions formulated in chapter 1 are addressed based on the results derived from the previous chapters. This thesis focuses on the challenges derived from the integration of a solar panel and a battery pack in one single device. For approaching the task of designing such a device, first, an extensive literature review was done encountering that in previous research have not paid attention to system sizing, thermal management, and battery capacity degradation. In terms of system sizing, a methodology was developed to shed light on the optimum PV rating and battery storage capacity combination for an off-grid application. Later, an energy management system was implemented using a DC coupled architecture, and it was capable of following seven modes of operation that controls the PV generation and battery operation for off-grid and grid-connected systems. Also, the thermal behaviour of the integrated device was studied, finding that by including an air gap between the PV panel and the battery pack, the temperature of the batteries can diminish considerably. Based on the model developed when analyzing the *PBIM*, a prototype was designed and tested in severe conditions. According to the data gathered by the prototype testing and an application-based model, battery degradation testing was designed for two battery candidates. After an extensive degradation test that reproduce the conditions expected in the *PBIM*, the $LiFePO_4$ found the most suitable. In conclusion, this thesis presents an energy management system to control the power flows, a thermal management technique to maintain the components operating in a safe region, and selects the most suitable battery technology, moving from the concept of integration to a prototype.

What are the most critical challenges and limitations when integrating a PV panel and a battery pack in one device?

Previous research on physical integrated devices, similar to *PBIM* (high power devices, see section 2.2.2), have been focused merely on a basic demonstration of the concept and the development of power electronics for the application. Little attention was paid to the most susceptible component of the system, the battery. Especially considering the thermal stresses that come along with the integration concept. Hence, one of the goals of this thesis is to reduce the temperature of operation of the components by exploring various thermal management techniques. Although the temperature of the battery can be reduced, in the *PBIM* the temperatures are always higher than in conventional systems. Therefore, it is crucial to asses the effect of temperature on battery aging, which is another objective pursued in this thesis. The other component that has been left behind is the system sizing, an essential part, considering that in an integrated device space and cost are constraints. Also, depending on the application, the PV rating and battery capacity must be determined, and its sizes are limited.

What are the boundaries in terms of PV rating and battery capacity for a single *PV-battery Integrated Module* in a standalone system considering system availability?

When selecting the PV rating and capacity of the battery pack, the inherent space limitations and expected operation condition of a device such as the *PBIM* are essential. Therefore, an iterative sizing methodology was proposed to study the combination of PV power rating and battery capacities able to ensure a reliable off-grid PV system. The results show that for a tier 3 load (defined by the energy access framework) and a loss of load probability of less than 10%, a 320 W_p and battery with a capacity of 864 Wh was needed, which reach the maximum PV rating available for commercial PV panels; therefore a single *PBIM* will not able to supply loads higher than tier 3 for the required system availability constraints (10%). However, if less energy demanding load is to be powered, the PV power could be reduced to 107 W_p and the battery to just 296 Wh.

How to implement an energy management system for the *PV-battery Integrated Module* to enable an intelligent power and energy delivery?

For implementing an energy management system, the system architecture must be defined in order to establish a control strategy to manage the power flows of the PV-battery system. A DC coupled architecture was found as the most appropriate, considering the number of conversion steps, safety, and control complexity. In this architecture, the maximum power point tracking and PV power curtailment are performed by a boost converter, while the charging and discharging of the battery is carried out by a buck-boost converter. These two converters are connected to a DC bus that must be kept at a constant voltage. To the DC bus, a microinverter is added to supply the loads. Seven modes of operation are defined in order to allow the use of the *PBIM* in three case studies, namely off-grid PV-battery system, constant load, and a peak shaving (grid-tied). For these cases, it was demonstrated that the *PBIM* can be managed to supply the load

and regulate the power delivery.

How can high temperatures reached by the battery pack be managed in order to ensure that the *PV-battery Integrated Module* performs within a safe region of operation

In a device as the *PBIM*, the closeness between the PV panel and balance of system components (battery pack and power electronics) result in temperatures of operation higher than the experienced in conventional PV-battery systems. Consequently, a finite element thermal model was developed not only to characterize the thermal response of the *PBIM* but also to propose a thermal management method to reduce the temperature of the battery pack. According to the performed simulation, it was found that an air gap of between the PV panel and battery pack of 5–7 cm help reducing the temperature of the batteries considerably. Although a phase change material could be used to reduce even more the temperature of the components, this solution is considered impractical. Therefore, an air gap is considered an appropriate thermal management method for the *PBIM*.

Which is the most suitable electrochemical cell technology or technologies to integrate a PV module and storage physically in one package based on aging?

Having recognized the negative influence of high temperatures on battery aging, a prototype is tested to study the thermal behavior batteries under extreme conditions — high irradiation and low convection. The temperature of the batteries was monitored, and it was found that the maximum temperature reached was 45°C. Based on the inputs received from the prototype testing and the integrated model that reproduced the expected electrical and thermal behavior of the *PBIM*, a battery aging test was designed. Two Li-ion candidates were extensively cycled at two temperatures (45°C and ambient) three current profiles. According to the measure battery's state of health (SOH), batteries tested at 45°C aged faster than the batteries kept at ambient temperature. Also, it was found that the different current profiles have a limited influence on battery aging for the application studied. Moreover, after comparing the SOH results for LFP and LCO, LFP showed a slower degradation rate. Therefore, this battery technology is selected as a suitable option for the *PBIM*.

Recommendations and future work

Power electronics

The design of power electronics adapted to the specifications of the *PBIM* was not explored in detail in this dissertation. Therefore, a detailed analysis of the adverse effect expected due to the high temperatures on the reliability of the power electronics is recommended, especially considering that the converter must be as thin as possible to achieve a highly compact device, which could lead to more accelerated aging compared to ordinary not completely integrated devices. To accomplish high compactness, an integrated power electronics in one single board could combine all the converters needed to take care of the energy management system and battery management sys-

tem. However, to realize this, a more detailed analysis of available system topologies for a completely integrated power electronics deserves further research.

Cost analysis
An analysis on total system cost, including not only components cost, but also installation and design cost that could be saved by the *PBIM* in comparison to typical systems, can help to quantify the expected benefits of a completely integrated solution. Also, it is important to investigate which types of application the integrated devices are more economically feasible. In this thesis, off-grid applications were explored in chapter 3, but grid-connected systems is also a potential application that should be included in the cost analysis.

Most extensive battery testing
A more extensive battery testing is suggested to corroborate if the aging trends reported in chapter 6 remain. It is suggested to test the batteries until its end-of-life (80% of initial capacity). Also, other battery technologies that at the moment of this thesis were in an early stage of development, such as Li-S and solid electrolyte Li-ion batteries, are perceived as a viable alternative to cope with high temperatures of operation and deserve to be tested in the future.

System modularity
By connecting various *PBIMs* in parallel, the PV production, as well as the total battery capacity, can be scaled up. Therefore, exploring the usefulness of multiple *PBIMs* in more energy and power demanding applications is an attractive idea for further research. To achieve an effective interconnection and coordination in power delivery of multiple *PBIMs*, the communication between them to follow a predefined energy management strategies is fundamental. Therefore, the implementation of global control for the *PBIMs* would need future work.

Outdoor testing
Finally, a prototype of the *PBIM* was tested indoors in this dissertation; however, outdoor testing is more close to the operational conditions that the *PBIM* will face. Therefore, designing a prototype that could be placed outdoors while the efficiency, temperature and battery degradation is measured may be an important advance in the field of integrated devices. In later stages of development, preventing water from outside entering into the device while providing appropriate ventilation are seen as future lines of research as well.

Acknowledgements

This PhD dissertation has been the result of a long journey that would have been impossible to navigate, and reach the finish line, without the help and motivation from many people and institutions. Hence, I will like to thank all of them and acknowledge their contributions in this section of the manuscript.

First of all, I would like to thank my promotor, Professor Pavol Bauer, for accepting me as a member of the, at the moment I joined, recently created DCE&S group. I went through many difficulties when starting my studies, but thank the guidance of professor Bauer, I was able to focus my efforts more intensely to finish on time my PhD. From him, among other things, I learned how to communicate fast and to the point, a skill that I consider as very useful. Additionally, I will like to show my gratitude for the help I received when settling down with my family in the Netherlands.

I would also like to thank Professor Miro Zeman, with whom I did not have much contact during the research, but all the interactions we had were fruitful. I will always remember that my first approach towards the PV field was through his lectures. Also, I remember his always inspirational toasts during the department activities that inspired us to give the best.

I want to express my gratitude to my daily supervisor, Dr. Laura Ramirez, which I met by coincidence. With her help, my life changed drastically thanks to the opportunity to study in TU Delft. I always felt welcome to discuss with her about any topic related or not to the PhD. I admire your multiple capacities as a musician, lecturer, supervisor, but more importantly, as an incredible human being.

I thank my doctoral examination committee, which consisted of Prof. dr. A.H.M Smets, Prof.ir. P.T.M Vaessen, Prof.dr. M. Gibescu, and Dr. T. Merdzhanova for accepting being members of the committee and for the feedback and constructive comments towards improving the dissertation.

During the research, I needed constant support from the technicians in charge of our lab. A special thank to Harrie Olsthoorn, which was available every time I needed, Joris Koeners, during the battery testing and Dr.ir. Bart Roodenburg for the coordination of the lab and for helping me translating the summary of this dissertation into Dutch. Thank you, Ad for helping with the logistics. Moreover, my special gratitude to our secretary, Sharmila, her help and constant dedication during my period in Delft and in Costa Rica has been invaluable.

I highly appreciate the opportunity given to me by my colleagues from the Department of Electrical Engineering at the University of Costa Rica, which supported my efforts to get a scholarship from the International Office of the University of Costa Rica. Thanks to this scholarship, I was able to bring my family and cover the expenses related to my studies in TU Delft. I was also partially funded by the Ministerio de Ciencia y Tecnología y Telecomunicaciones of Costa Rica, and Consejo Nacional para Investigaciones Científicas y Tecnológicas, to which I thank.

I consider myself very lucky, as I was able to share my time with my PhD colleagues. I really appreciate the many times we spent during lunch and coffee breaks. I will always be grateful for being able to share with Mladen, Ilija, Minos, Prasanth, Martin, and Tim. Udai, it was nice to talk to you about India and life in general. Thank you, Nils for instructing us about the Dutch culture. Ibrahim, thank you for taking us to that excellent Lebanese place in the Hague. Gilmero (I mean Guillermo), Luis and Fabio, thank you for the casual chats in *español*. Soumya, what a nice man, thanks for the football conversation and help with the optimisation. Lucia, a really like your energy and the fact you can speak Spanish so fast that I could merely understand :). Pavel, thank you for coming many times to call us for lunch. Shubhangi, thank you for the many good coffees we had. Aditya, thank you for making our coffee and lunch time more fun. My special gratitude to Thiago, Muhamad, Babak, Rodrigo, Francesca, Alessandro, Marco, Djurre, Jiayang, Wiljan, Zhi, Wenli, and Tianzhu. Also, thank you Laurens and Tsegay for the frequent conversation we had. Zian, thank you for letting me stay in your lovely house for the last months I stayed in the Netherlands.

For more than four years, the office LB03.680 was my second house. There, I have the pleasure to meet Johan and Tim. Johan, thank you for all the many things you left our/your apartment once you left the Netherlands. During the time of settling down with my family and later on, your help Gautham has been highly appreciated, for that I will always be indebted to you. Nishant, without the sometimes endless discussions we had, ranging from all possible topics, I know that my PhD would have been even more challenging and stressful. Thanks a lot, *mi amigo*!. Na, thank you for giving us company. We also had Yunhe, our sister, it was a pleasure working with you during your master, and have you for a small period in the office.

I had the opportunity to work with several master students in a variety of projects. Due to their willingness to work in my PhD project, I was able to accomplish more and explore facets of my research that I could not have done by myself. I also learned valuable lessons about coaching and life in general from them. Thank you: Yunhe (the first one), Nadhilah, Ilman, Anindio, Loic, Thekla, Diego, Faizal, Yunizar, Novy, Mónica, Wenrui, Shiwankar, Ali, and Manolis.

My time in the Netherlands it would have been completely different without the people I meet during the journey. I am grateful to Helga, Mike, and Gabi, an incredible family that invited us many times to their place, a place where I had very interesting conversations. Thank you Dalal and Rital for having us in Jordan, it was a lifetime experience being there. Thank you, Cristobal and Josefina, for the football afternoons we spent with the kids. Faulk and Josselin, thank you for sharing with us the new year evening of 2018 and let us stay with your house for the defence. The list is long, but we really appreciated your friendship: Daduí, Fernanda, Zoé, Carolina, Dennis, Gonzalo, Adriana, Francesca, Nicola, Hasan, Mah, Eduardo, and Gabriela.

I will like to express my gratitude to the Costa Ricans in Delft: William, Laura and Juan Andrés, I will never forget that I spent my first night in Delft at your place. Marta and Johan, it was nice to find you both there, we really like to spend time having dinner or coffee with you. Andrés and Mary, thank you for the many occasions in which you received us at your house, where we could enjoy remembering Costa Rica and what it means to be away from home. I will miss Santi and Fede, same Tomás. Also, thank

you, Miguel, Andrea, and Pamela for the time we shared.

Finally, and most importantly, I have a huge admiration and gratitude to my wife. Ana, your constant support and resilience made this possible. You left your job, and family to come with me, I hope someday will be able to give you a small portion back. It was difficult at the beginning, but we manage to survive and eventually enjoy our time in the Netherlands. Tomás, you are and always will be my source of inspiration. Having you in the Netherlands with me has been the experience of my life. *Mamá y papá, su ayuda incondicional y apoyo ha sido muy importante para mí, los quiero mucho*. Diana, I love you and thank you for visiting us in the Netherlands.

A

Transient analysis

A.1. Transient Analysis

The following equations define the procedure followed to find the parameters needed by the feedback loop of the boost and buck-boost converters introduced in chapter 4:

A.1.1. Boost Converter

$$e_1(t) = V_{\mathrm{PV}}(t - \Delta t) - V_{\mathrm{PV,ref}}(t) \tag{A.1}$$

$$e_2(t) = I_{\mathrm{PV}}(t - \Delta t) - I_{\mathrm{PV,ref}}(t) \tag{A.2}$$

$$I_{\mathrm{PV,ref}}(t) = \mathrm{K_{p,v}} \cdot e_1(t) + \mathrm{K_{i,v}} \cdot \int_0^t e_1(t)dt \tag{A.3}$$

$$D'_{\mathrm{boost}}(t) = \mathrm{K_{p,i}} \cdot e_2(t) + \mathrm{K_{i,i}} \cdot \int_0^t e_2(t)dt \tag{A.4}$$

A.1.2. Buck-Boost Converter

$$e_3(t) = V_{\mathrm{DC}}(t - 1) - V_{\mathrm{DC,ref}}(t) \tag{A.5}$$

$$e_4(t) = I_{\mathrm{batt}}(t - 1) - I_{\mathrm{batt,ref}}(t) \tag{A.6}$$

$$I_{\mathrm{batt,ref}}(t) = \mathrm{K_{p,v}} \cdot e_3(t) + \mathrm{K_{i,v}} \cdot \int_0^t e_3(t)dt \tag{A.7}$$

$$D_{\text{buck-boost}}(t) = \mathrm{K_{p,i}} \cdot e_4(t) + \mathrm{K_{i,i}} \cdot \int_0^t e_4(t)dt \tag{A.8}$$

The transient simulations were implemented in MATLAB/Simulink, according to the architecture depicted in Figure 4.1b. For this simulation, the load and inverter are substituted by constant impedance DC load to simplify the simulation.

The simulation was set to run for 0.4 s as the changes were visible under that period. In Figure A.1a, a rapid shift in power is observed; this happens because the

A

irradiance values were changed first from 0 to 500 W/m^2, and later from 500 to 1000 W/m^2 after 0.2 s, a period in which the MPP was reached. Also, based on Figure A.1b, two disturbances can be observed, which corresponds to the changes in irradiance. At the beginning of the simulation the solar power was not enough, so the load was not completely satisfied; therefore, the bus voltage slightly deviated from 36 V. Later, power is extracted from the battery to keep the power balance and reach the reference voltage and match the load. When the irradiance reached 1000 W/m^2, the solar production is now above the power required, and the DC bus voltage rose accordingly. Given the power excess, the battery is powered, and the voltage comes back to its reference level after 0.1 s, reaching equilibrium.

$$V_{\mathrm{PV}} = (1 - D_{\mathrm{boost}})\, V_{\mathrm{DC}} \tag{A.9}$$

$$V_{\mathrm{DC}} = \frac{V_{\mathrm{batt}}}{D_{\mathrm{buck\text{-}boost}}} \tag{A.10}$$

Table A.1: Parameters for transient simulation.

Parameter	Value	Parameter	Value
$V_{\mathrm{DC,ref}}$	36 V	L_{boost}	1 mH
$V_{\mathrm{PV,mpp}}$	18 V	$L_{\mathrm{buck\text{-}boost}}$	5 mH
$V_{\mathrm{batt,nom}}$	26.4 V	$C_{\mathrm{in,boost}}$	0.01 mF
PV power rating	140 W	$C_{\mathrm{out,boost}}$	2 mF
Load (nominal voltage, nominal load)	36 V, 100 W	C_{batt}	0.01 mF
Converter switching frequency	50 kHz	C_{DC}	2 mF
$K_{\mathrm{p,v}}$	0.2	$K_{\mathrm{i,v}}$	100
$K_{\mathrm{p,i}}$	0.02	$K_{\mathrm{i,i}}$	20

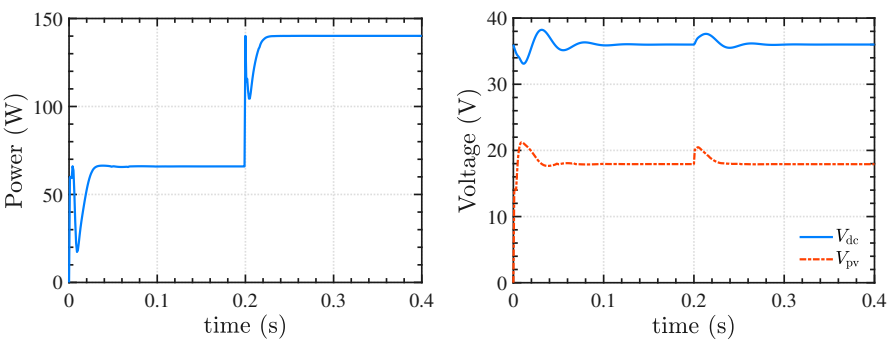

Figure A.1: Transient analysis for (a) PV power and (b) PV and DC voltage.

Curriculum Vitæ

Víctor Ernesto Vega Garita

24-10-1986 Born in Heredia, Costa Rica.

Education

2004–2010 Materials Engineering
Costa Rica Institute of Technology, Costa Rica

2014–2019 PhD. Electrical Engineering
Delft University of Technology, Netherlands

Thesis:	Integrating a Photovoltaic Panel and a Battery Pack in One Module
Promotor:	Prof. dr.ir P. Bauer
Promotor:	Prof. dr. M. Zeman
Daily supervisor:	Dr. L. Ramírez Elizondo

Experience

2019 Lecturer
Electrical Engineering Department
University of Costa Rica, Costa Rica

List of Publications

A.2. Publications related to this thesis

Journal papers

4. **V. Vega-Garita**, A. Hanif, L. Ramirez-Elizondo and P. Bauer, *Selecting a Suitable Battery Technology for a Photovoltaic Battery Integrated Module*, Journal of Power Sources, ***under review***, 2019.

3. **V. Vega-Garita**, M. Faizal Sofyan, N. Narayan, L. Ramirez-Elizondo, P. Bauer, *Energy Management System for the Photovoltaic Battery Integrated Module*, Energies, 2018.

2. **V. Vega-Garita**, L. Ramirez-Elizondo, N, Narayan and P. Bauer, *Integrating a Photovoltaic-Storage System in One Device: a Critical Review*, Progress in Photovoltaics, 2018.

1. **V. Vega-Garita**, L. Ramirez-Elizondo, and P. Bauer, *Physical integration of a photovoltaic-battery system: A thermal analysis*, Applied Energy, 2017.

Conference papers

4. **V. Vega-Garita**, S. Garg, N. Narayan, L. Ramirez-Elizondo and P. Bauer, *Testing a PV-Battery Integrated Module Prototype*, World Conference on Photovoltaic Energy Conversion 7th, 2018.

3. **V. Vega-Garita**, D. De Lucia, N. Narayan, L. Ramirez-Elizondo, and P. Bauer, *PV-Battery Integrated Module as a Solution for Off-Grid Applications in the Developing World*, IEEE Energycon, 2018.

2. **V. Vega-Garita**, L. Ramirez-Elizondo, G. R. C. Mouli, and P. Bauer, *Review of residential PV-storage architectures*, IEEE ENERGYCON, 2016.

1. **V. Vega-Garita**, A. P. Harsarapama, L. Ramirez-Elizondo, and P. Bauer, *Physical integration of PV-battery system: Advantages, challenges, and thermal model*, IEEE Energycon, 2016.

A.3. Other publications

Journal papers

4. N. Narayan, A. Chamseddine, **V. Vega-Garita**, J. Popovic-Gerber, P. Bauer, and M. Zeman, *Quantifying the Benefits of a Solar Home System-Based DC Microgrid for Rural Electrification*, Energies, 2019.

3. N. Narayan, A. Chamseddine, **V. Vega-Garita**, J. Popovic-Gerber, P. Bauer, and M. Zeman, *Exploring the boundaries of standalone Solar Home Systems for off-grid electrification: optimal sizing of Solar Home System for various tiers of the Multi-tier framework for household electricity access* , Applied Energy, 2019.

2. Y. Yu, N. Narayan, **V. Vega-Garita**, J. Popovic-Gerber, Z. Qin, M. Wagemaker, P. Bauer, M. Zeman, *Constructing Accurate Equivalent Electrical Circuit Models of Lithium Iron Phosphate and Lead-acid Battery Cells for Solar Home System Applications*,Energies, 2018.

1. N. Narayan, T. Papakosta,**V. Vega-Garita**, Z. Qin, J. Popovic-gerber, P. Bauer, *Estimating battery lifetimes in Solar Home System design using a practical modelling methodology*, Applied Energy, 2018.

Conference papers

3. N. Narayan, **V. Vega-Garita**, Z. Qin, J. Popovic-gerber, P. Bauer, and M. Zema, *A modeling methodology to evaluate the impact of temperature on Solar Home Systems for rural electrification*, IEEE Energycon, 2018.

2. N. Narayan, T. Papakosta,**V. Vega-Garita**, J. Popovic-Gerber, P. Bauer, and M. Zeman, *A simple methodology for estimating battery lifetimes in Solar Home System design*, 2017 IEEE AFRICON Sci. Technol. Innov. Africa, AFRICON 2017, 2017.

1. I. Sulaeman, **V. Vega-Garita**, G. R. C. Mouli, N. Narayan, L. Ramirez-Elizondo, and P. Bauer, *Comparison of PV-battery architectures for residential applications*, IEEE Energycon, 2016.